Phase relations in Zn-group IV-oxide nitride (IV: Ge, Sn) wide gap semiconductors

Dissertation

zur Erlangung des akademischen Grades des

Doktor der Naturwissenschaften

(Dr. rer. nat.)

eingereicht im Fachbereich Geowissenschaften

der Freien Universität Berlin

angefertigt am Helmholtz-Zentrum Berlin für Materialien und Energie

Abteilung Struktur und Dynamik von Energiematerialien

vorgelegt von

Zhenyu Wang

2022, Berlin

Vorgelegt bei

Erstgutachter/in:

Prof. Dr. Susan Schorr

Freie Universität Berlin / Helmholtz-Zentrum Berlin für Materialien und Energie

Zweitgutachter/in:

Prof. Dr. Timm John

Freie Universität Berlin

Tag der Disputation: 08.11.2022

Eidesstattliche Erklärung

Hiermit versichere ich, dass ich die vorliegende Arbeit selbstständig verfasst und keine anderen als die angegebenen Quellen und Hilfsmittel benutzt habe. Alle Ausführungen, die anderen veröffentlichten oder nicht veröffentlichten Schriften wörtlich oder sinngemäß entnommen wurden, habe ich kenntlich gemacht. Die Arbeit hat in gleicher oder ähnlicher Fassung noch keiner anderen Prüfungsbehörde vorgelegen.

Berlin, 24.01.2022
Zhenyu Wang

Einverständniserklärung

Ich erkläre mich einverstanden mit dem Abgleich meiner Dissertation mit anderen Texten zwecks Auffindungen von Übereinstimmungen sowie mit einer zu diesem Zweck vorzunehmenden Speicherung der Dissertation in einer Datenbank.

Berlin, 24.01.2022
Zhenyu Wang

Acknowledgement

This thesis would not have been accomplished without the help, support and encouragement of many people.

First of all, I acknowledge my supervisor Prof. Susan Schorr for this amazing project. Thanks for giving me the opportunity to work on it and for granting me all the freedom and idea with the research. Furthermore, I very much appreciate the guidance you have given me in terms of professionalism and behavioural patterns, teaching me how to approach research rigorously.

I would like to express my gratitude to Dr. Joachim Breternitz, my daily supervisor, for all the time you spent tutoring and teaching me about all the small details in the lab, discussing new ideas or outlines for the thesis, and for all the funny and philosophical anecdotes. You were very encouraging, and your enthusiasm for research was always inspiring.

I also acknowledge the MatSEC for the funding I obtained for the doctoral position.

I should also mention all of the colleges in our group SE-ASD that made the work in Berlin enjoyable and worthwhile. René Gunder, thank you for showing me the Rietveld and Le Bail method and sending me the first starting input file, and thank you so much for the help while the XRD devices were in error. Dr. Galina Gurieva, thank you for the lab introduction and the advice about how to write a thesis efficiently. Lar Steinkopf, thank you so much for the instruction of the XRF device. Dr. Lars Choubrac, thank you so much for the test measurement with Raman and PL. Many thanks to Dr. Daniel Abou-Ras for the test measurement with EDS. I also would like to give my thanks to Dr. Daniel Fritsch for the discussion and help on DFT calculations. Furthermore, special thanks go to Dr. Alexandra Franz for the help of the neutron diffraction experiment at E9 and Dr. Daniel Többens for data analysis guidance. Many thanks to Dr. Daniel Abou-Ras for the test measurement with EDS.

I owe my gratitude to Dr. Stefan Berendts and Prof. Martin Lerch for supporting chemical analysis at TU Berlin, which is of great importance for this work. Further acknowledgement is due to Dr. Stanislav Savvin for the beamtime of D2B@ILL.

Apart from that, I want to thank the colleges who were PhD students in the group and shared the same office with me. Dr. Julien Marquardt, Dr. Frederike Lehmann and Dr. Sara Niedenzu, thanks so much for the advice at the beginning of my PhD and it helped

me so much to adapt to the new atmosphere. And also many thanks to Ana and David for inviting for a coffee using your new coffee machine in the office.
Special thanks to my wife, Liu, who encouraged and accompanied me when I was most confused and depressed. Thank you for keeping my faith in myself and still facing life with optimism.
最后，感谢我家人给我支持和理解，爱你们。

Abstract

This work is motivated by the increasing concern on novel earth-abundant and low-cost semiconductors to meet the growing demand in industry, such as solar cell applications.

Since Zn-IV-N_2 (IV: Ge, Sn) are widely reported as earth-abundant semiconductors, which allow excellent bandgap energy tuning, these materials are being considered as promising candidates for solar cells. In addition to alloying the group IV elements, an interesting bandgap tuning mechanism through the cation disorder in these materials is postulated by many calculation studies. The cation disorder arises as an interesting question because cation in this material can have different arrangements that lead to two possible crystal structures. One is the wurtzite-type structure, in which cations are disordered, sharing one 2*b* Wyckoff site, and the other is the β-$NaFeO_2$-type structure, in which cations are ordered in the structure, distributed on two different 4*a* Wyckoff sites.

Change in the crystal structure based on cation disorder naturally affects the material properties essential for solar energy harvesting. Though numerous studies computationally predict the wurtzite-type structure and the β-$NaFeO_2$-type structure for Zn-IV-N_2 (IV: Ge, Sn), the compelling experimental validation of the cation disorder effect on the crystal structure transformation is still lacking.

The well-crystallised bulks (signal crystal, powder) are ideal for the study of crystal structure and cation disorder based on diffraction methods. However, bulk Zn-IV-N_2 are challenging to prepare, particularly the $ZnSnN_2$ due to its shallow formation energy. Therefore, the synthesis of well-crystallised bulk material is one of the challenges in the experimental investigation of crystal structure and cation disorder.

Allowing oxygen content in the nitrides (avoiding oxygen in nitrides is a challenge), one could achieve the synthesis of $Zn_{1+x}IV_{1-x}(O_xN_{1-x})_2$ (IV: Ge, Sn) powders, which can crystallise in the wurtzite-type structure and the β-$NaFeO_2$-type structure, similar to Zn-IV-N_2 (IV: Ge, Sn). Therefore, this work attempts to study $Zn_{1+x}IV_{1-x}(O_xN_{1-x})_2$ (IV: Ge, Sn) as the exemplary system to understand the similar cation disorder effect in Zn-IV-N_2 (IV: Ge, Sn).

This thesis optimises the synthesis method for $Zn_{1+x}Ge_{1-x}(O_xN_{1-x})_2$. The nature of the reaction mechanisms is studied by correlating chemical composition obtained by X-ray fluorescence spectroscopy (XRF) and hot gas extraction method (HE) with reaction conditions, hence realising a targeted synthesis of phase-pure $Zn_{1+x}Ge_{1-x}(O_xN_{1-x})_2$ powders with varying compositions. An evident transformation of crystal structure between the wurtzite-type structure and the β-$NaFeO_2$-type structure is observed.

The experimental investigation of cation disorder in $Zn_{1+x}Ge_{1-x}(O_xN_{1-x})_2$ is achieved by using X-ray and neutron diffraction. Simultaneous Rietveld refinement was performed to characterise the site occupancy factor to understand the degree of cation disorder. Moreover, the bandgap tuning mechanism is investigated by correlating optical bandgap energy measured by the UV-Vis method, with chemical composition, crystal structure, and cation disorder studies.

Furthermore, this thesis introduces a new synthesis method for $Zn_{1+x}Sn_{1-x}(O_xN_{1-x})_2$ powder. This method achieves the synthesis of well-crystallised phase-pure $Zn_{1+x}Sn_{1-x}(O_xN_{1-x})_2$ with a large composition range under ambient pressure, allowing the investigation of crystal structure and cation disorder based on PXRD. The crystal structure of $Zn_{1+x}Sn_{1-x}(O_xN_{1-x})_2$ is evaluated by the Rietveld refinement of the XRD data. Moreover, the optical bandgap energy analysis was performed using the UV-Vis method. This work suggests an indirect band transition of the wurtzite-type $ZnSnN_2$ by combing the crystal structure study and the bandgap energy analysis.

Altogether, this work draws insight into the relationship among crystal structure, cation disorder and optical bandgap energy for $Zn_{1+x}IV_{1-x}(O_xN_{1-x})_2$ (IV: Ge, Sn). The results facilitate developing the high-efficient solar cell based on these novel materials in the future.

Contents

List of Figures

List of Table

Chapter I

Introduction

1.1 A gift from the sun

Among the many new technologies for power generation, photovoltaic technology has been considered one of the most representative ways of sustainably harvesting energy. The near-infinite availability of sunlight endows the photovoltaic technology with an inherent advantage that is unmatched by other alternatives. A solar cell is a photovoltaic device that directly converts solar radiation into electrical energy. The direct conversion of solar radiation into electrical energy avoids unnecessary energy losses caused by converting the energy via different intermediate forms into electrical energy. As global energy demand increases year on year, the abundance of solar photovoltaic energy will be ideal for meeting global energy needs and making more efficient use of the gift from the sun.

1.2 Absorber materials for solar cells

A solar cell is basically a p-n junction diode made from semiconducting materials. According to the main charge carrier types, semiconducting materials can be classified into n-type (electrons) or p-type (holes). When sunlight hits a semiconducting material with the appropriate band gap energy, electrons in the valence band gain energy to leap into the conduction band, and pairs of charge carriers (electron-hole pairs) emerge. Due to the potential barrier caused by the p-n junction, electrons can only flow from the p-type to the n-type semiconductor, while holes move in the opposite direction. The electron is enriched towards the n-type semiconductors and holes towards the p-type, hence voltage on two ends - the photovoltaic effect. Since the photovoltaic effect that light converts into electric powder occurs on the semiconductors, these materials are also known as absorber materials in solar cells, and their bandgap dominates the conversion efficiency limits of single-junction solar cells (Figure 1) according to Shockley and Queisser.[1-4]

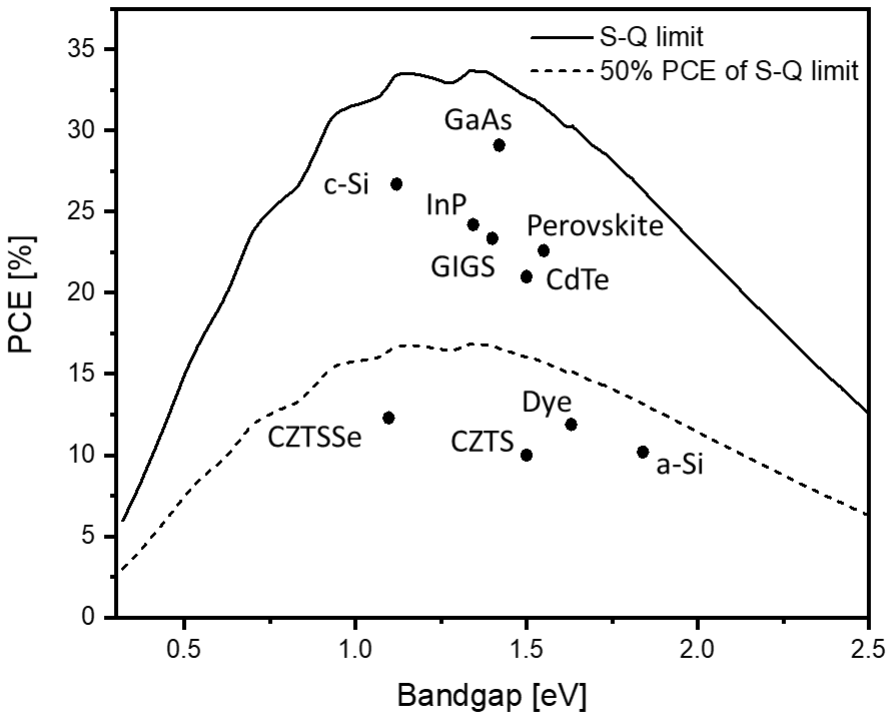

Figure 1 Fundamental solar cell efficiency due to Shockley-Queisser limits and present-day records. Theoretical Shockley-Queisser detailed-balance efficiency limit as a function of bandgap (black line), and 50% of the limit (dash lines). The record efficiencies for different materials[5] are plotted for the corresponding band gaps (c-Si[6], a-Si[7], GaAs[8], InP[9], GIGS[10], CdTe[11], Dye[12], CZTS[13], CZTSSe[14], Perovskite[15, 16]).

As the prevalence of photovoltaic technology increases, the energy obtained through photovoltaic technology has exploded in the last few years.[17] The worldwide market for photovoltaic power generation totalled 131 GW in 2019, with the European market generating more than 12% of the global total.[18] The vast, rapidly developing market has resulted in an explosion in industrial demand for photovoltaic devices. Consequently, concerns about the scarcity of sourced raw materials, production costs and environmental impact have led to research into novel absorber materials suitable for use in photovoltaic equipment of large scales.

At present, silicon-based semiconducting material has dominated photovoltaic applications due to its abundance in the earth's crust and established manufacturing processes. For example, crystalline silicon (c-Si) solar cells account for over 90% of the total market share of photovoltaic production.[18] Although silicon-based photovoltaic materials are widely accepted in today's global market, as for the material itself, the non-ideal indirect bandgap of silicon (1.1 eV) limits their theoretical

conversion efficiency, according to the Shockley-Queisser limit.[19] The absorber layer for these solar cells in the industry is made of high-purity monocrystalline silicon rods. For one thing, the extraction of high purity crystalline silicon from silicon dioxide requires exceptionally high temperatures, and the production process is energetically costly. For another, the manufacturing process limits the thinness of the absorber layer, which is mainly greater than 200 microns. Thus, monocrystalline silicon solar cells consume a large amount of semiconductor material compared to thin-film solar cells. However, if thin-film preparation processes are used to reduce material costs for Si-based solar cells (e.g. thin-film minimodule c-Si cell or amorphous-Si solar cell), the photovoltaic conversion efficiency plummets over 50% compared to the c-Si solar cell.[5]

Other high-performance photovoltaic materials often contain low-abundant or toxic ions such as expensive Ga, In in III-V materials (III: group III elements such as Ga, In, Al; V: group V elements such as As, P) and chalcogenide thin-film solar cells (such as $Cu(In,Ga)Se_2$ (CIGS) solar cell), toxic and scared ions in CdTe and toxic Pb ion in halide Perovskites.[20]

These drawbacks have moved research into novel earth-abundant semiconductors, which might bring a low-cost, environmentally friendly solution to the material consumption in solar cell manufacturing and problematic ions currently used for high-performance photovoltaic devices. A strategy for deriving earth-abundant alternatives is replacing problematic elements in the high-performance photovoltaic materials with earth-abundant ones. For example, earth-abundant alternatives of the high-performance photovoltaic materials presently being extensively researched include Cu_2-II-IV-VI_4 (II: elements such as Zn, Fe; IV: group IV elements such as Sn, Ge; VI: group VI elements such as S, Se) as derivatives of CIGS.[21-23] It can be thought of that the trivalent cations (In^{3+}, Ga^{3+}) are replaced with a combination of divalent (Zn^{2+}, Fe^{2+}) and tetravalent (Sn^{4+}, Ge^{4+}) cations. In addition to the cost of materials, the environmental friendliness of earth-abundant alternatives can reduce the cost of cumbersome packaging or device handling.

Notably, researchers are currently actively developing the efficiency of these earth-rich alternatives so that they can one day be rolled out on a large scale to replace expensive or toxic target materials.[20] There are still fundamental unanswered questions about these earth-abundant materials. Therefore, an in-depth study of these earth-abundant

semiconductor materials and the improvement of their material properties are crucial to solving the future challenges facing the photovoltaic industry and the world's energy needs.

1.3 Zn-IV-N_2 (IV: Ge, Sn): earth-abundant ternary nitride for solar cells

1.3.1 A novel ternary nitride family: Zn-IV-N_2 (IV: Ge, Sn)

Since the 20th century, nitride materials have attracted increasing attention.[24-27] One famous binary nitride family, which greatly influenced the laser and electronics industry, might be the group III-nitrides (III: Al, Ga, In). The Nobel Prize in physics in 2014 was awarded to Shuji Nakamura, Hiroshi Amano and Isamu Akasaki, inventors of the group III-nitride based blue LED. These group III-nitride are currently widely used in numerous fields such as laser devices,[28] power electronics.[29] Because group-III nitrides have excelled in light-emitting applications related to converting light into electricity, they have also been considered promising for photovoltaic applications, the reverse conversion process of the former.[30-35]

With the increase in the utility of group III-nitrides, the supply of group III elements (i.e. Ga, In) has also become an issue that cannot be ignored. By considering a similar strategy discussed above between Cu_2-II-IV-VI_4 and CIGS, one has Zn-IV-V_2 (IV: group IV elements such as Ge, Sn; V: group V elements such as N, P) as derivatives of III–V semiconductors.[36-38]

This new class of materials fulfils the criteria of prevalence and non-toxicity of cations. As Zn-IV-nitrides (IV: Ge, Sn) are structurally analogous to III-nitrides, it is postulated that this newly derived binary nitride family can have a similar optical bandgap range and absorption performance as III-nitrides, hence the potential for light-emitting or photovoltaic applications.[38] Besides, the extra cation type in Zn-IV-nitrides provides an additional degree of freedom that makes the cation disorder an interesting topic, which is one of the focuses to be discussed in this thesis.

1.3.2 Brief research history and timeline of the development

This section introduces a brief research history and timeline of the development of Zn-IV-N_2 (IV: Ge, Sn), particularly the preparative basis and theoretical perspectives. The crystal structure studies in these materials are shown in the timeline (Figure 2). Studies of structure-property tuning strategies of these ternary nitrides are emerging. However, many of these studies are still theoretical or early-stage. Nonetheless, there is a huge opportunity space to promote the structure-property study of these ternary nitrides, as many experimental validation efforts need to be advanced. We hope this section provides readers with an overview of the Zn-Group IV-nitride (IV: Ge, Sn) materials.

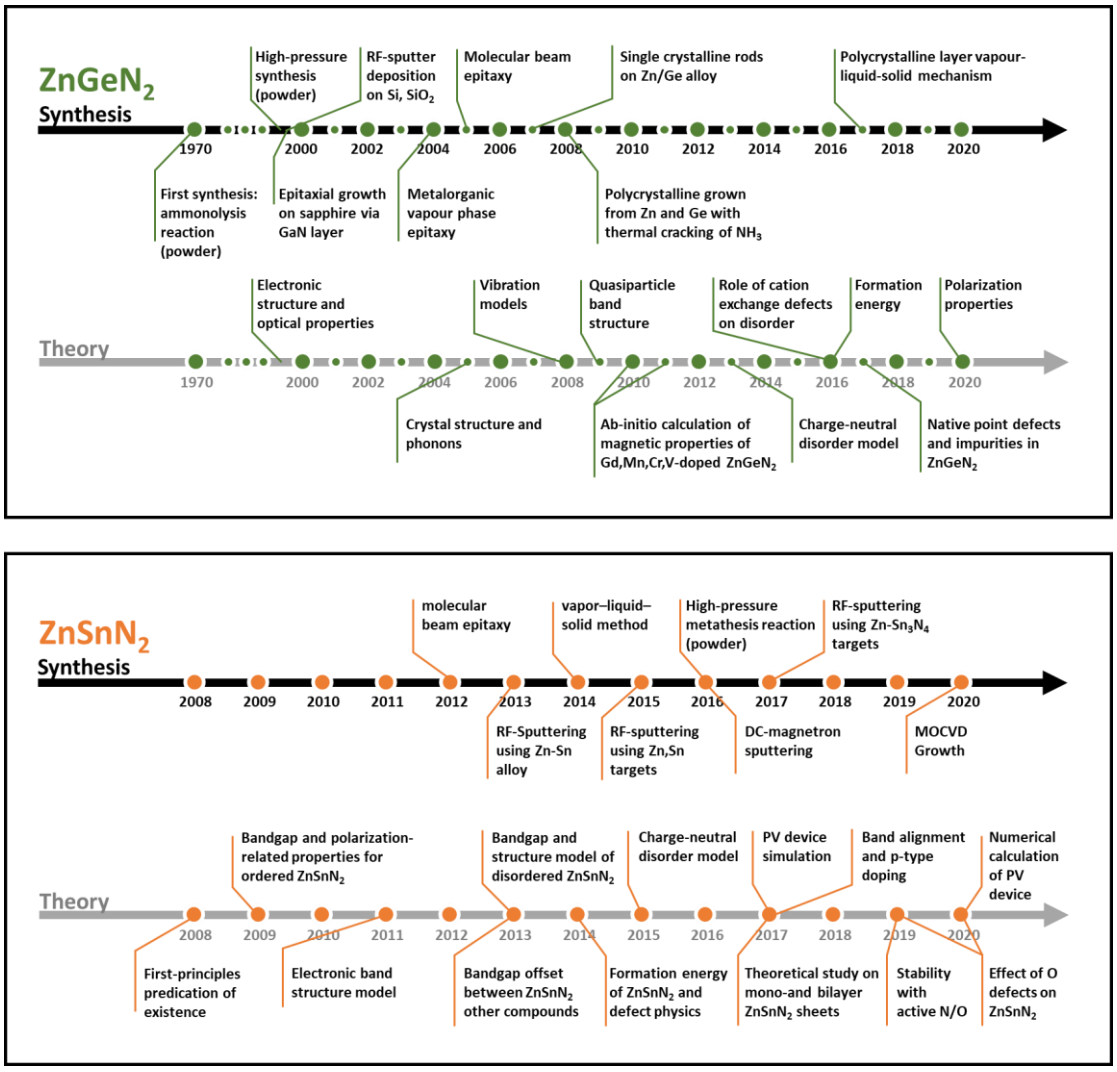

Figure 2 Critical milestones in the timeline of $ZnGeN_2$ and $ZnSnN_2$ synthesis and theoretical research.

From the 1970s to the 1990s, there were few studies of Zn-IV-N_2 (IV: Ge, Sn).[39-41] Early works by a few research groups were limited to synthesis and basic crystal structural characterisation of $ZnGeN_2$.[39,41] Breakthroughs in synthetic methods motivate the study of $ZnGeN_2$ that the number of reports about $ZnGeN_2$ increases as the synthetic techniques such as the high-pressure metathesis method,[41-43] ammonolysis approaches through oxide precursors[44] under ammonia,[45-49] reactive sputtering technique[36, 49, 50] and novel epitaxial growth,[44, 51, 52] were used in exploratory syntheses. Moreover, with the rise of the computational study of materials, the potential material properties of $ZnGeN_2$ suitable for photovoltaic applications predicted by theoretical calculations[44, 53-55] has driven the expansion of research that continues into the 21st century.

Research on $ZnSnN_2$ compounds started later than on $ZnGeN_2$. The existence of $ZnSnN_2$ was first predicted in 2008 by computational study.[54] After that, the same group that first predicted the existence of $ZnSnN_2$ postulated the bandgap of $ZnSnN_2$ through DFT calculations in 2009.[56, 57] In the early stages, theoretical studies on $ZnSnN_2$ were far ahead of experimental progress since $ZnSnN_2$ has very shallow formation energy; hence a low decomposition temperature, challenging to be synthesised.[58] The interest in $ZnSnN_2$ has increased rapidly since 2012 due to the experimental breakthrough of the $ZnSnN_2$ epitaxy layer.[59] The bandgap of $ZnSnN_2$ is postulated to vary between 1.12 eV and 2.09 eV.[60] This bandgap region is very promising for absorbers in solar energy harvesting applications, according to the Shockley-Queisser equation (Figure 1).[4, 19]

$ZnGeN_2$ and $ZnSnN_2$ are unique because they provide a new cation-disorder-based bandgap tunning mechanism, in addition to doping with other elements or alloying with other compounds.[56, 61-63] This unique mechanism spurs the studies of crystal structure and cation arrangement of these compounds. While one can find various reports of the crystal structures of $ZnGeN_2$ and $ZnSnN_2$ in literature, the study on the cation disorder effect is mainly based on computational studies or at the early stages of experimental investigation. Thus, an in-depth understanding of cation arrangement in the corresponding crystal structures and their relationship is essential to promoting the research on these ternary nitrides and facilitating the design of material properties.

1.4 Crystal structure and cation disorder of Zn-IV-N_2 (IV: Ge, Sn)

As discussed above, Zn-IV-N_2 (IV: Ge, Sn) are structurally analogous to group-III nitrides through the replacement of group III atoms with heterovalent Zn^{2+} and group IV ions. The additional cation type with different oxidation states results in the complexity of crystal structures.

When cations adopt a statistical cation distribution in Zn-IV-N_2 (IV: Ge, Sn), the materials crystallise in the hexagonal wurtzite-type structure (space group $P6_3mc$), where cations share one Wyckoff position 2*b*, analogous to the case in the group III-nitrides (Figure 3, bottom left). On the other hand, having divalent and tetravalent cations instead of having only trivalent cations in the compounds raises the question of cation ordering related to the arrangement of cations in the crystal structure. This is because there are several possibilities to achieve the arrangement of ordered cations from the structural point of view.[64]

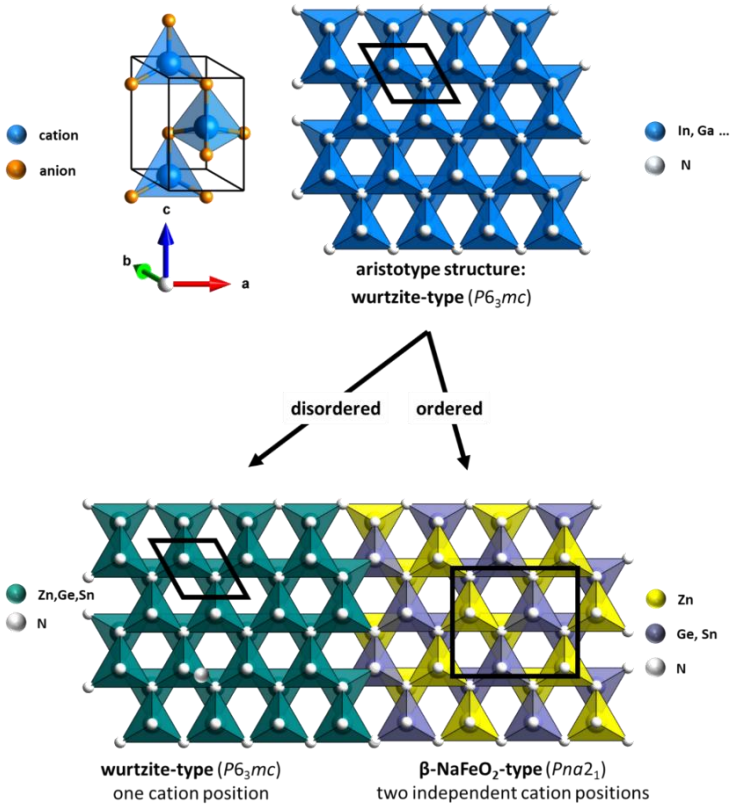

Figure 3 General atomic arrangement in the wurtzite-type structure (top left) and the atomic arrangement of wurtzite-type (In, Ga)N, view on the ***ab***-plane (top right). The atomic arrangement of disordered Zn-IV-N_2 (IV: Ge, Sn) (bottom left) and ordered Zn-IV-N_2 (IV: Ge, Sn), view on the ***ab***-plane (bottom right).

Historically, the first evidence of cation ordering in Zn-IV-N_2 (IV: Ge, Sn) was observed using neutron diffraction of powder $ZnGeN_2$ by Wintenberger et al. in 1973. [40] Their work proposed the orthorhombic β-$NaFeO_2$-type structure (space group *Pna*2_1) for $ZnGeN_2$ (Figure 3, bottom right) in addition to the wurtzite-type structure and opened the discussion on the cation disorder in Zn-IV-N_2 (IV: Ge, Sn).

The disorder-order problem for heterovalent cations in Zn-IV-N_2 (IV: Ge, Sn) involves Pauling's second rule that the sum of the bond strengths (*s*) of all the ions coordinated around a central ion equals the bond strength of the central ion.[65, 66]

$$\sum s_{surround} = s_{central}$$

The bond strengths is defined by Pauling as:

$$s = \frac{z}{c} \tag{1.1}$$

where *z* is the cation charge and *c* is the cation coordination number.

According to Pauling, for Zn-IV-N_2 (IV: Ge, Sn), the coordination number of Zn^{2+} and Ge^{4+} is four (Figure 3) so that:

$$s(\mathrm{Zn}^{2+}) = \frac{2}{4} = \frac{1}{2} \tag{1.2}$$

$$s(\mathrm{Ge}^{4+}) = \frac{4}{4} = 1 \tag{1.3}$$

Because N^{3-} is defined as the centred anion, the sum of the electrostatic bond strength to N^{3-} equals its charge.

$$s(\mathrm{N}^{3-}) = 3 \tag{1.4}$$

The sum of the strengths of the electrostatic bonds to an anion equals the charge on the anion:

$$num(\mathrm{Zn}^{2+}) \times s(\mathrm{Zn}^{2+}) + num(\mathrm{Ge}^{4+}) \times s(\mathrm{Ge}^{4+}) = s(\mathrm{N}^{3-}) \tag{1.5}$$

$$num(\mathrm{Zn}^{2+}) + num(\mathrm{Ge}^{4+}) = 4 \tag{1.6}$$

where *num*(Zn^{2+}) and *num*(Ge^{4+}) are the numbers of the Zn^{2+} and Ge^{4+} surrounding an N^{3-}. By solving the equations, one obtains *num*(Zn^{2+}) = 2 and *num*(Ge^{4+}) = 2. Thus, each N^{3-} should bond to two Zn^{2+} and two Ge^{4+}, preserving the overall charge neutrality.

The arrangement of cations in an ordered structure is also conceivably described in some literature using the octet rule.[65, 66]

The two possible structures to allow cation ordering preserving Pauling's rule are the orthorhombic β-$NaFeO_2$-type structure (space group: $Pna2_1$), where the cations occupy two distinct Wyckoff positions *4a*[40, 44, 67], and another case (space group: $Pmc2_1$) with higher-symmetry than the former. The $Pmc2_1$ case once puzzled the academic community since it has higher symmetry than the $Pna2_1$ case but has never been observed experimentally. In 2020, Breternitz et al. interpreted from the pure crystallographic point of view that the symmetry in $Pmc2_1$ leads to identical tetrahedron sizes for different cations, which is hardly energetically favourable.[67]

Experimental studies consistently reported that ordered $ZnGeN_2$ crystallises in the orthorhombic β-$NaFeO_2$-type structure,[68, 69] consistent with the computational prediction that the β-$NaFeO_2$-type structure is energetically favourable.[65] However, most experimental findings demonstrated that the crystal structure of $ZnSnN_2$ is wurtzite-type, with no obvious evidence of cationic ordering[43, 70, 71], only a few studies suggested that they found clues that $ZnSnN_2$ might crystallise in the orthorhombic structure.[72, 73] No compelling experimental evidence for the β-$NaFeO_2$-type structure for $ZnSnN_2$ has been observed so far, although the β-$NaFeO_2$-type structure has been postulated to be thermodynamically stable based on computational studies for $ZnSnN_2$.[65, 74]

Another point still unclear about the crystal structure of Zn-IV-N_2 (IV: Ge, Sn) is the local arrangement of cations in the wurtzite-type structure. While earlier studies assumed statistic cation distribution for disordered Zn-IV-N_2 (IV: Ge, Sn),[36, 42, 60] DFT calculations indicated that a statistic cation distribution would locally violate Pauling's principle and be energetically very costly.[74, 75] A conceivable interpretation has been proposed by Quayle et al. that the disordered structure might be a puzzle-like mixture of two different charge-neutral fragments ($Pna2_1$ and $Pmc2_1$) complying with the octet rule and still has violation at the interfaces.[65] However, conclusive experimental evidence of the puzzle-like model is still missing. Moreover, the extent of intentional or unintentional oxygen incorporation and its effect on formation energy, crystal structure and local disorder moved into focus in very recent literature.[76-78] While O_N defects and their local coordination significantly influence the phase stability and

material properties of compounds,[79-81] the studies of oxygen incorporation in Zn-IV-N_2 (IV: Ge, Sn) are often under-report in previous literature.

1.5 Challenges and strategies in experimental investigation of crystal structures of Zn-IV-N_2 (IV: Ge, Sn): Significance of synthesising bulk samples

Experimental studies on the crystal structure of materials generally rely on well-crystallised samples. At present, the synthesis of Zn-IV-N_2 (IV: Ge, Sn) is a relatively young field, particularly for $ZnSnN_2$, which was first synthesised in 2012. Zn-IV-N_2 (IV: Ge, Sn) specimens can be classified according to their macroscopic morphology: thin films, powder materials. While thin-film preparation techniques have developed rapidly, bulk materials (single crystal and powder) are more favourable for studying crystal structure. The high crystallinity, the large volume of bulk sample can avoid noise caused by the substrate and provide other potent characterisation possibilities for crystal structure, such as neutron diffraction.

The major problem of synthesising bulk Zn-IV-N_2 (IV: Ge, Sn) is the narrow stable region of these nitrides, which is affected by the chemical potential of nitrogen (μ(N)).[58, 82, 83] The paradox is that, on the one hand, synthesising bulk materials usually requires increasing temperature for mass transport, leading to a decrease in μ(N). On the other hand, the formation energy of these nitrides increases as the μ(N) decreases so that the compounds are going to be energetically unfavourable.

Another relevant challenge is that traces of oxygen are present in virtually any nitride material. There are two sides to a story, and challenges and opportunities coexist. While the structural investigation becomes even more complex due to oxygen impurities in the crystal structure, allowing oxygen in the compounds might decrease the formation energy,[78] hence stabilising the compounds. Therefore, we study the exemplary Zn-IV-O-N (IV: Ge, Sn) system, which might facilitate deconvoluting the crystal structure and similar disorder effect in pure nitride.

1.6 Space group relationship of the wurtzite-derived system in Zn-IV-N_2 (IV: Ge, Sn)

This section discusses the group-subgroup relationship between the wurtzite-type structure and the β-$NaFeO_2$-type structure in Zn-IV-N_2 (IV: Ge, Sn). For the Zn-IV-N_2 (IV: Ge, Sn), the hexagonal wurtzite-type structure (space group $P6_3mc$) is the aristotype that is a high-symmetry crystallographic structure type, also known as basic structures. The β-$NaFeO_2$-type structure (space group $Pna2_1$) is the hettotype, the lower-symmetry variant; it can be thought of as the derivative structure from the aristotype. One can access the hettotype from the aristotype type by stepwise descents of structural symmetry. Herein, we use the Bärnighausen tree[84] as a powerful tool to present the group-subgroup relationship and understand the stepwise descents of structural symmetry of Zn-IV-N_2 (IV: Ge, Sn).

Figure 4 exhibits a brief graphical representation of the group-subgroup relationship between the space group $P6_3mc$ and $Pna2_1$ involving intermediate subgroups that could relate to the transformation. It is worth noting that the following chains between $P6_3mc$ and $Pna2_1$ show the path that crystal structure transformations could follow; however, no experimental evidence of a Zn-IV-N_2 (IV: Ge, Sn) obeying these intermediate space groups have ever been observed so far. Nonetheless, they serve as conceivable chains to reflect the symmetry relationship between different crystal structures. Here we will discuss the path depicted by the bold black arrow as an example.

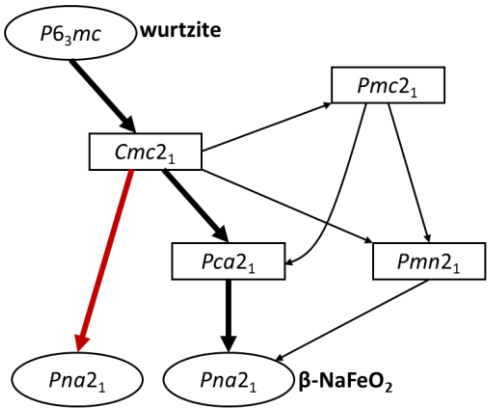

Figure 4 A brief graphical representation of the group-subgroup relationship between P6_3mc and $Pna2_1$ involving intermediate subgroups that could relate to the transformation (scheme on the left). The arrows link space groups and their maximal subgroups. The broad black arrows represent the transformation chain presented in Figure 5. The red arrow represents the direct transformation from $Cmc2_1$ to $Pna2_1$ without intermediate space groups.

The most distinguishing feature of the wurtzite-type structure from the ordered β-$NaFeO_2$-type structure is the 6_3-screw axis (Figure 5a, hexagonal symbol), which is the criterion for the hexagonal crystal system. Due to the 6_3-screw axis, the cation must be on the central axis of the triangular pyramid tetrahedron (Figure 5a). Cations and anions are on *2b* sites with coordinates (1/3, 2/3, z). The sites are fixed in the *x* and *y* direction and free for moving along the *c*-axis.

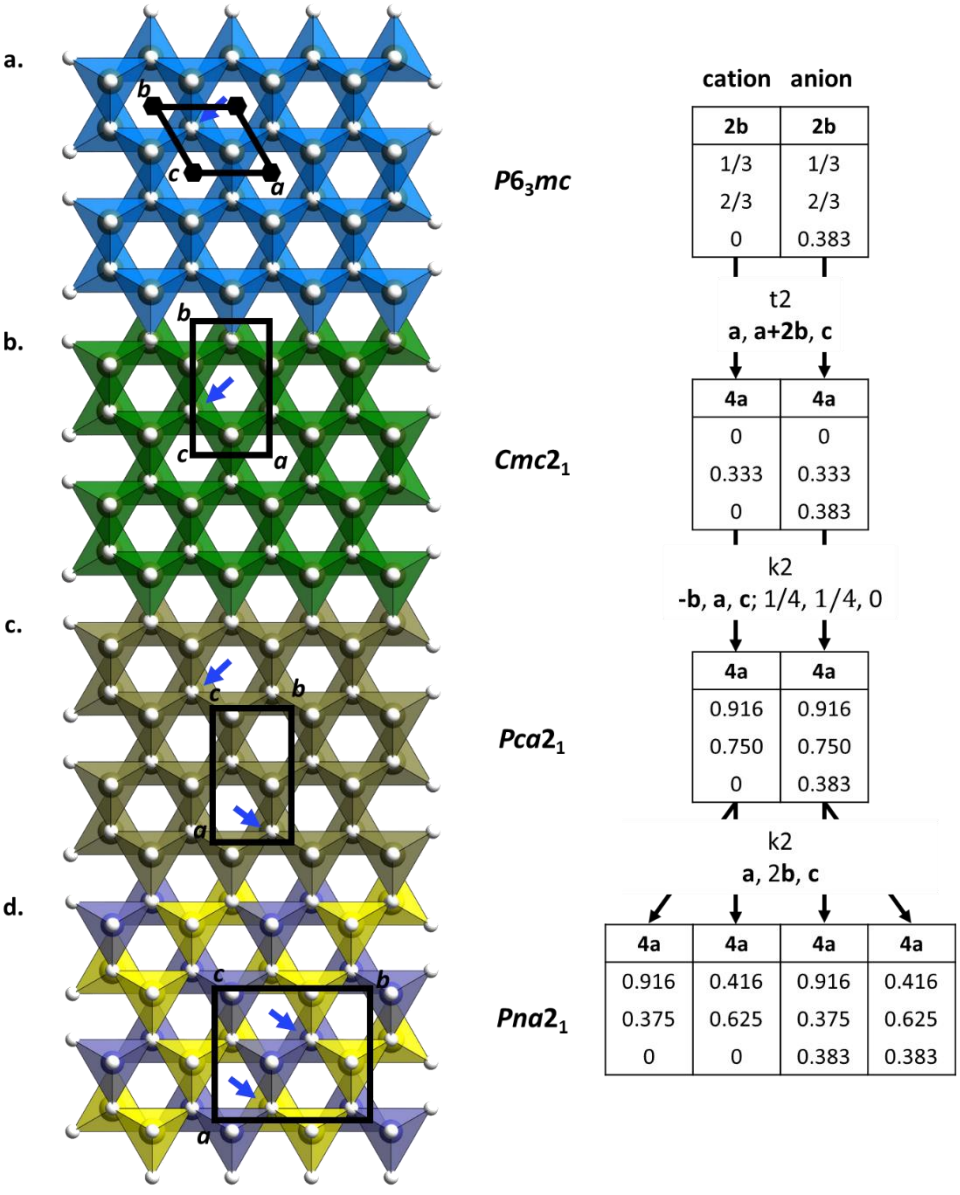

Figure 5 Bärnighausen tree for the space group relationship between the wurtzite-type structure and the β-$NaFeO_2$-type structure. The transformation of the basis vector is given below the maximal subgroup-type symbol and index (left-hand side table). The transformation of the crystal structure is illustrated in the schema on the right-hand side. Cations are displayed in the polyhedral form. The blue arrows in the figures indicate the positions of the cations corresponding to the cation coordinates in the tables.

The space group *Pna*2$_1$ is not the maximal subgroup *P*6$_3$*mc*. Therefore, it is important to find out the intermediate space groups to fill the sequential steps of the transformation chain. The first step is the transformation of the wurtzite-type structure (space group *P*6$_3$*mc*) into a *translationengleiche* maximal subgroup in *Cmc*2$_1$. The term "*translationengleiche*" means in German "with the same translation". This type of subgroup retains translational symmetry of the space group, accompanied by a change in the crystal class. The transformation matrix ***a***, ***a***+2***b***, ***c*** is symbolised in the Bärnighausen tree in Figure 5. The variation of the unit cell and basis vectors is indicated on the right-hand side of Figure 5. While the basis vectors ***a***, ***c*** and the origin point remain, the new basis vector ***b′*** is obtained by vector operation ***a***+2***b*.** The unit cell size is doubled. The Wyckoff position 2*b* in the wurtzite-type structure changes into 4*a* position in the new unit cell. In Cmc2$_1$, 4*a* site is on position (0, *y*, *z*). The 4*a* site is on the mirror plane perpendicular to the *a*-axis so that the atomic coordinate is fixed in *x* and free in *y* and *z*. Thus, the triangular pyramid can be distorted into a disphenoid.

It is worth noting that the space group *Pna*2$_1$ is one of the maximal subgroups of the space group *Cmc*2$_1$ so that a direct transition from *Cmc*2$_1$ to *Pna*2$_1$ is possible (Figure 4, red arrow). However, the crystal structure remains only two independent crystallographic sites through this transformation, one for the anions and one for the cations (Figure 6). Therefore, for Zn-IV-N$_2$ (IV: Ge, Sn), the different cations are still forced to share one position, preventing cation ordering.

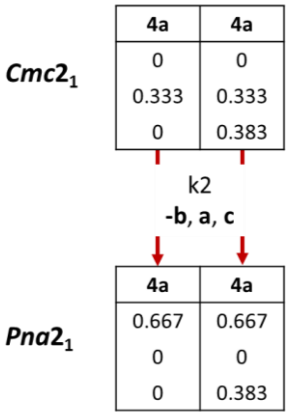

Figure 6 The transformation matrix and atomic coordinates for the direct transformation from *Cmc*2$_1$ to *Pna*2$_1$ without intermediate space groups.

Introducing an intermediate step via the space group *Pca*2$_1$ can achieve the splitting of the cation site. *Pca*2$_1$ is the maximal *klassengleiche* subgroups of the space group

Cmc2_1. German *klassengleiche* means “of the same class”. In this case, the group and the subgroup belong to the same crystal class. The transformation matrix ***-b***, ***a***, ***c***; 1/4, 1/4, 0 from *Cmc*2_1 to *Pca*2_1 is shown in the Bärnighausen tree in Figure 5. The symmetry elements no longer constrain any coordinate of the sites so that they can reflect the freely moving of atoms in any direction in the unit cell.

The last complexity arises from the transformation from the structure in space group *Pca*2_1 to the β-$NaFeO_2$-type structure in its *klassengleiche* subgroup *Pna*2_1 with a unit cell twice as large as that of the former. The most distinguishing feature of this step is that the two crystallographic sites split into four sites. Two of them are for cations, allowing ordered accommodation of Zn and the other group-IV atom in the crystal structure.

1.7 Scope of this thesis

The cation disorder effect associated with crystal structure and defects in Zn-IV-N_2 (IV: Ge, Sn) remains poorly understood, and in particular, the experimental investigations and verification of these materials remain challenging. Thus, experimental research on the crystal structure and cation disorder is essential to understand the structure-related property and the structure-property relationship in order to develop this class of novel materials further.

This thesis emphasises the study of crystal structure and disorder effects, as they are crucial to the material properties and significantly influence the prospects of these materials in photovoltaic applications. The basic principle of characterisation techniques, including X-ray diffraction, neutron diffraction technique and data analysis method (refinement of diffraction data), is introduced in Chapter II. Chapter III focuses on the synthesis and experimental results from crystal structural investigations on the Zn-Ge-O-N system, followed by a comprehensive discussion on the chemical reaction mechanism, the structure transformation, the cation disorder and bandgap tunning. Further, Chapter IV presents a new method for synthesising Zn-Sn-O-N powders and discuss the study of crystal structure and optical properties. Finally, the results and findings from this dissertation will be concluded in Chapter V, followed by the outlook and speculate on further research directions for these material systems.

Chapter II

Analytical techniques

2.1 Determination and analysis of crystal structure

In 1912, Max von Laue discovered a distinct diffraction phenomenon by irradiation of materials with X-ray beams.[85] As diffraction is a typical property of waves, his finding first confirmed the wave nature of X-ray. [85, 86] Furthermore, his discovery exposed the periodic arrangement of atoms in a material since periodically arranged scattering points in space are the prerequisite for interference phenomena. Based on Laue's findings, William Lawrence Bragg and his father William Henry Bragg experimented with X-ray diffraction to elucidate crystal structures of materials,[87-89] opening the experimental investigation of crystal structure using the diffraction method as a powerful tool.

In the following sections, we will first briefly describe the nature of diffraction. This is followed by introducing the geometrical conditions respected with measurable Bragg peaks in diffractograms. Finally, we introduce the analytic methods and strategies for diffraction patterns of polycrystalline powders used in the present work.

2.1.1 Nature of diffraction

Geometric condition of diffraction methods

According to Laue, the diffraction signals can be observed if the geometric configuration preserves Laue's condition[90]. When describing the detectable diffraction peak positions of a crystalline material, Laue's condition can be expressed in a form equal to the well-known Bragg's law as shown in Equation 2.1. λ is the wavelength of the incident radiation, *d* is the interplanar distance of the crystal plane *hkl*, θ is the diffraction angle, and n is an integer. The geometrical illustration of Bragg's law is shown in Figure 7.

$$n\lambda = 2d \sin\theta \qquad 2.1$$

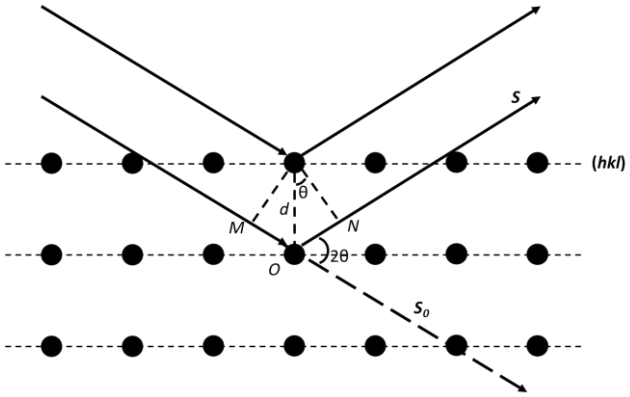

Figure 7 Geometrical illustration of Bragg's law. Interference radiation by crystalline material.

Structure factor of X-rays diffraction and neutron diffraction

X-rays scattering by crystalline materials can be thought of as scattering by all the atoms in the material. When each atom is taken into account, the scattered waves mutually interfere, being associated with large numbers of phase shifts. The phase for coherent scattering is by conversion related to that of the scattering vector $\boldsymbol{q}$ with

$$\boldsymbol{q} = 2\pi(\boldsymbol{s} - \boldsymbol{s_0})/\lambda \qquad 2.2$$

and the relative geometrical positions of atoms $\boldsymbol{r_j}$ in a crystal plane. Therefore, the structure factor (F_{hkl}) is defined to describe the resultant of all waves scattered in the direction of the *hkl* reflection by the atoms contained in the unit cell and can be expressed as follow:

$$F_{hkl} = \sum_{j=1}^{J} f_j \exp\left(i\boldsymbol{q} \cdot \boldsymbol{r_j}\right) \qquad 2.3$$

In the formula, *j* represents the atoms in the unit cell. f_j is the atomic form factor or called X-ray form factor, which is the Fourier transform of the electron density of an atom describing the ability of scattering of X-ray by all electrons in an atom, $\boldsymbol{q}$ is the scattering vector, $\boldsymbol{r_j}$ represents the geometrical positions of atoms.

While the position of the atoms $\boldsymbol{r_j}$ can be described by their fractional coordinates (x_j, y_j, z_j) associating with basis vectors: $\boldsymbol{r_j} = x\boldsymbol{a} + y\boldsymbol{b} + z\boldsymbol{c}$, the scattering vector $\boldsymbol{q}$ for conditions preserving Bragg's law is: $\boldsymbol{q} = 2\pi(h\boldsymbol{a}^* + k\boldsymbol{b}^* + l\boldsymbol{c}^*)$. Thus, the structure factor can be expressed as:

$$F_{hkl} = \sum_{j=1}^{J} f_j \exp\left[i2\pi(hx_j + ky_j + lz_j)\right] \qquad 2.4$$

The conceptual experiment and theory are similar for neutron diffraction and X-ray diffraction. The differences are the physics of the interactions of X-rays (electro-magnetic radiation) versus neutrons (neutral particles) with the matter. Neutrons have zero charge and negligible electric dipole. The key interaction in neutron diffraction experiments is the elastic scattering of neutron particles and nuclei of materials.

The structure factor (F_{hkl}) for neutron diffraction can be expressed as follow:

$$F_{hkl} = \sum_{j=1}^{J} b_j \exp\left(i\boldsymbol{q} \cdot \boldsymbol{r_j}\right) \qquad 2.5$$

where b_j is the neutron scattering length of the atom j, or in the form of that atomic coordinates, similar to the mathematic expression of the structure factor for X-ray diffraction.

$$F_{hkl} = \sum_{j=1}^{J} b_j \exp\left[i2\pi(hx_j + ky_j + lz_j)\right] \qquad 2.6$$

In Zn-IV-N_2 (IV: Ge), the isoelectronic ions (such as Zn^{2+} and Ge^{4+}) have similar atomic form factors (Figure 8), making it difficult to distinguish them from the diffraction signal. As a solution, neutron diffraction is a powerful method to distinguish these isoelectronic ions because of their distinct neutron diffraction length difference.

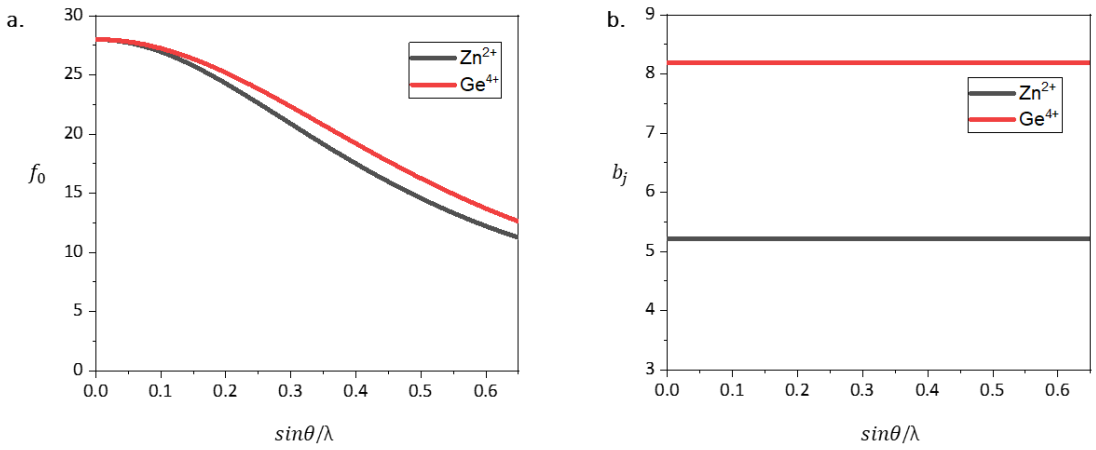

Figure 8 Atomic form factors[91] (a) and neutron scattering length[92] (b) of isoelectronic Zn^{2+} and Ge^{4+}. Parameters for calculation are from the International Tables for Crystallography.[91, 92]

Structure factor is a critical tool in the interpretation of scattering patterns, including XRD patterns and neutron diffraction patterns. This is because the structure factor contains various information concerning the crystal structure and relates to the intensity of the scattered signal. When studying well-crystallised polycrystalline materials such

as crystallised powders, it can be assumed that the probability of each orientation of crystal planes is equal. In this case, the intensity of a Bragg reflection largely depends on the structure factor of phases in the material. Hence, the intensity for a crystalline material can be expressed as:

$$I_{hkl} = I_{electron}|F_{hkl}|^2|L_{hkl}|^2 \quad 2.7$$

where L_{hkl} stands for interference function according to Laue, implying that only the diffraction signals that meet Laue's condition (or Bragg's law) can be detected and displayed in the diffractogram.[90]

For powder or polycrystalline samples, since these samples can be thought of as a random stack of numerous tiny crystals, the diffraction can be regarded as an overlapping of many tiny crystal diffraction signals. Therefore, for an unpolarised incident beam, the intensity of the diffraction signal must be a function of the diffraction angle 2θ and equal in all directions and reach the maximum where Bragg's law is obeyed.

Indeed, the actual diffraction is more complex and requires consideration of the instrument configuration, domain size, preferred orientation, defects, absorption, etc. Nonetheless, these complications are beyond the scope of this section since the main purpose of this section is to provide a comprehensible overview of diffraction principles – this aids in understanding the structure determination of powder diffraction data by whole pattern fitting methods.

2.1.2 Evaluation of diffraction data: whole pattern fitting methods

2.1.2.1 Rietveld method

As mentioned in the section above, the scattered waves by the crystalline material can be expressed as Fourier transformations of the electron density $\rho(\boldsymbol{r})$ of the material. Mathematically, one can obtain the electron density function by inverse Fourier transformation of the scattered wave function. However, what can be measured experimentally is only the scattering intensity (I) that is only related to the absolute value of the amplitude of scattered waves (A) with the relationship of

$$I = |A|^2 \quad 2.8$$

and cannot peek into the phase information of waves. Thus, the exact distribution of electrons cannot be directly deconvoluted from the measurable diffraction signal due to the loss of information.

An implementable strategy is first to assume a structural model with $\rho(\boldsymbol{r})$, obtain the calculated intensity by Fourier transformation and then compare the calculated intensity with the observed one. Afterwards, this structural model is modified until the calculated results match the observed results. This strategy is widely embodied in various fitting methods, including the fitting methods for diffraction patterns.

Hugo Rietveld described in 1967 an analytical method to characterise a powder diffractogram, which is well-known as Rietveld refinement.[93] This method was a critical outbreak for analysing powder diffractogram since it is able to deal with strongly overlapping diffraction signals. The method can be used to analyse crystal structure, unit cell parameters, domain size and shape, microstrain, atomic coordinates, site occupancy factor (SOF), atomic vibration parameters and other important information.

Rietveld refinement fits the whole pattern profile by employing a crystal structure, diffraction optics effects, peak shape function, specimen and instrumental parameters. The calculation of patterns is made that a whole powder diffraction pattern of crystalline material can be thought of as a linear summation of all individual Bragg reflections. The calculated intensity of a diffractogram at the position $2\theta_i$ can be expressed as:[94]

$$I_{ci} = s \sum_{hkl} L_{hkl} |F_{hkl}|^2 \emptyset(2\theta_i - 2\theta_{hkl}) P_{hkl} A + I_B \qquad 2.9$$

where *s* is the scale factor, *hkl* are the Miller indices for Bragg reflections, L_{hkl} is the term containing Lorentz, polarisation and multiplicity factors, $\emptyset(2\theta_i\text{-}2\theta_{hkl})$ is the peak shape function. P_{hkl} is the preferred orientation function, and *A* is the absorption factor. Besides, the method takes into account the background noise of measurable intensity that is expressed as I_B.

The Rietveld refinement utilizes a least-squares approach to fit a line profile until it coordinates with the measured profile. The refinement principle can be demonstrated by the form of the residuum function *M*, which has to be minimized with respect to the refined parameters:[93]

$$M = \sum_i w_i \{y_i(obs) - y_i(calc)\}^2 \qquad 2.10$$

where w_i is the weight factor equal to $1/y_i$, y_i(obs) are the observed intensity and y_i(calc) is the calculated intensity.

Before a refinement, instrument parameters such as the wavelength, polarisation, and instrument configuration are given since they are related to the experimental setup, usually fixed during the calculation. In addition to the instrument parameters, the diffraction profile is governed by the structural model since it determines the simulated $\rho(\boldsymbol{r})$.

The profile calculation can be looked upon as a sequential process following the order of peak position – peak intensity – peak shape – summation of all peaks. This way of thinking facilitates understanding of what information is encoded therein and how the calculated pattern is affected by refined parameters.

Herein, the paragraph mainly discusses the effect of the parameters involved in Rietveld refinement on calculating a profile. First, the position of atoms (described by combining the space group with related unit cell parameter (a, b, c, α, β, γ)) essentially defines interplanar distances, hence the peak position $2\theta_{hkl}$ of Bragg reflections according to Bragg's law. Then, the integral intensity of individual peak is strongly related to the structure factor F_{hkl}, depending on the atomic type (atomic number and the charge), atomic coordination (x, y, z) and site occupancy factor (SOF), as well as thermal vibration of atoms. Further, the peak shape and width can be quantified by using a peak shape function to distribute the integral intensity of a Bragg reflection. It is common to empirically select peak shape functions containing Gaussian and Lorentz components to reflect the peak shape since a realistic ab initio modelling is difficult. Finally, the individual peak functions are summed and added to a background function I_B to achieve the resultant diffraction pattern.

After the initial model has been built, the parameters that need to be refined are set as variables in refinement step by step. Then the variables are involved in the least-squares calculation to fit calculated results with the observed diffraction data.

In the present work, the following parameters are varied in Rietveld refinements:

(a) the instrument-related parameters, including:

the zero-shift parameter for XRD data to correct the error from detector position, the sin(θ)-dependent shift for neutron data to perform the sample transparency

correction, and the asymmetry parameter to correct the axial divergence of beam for all data set;

(b) the overall scale factor;

(c) six-order polynomial function for background;

(d) peak shape parameter according to Thompson-Cox-Hastings pseudo-Voigt function to calculate the amount of Gaussian and Lorentzian peak broadening;[95]

(e) spherical harmonics in the Laue class *mmm* for anisotropic line broadening correction;[96, 97]

(d) the parameters related to the crystal structural model, such as lattice constants, atomic positions, atomic displacement parameters and site occupancy factor.

It should be noted that the site occupancy factors (SOF) are fixed for refining XRD patterns of Zn-Ge-O-N samples since the isoelectronic cations (Zn^{2+} and Ge^{4+}) are difficult to be distinguished. For example, when using an orthorhombic structural model, SOF is set to 1 for each cation site for a β-$NaFeO_2$-type sample to reflect the expectation of fully ordered cations. Similarly, SOF is set to 0.5 Zn and 0.5 Ge for each cation for a wurtzite-type sample to reflect the fully disordered arrangement of cations. Fixing the SOF is a must strategy to allow a convergence of refinement in this case; otherwise, the SOF would jump in a wide range due to the similar atomic form factor of Zn^{2+} and Ge^{4+}, leading to refinement failure.

2.1.2.2 Le Bail method

Le Bail method was first applied in 1988 to refine the unit-cell parameters and extract Bragg peak integral intensity best estimations without requiring the atomic information.[98]

This approach set arbitrary integrated intensity for reflections I_K(obs) in the initial step by giving an initial value of S_i^2 to yield the I_K(obs), which will be used as the new value of S_K^2 in the next iteration. The $w_{i,K}$ is a measure of the contribution of the Bragg peak at position $2\theta_K$ to the diffraction profile y_i at position $2\theta_i$.

$$I_K(obs) = \sum_j \{w_{i,K} \cdot S_K^2 \cdot y_i(obs)/y_i(calc)\} \quad 2.11$$

The simplified iterative process provides a quick way to extract information, including the unit-cell parameters, shift due to the instrumental setting, peak width parameters, and peak shape parameters. At present, the Le Bail method is commonly embedded in most Rietveld refinement software, such as FULLPROF[99] and Jana[100]. The Le Bail refinement can be used as a reference for building accurate Rietveld refinement starting models or as a stand-alone means of analysing the unit cell of phases.

In the present work, the Le Bail method was applied for the XRD patterns involving reflections of the LaB_6 standard to access fast determination of lattice constants through multi-phase refinement. The following parameters are applied:

(a) the instrument-related parameters, including:

the zero-shift parameter to correct the error from the detector position, and the asymmetry parameter to correct the axial divergence of the beam;

(b) linear interplation function for background;

(c) peak shape parameter according to a Thompson–Cox–Hastings pseudo-Voigt function to calculate the amount of Gaussian and Lorentzian peak broadening;[95]

(d) spherical harmonics in the Laue class *mmm* for anisotropic line broadening correction;[96, 97]

(e) lattice constants for determining the position of Bragg reflections. Applying the Le Bail method does not need to consider the overall scale factor and atomic details.

2.1.3 Instruments of diffraction experiments

2.1.3.1 Laboratory Powder X-ray Diffraction (PXRD)

The laboratory PXRD experiments were carried out in the X-ray CoreLab at Helmholtz Zentrum Berlin (HZB). PXRD data were collected using a Bruker D8 Advance powder diffractometer in Bragg-Brentano geometry in a 2θ range from 15° to 140° for flat plate samples. The radiation source is Cu-$K_{\alpha1}$ (λ = 1.540559 Å) and Cu-$K_{\alpha2}$ (λ = 1.544426 Å) radiation with an intensity ratio $I_{K\alpha1}/ I_{K\alpha2}$ of 0.497.

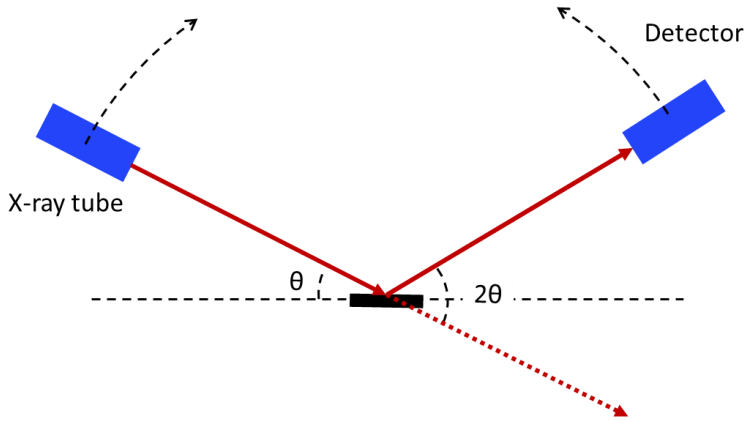

Figure 9 Schematic illustration of the Bragg-Brentano geometry.

2.1.3.2 Neutron diffraction

Neutron diffraction is a powerful tool to distinguish isoelectronic ions with similar atomic form factors, as discussed in section 2.1.1 (Figure 8). For this, the thesis uses neutron diffraction to investigate the cation disorder in Zn-Ge-O-N compounds. The neutron diffraction data were collected by E9 instrument at Helmholtz-Zentrum Berlin für Materialien und Energie (HZB)[101] and D2B instrument at Institut Laue-Langevin (ILL)[102].

2.2 Elemental analyses

Elemental analysis methods provide information on the elemental ratio in compounds, allowing the calculation of chemical composition. It is important to study the chemical composition of the compounds. For example, knowing the chemical composition at different reaction stages is essential for investigating the reaction mechanism, facilitating optimising the synthesis method in order to gain phase-pure samples. Additionally, for structure determinations, knowing the chemical composition allows applying supplementary constraints into Rietveld refinement to stabilise the calculation of atomic details such as the site occupancy factor. This work has applied three different elemental analysis methods, including X-ray fluorescence spectroscopy, carrier gas hot extraction, and energy dispersive X-ray spectroscopy, to characterise the chemical composition of the compounds.

2.2.1 X-ray fluorescence spectroscopy (XRF)

X-ray fluorescence refers to the emission of characteristic "secondary" X-rays from materials excited by high-energy X-rays. When high energy X-rays encounter the material, the tightly held electrons of the inner shell of the atoms may be excited to higher energy orbitals, such as the outer shell, or be ionised, such as ejection of electrons.[103] Removing electrons from the inner shell results in an energetically unstable electron structure, so electrons from the outer shell move into the inner shell to fill the hole – the vacancy left behind by the electron ejection. Because electrons from the outer shell have higher energy than those from the inner shell, the atom radiates energy outward in the form of X-rays. The wavelengths of these "secondary" X-rays are related to the shell types and atom types.[104] Therefore, one can qualitatively analyse the elements by the wavelength of these secondary rays and quantitatively investigate the elemental proportions by the intensity of the signal.

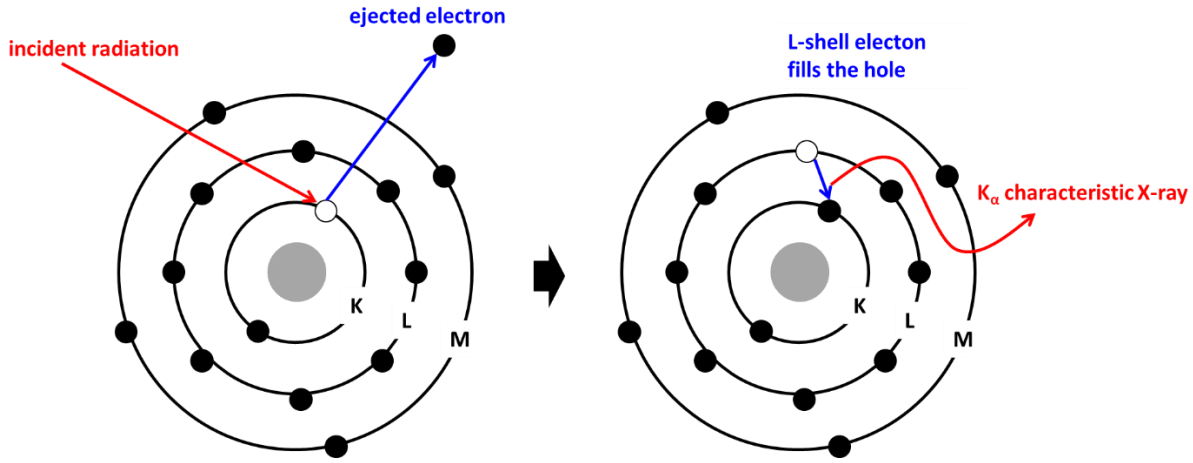

Figure 10 Schematic illustration of emission of characteristic X-ray.

In this work, X-ray fluorescence spectra (XRF) were collected using a Bruker M4 Tornado system with Rh-Microfocus tube for the determination of the cation ratios. The tube voltage was set to 50 kV. Samples were pressed to pellets with 5 mm in diameter to avoid contamination when measuring in vacuum. Further, the pellets offer a flat surface for focusing in order to eliminate an undesired background. For each pellet, data on 6 different measuring points, at least, were collected with a collection time of 60 s per point.

It should be noted that XRF is reliable for cation analysis (Zn, Ge, Sn) in this work, while it is not able to measure the anions (O and N) since the energy of the characteristic X-ray of O and N are too low to pass through the detector window to be counted.

2.2.2 Hot gas extraction (HE)

O and N determination for materials in this work requires specialised laboratory methods such as Hot gas extraction (HE). Hot gas extraction is a method for non-metal elements analysis such as H, C, N, O, S in inorganic materials. The gases that are emitted during overheating, melting, or decomposition are extracted and analysed by gas chromatography or other characterisation methods.

In this work, the experimentation of HE is performed by Dr. Stefan Berendts at Technische Universität Berlin (TU Berlin). The measurement was carried out by using a LECO TC-300/EF-300 instrument to determine O and N contents. Samples of approximately 10 mg were used for each independent measurement. The average value of three repeated measurements was taken as the final data with a relative error of 2 %.

2.3 Ultraviolet-visible spectroscopy (UV-Vis)

An ultraviolet-visible spectrum refers to the absorption spectrum when electromagnetic waves in the visible and adjacent ranges irradiate the material. In this spectrum region, the incident light can excite the electrons from their ground state to an excited state and provoke changes in the electronic structure of materials. For example, for semiconducting materials, the incident light can trigger the electronic excitement from the valence band to the conduction band. Therefore, the absorption spectrum of semiconductors involves significant information of the optical bandgap energy. Thus, one can apply the UV-Vis method to estimate the optical bandgap of semiconductors, which is crucial in predicting photovoltaic properties.

The Tauc method[105] is widely used to evaluate the UV-Vis spectrum to estimate the optical bandgap of crystalline semiconductors based on absorption spectrum and was further developed by Davis and Mott.[106, 107] The energy-dependent absorption coefficient of a material can be expressed by:

$$(\alpha h\nu)^{1/n} = B\left(h\nu - E_g\right) \qquad 2.12$$

where α is the absorption coefficient, h is the Plank constant, v is the frequency of light, E_g is the bandgap value, B is a constant. The factor n in the exponent donates the nature of the transition. For direct allowed transition, n is equal to 1/2, and for indirect allowed transition, n equals 2.[108]

For thin-film samples, the absorption coefficient can be calculated by combining the absorbance with the thickness of the specimens. However, it is challenging to calculate the absorption coefficient of powders using absorbance and thickness since complex refraction and unclear thickness of specimen due to random stacking of irregular particles.

Applying the Kubelka-Munk function[109] permits transforming reflectance spectra into corresponding absorption spectra, thus overcoming the challenge of measuring the absorbance and thickness of the powder specimens. Applying the Kubelka-Munk (or F(R)) method for reflectance offers great advantages to determine the bandgap since F(R) is proportional to the extinction coefficient, hence reflecting the absorption nature of the material.[110-112] The combining of the Kubelka-Munk function with the Tauc method can be expressed as:

$$[F(R_\infty)hv]^{1/n} = B\left(hv - E_g\right) \qquad 2.13$$

where $F(R_\infty)$ is the Kubelka-Munk function, can be expressed by:

$$F(R_\infty) = \frac{K}{S} = \frac{(1-R_\infty)^2}{2R_\infty} \qquad 2.14$$

K and S are the absorption and scattering coefficients, respectively. $R_\infty = R_{\text{Sample}}/R_{\text{Standard}}$ is the relative reflectance of a powder sample of infinite. Additionally, exploration of the Kubelka-Munk function was used as a stand-alone method to estimate the optical bandgap without considering the type of transition.[110]

The present work uses a PerkinElmer Lambda750S spectrometer with a diffuse reflectance sample holder suitable for powder specimens. The instrument scans through the wavelength range (1500 nm - 300 nm) with a step size of 2 nm. Ulbricht sphere and praying mantis setup were used to collect the light reflected diffusely from the sample.

Chapter III

Study of zinc germanium oxide nitride

In this chapter, oxide nitride compounds are used as the exemplary system to investigate phase relations in Zn-IV-nitrides since the oxygen impurities are challenging to avoid entirely in prepared products. This chapter begins with the preparation of Zn-Ge-O-N powders through the nitridation of Zn_2GeO_4. Then a two-step reaction mechanism is elucidated based on the elemental analysis of compounds at different reaction stages. Understanding and verifying the reaction mechanism facilitates optimisation of the synthesis method and investigation of the cation disordered effect in the crystal structure. Next, using X-ray diffraction, an evident structural transformation between wurtzite-type and β-$NaFeO_2$-type is experimentally observed, followed by a discussion on the crystal structure of compounds, particularly at different transformation stages.

Further, together with the neutron diffraction technique, the experimental investigation of cation disorder is achieved. This section distinguishes the intrinsic and extrinsic cation disorder by analysing the site occupancy (SOF) and determines the significant effects of cation disorder on the crystal structure. Finally, combining chemical and structural analysis with the optical bandgap value measure by UV-Vis, the bandgap tunning phenomenon of this material system is revealed.

3.1 Synthesis of phase pure $ZnGeN_2$ powder

In this work, oxygen-containing $ZnGeN_2$ were prepared using the ammonolysis reaction of oxide precursor, as outlined in literature.[39, 46, 113] Because of oxygen impurity in the material, the following section names the compounds as Zn-Ge-O-N. The synthesis process was optimised to reduce the oxygen content in Zn-Ge-O-N to achieve an approximant toward pure nitride. The following subsections discuss the preparation method of oxide precursors and Zn-Ge-O-N powders.

3.1.1 Preparation of Zn_2GeO_4 powder as the precursor

Figure 11 shows the preparation process of the Zn_2GeO_4 precursor. A mixture of ZnO (Fisher Chemical, laboratory reagent grade, > 99 %) and GeO_2 (ACROS Organics, electronic grade, 99.999 %) with a molar ratio of 2:1 was prepared by grinding. The mixture was pressed into pellets of 10 mm diameter using hydraulic equipment and a pressing die and then annealed at 1100 °C for 72 hours in a muffle furnace. The heating rate was 200 K/h. Pressing the ZnO-GeO_2 mixture into pellets reduces the porosity of the mixture, increasing the contact area between the powder particles, thus facilitating the diffusion of substances in the solid-state reaction. After annealing, the samples are cooled naturally to room temperature in the oven.

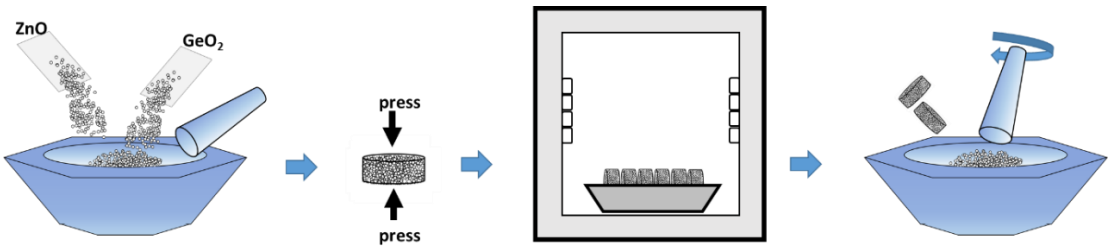

Figure 11 schematic illustration of preparation process of Zn_2GeO_4 precursor.

One obtained white solid pellets as products, which was reground into powders to adapt following characterisation processes. The annealed pellets were significantly harder than the pressed blocks of the powder mixture. This is rational because of the substance diffusion between precursor particles during the annealing.

Figure 12 shows the refinement of the XRD pattern of Zn_2GeO_4. The Bragg reflections in the experimental pattern are sharp, suggesting that the powder was well-crystallised. The red circles are the measured pattern. The trace of ZnO phases was observed in the measured pattern. The three strongest reflections of ZnO are highlighted with asterisk symbols. Therefore, a two-phase Rietveld refinement (Zn_2GeO_4 and ZnO phases) was performed for the XRD pattern of Zn_2GeO_4 prepared in this work. The black line is the calculated pattern using the unit cell setting reported by Oribe et al.[114] as starting parameters. The green ticks represent the reflection position of the phases (Zn_2GeO_4 top and ZnO bottom). The profile in the experiment pattern is consistent with that in the calculated one with χ^2 = 5.62 and $R_{Bragg}(Zn_2GeO_4)$ = 5.96, indicating acceptable goodness of fit.

According to the refinement, the main phase is Zn_2GeO_4, which has a weight fraction of 98(7)% and the Zn/Ge ratio of approximately 2.05(6):1, largely the ratio of stoichiometry Zn_2GeO_4. In addition, 1.52(14) wt.% of ZnO is present in the product. This slight amount of ZnO in the Zn_2GeO_4 precursor is negligible because the next step applies ammonolysis reaction of the precursor at over 800 °C, ZnO converts into Zn_3N_2[115] and subsequently decomposes to gaseous Zn vapour and N_2,[116, 117] which does not remain in the final product. Thus, the Zn_2GeO_4 prepared by this method can be used as a precursor for the next step in synthesising Zn-Ge-O-N compounds.

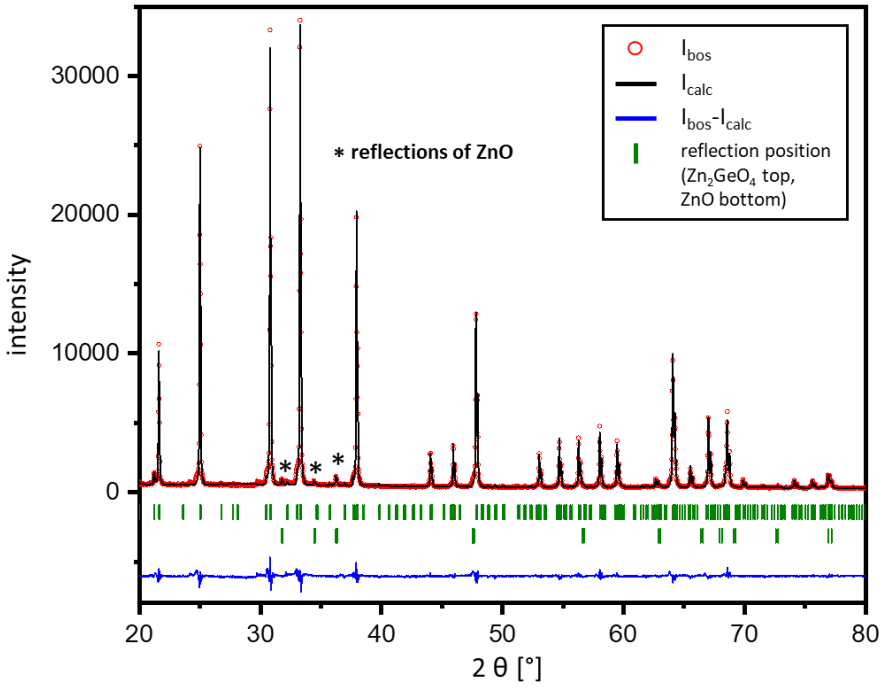

Figure 12 Plot of Rietveld refinement of XRD profile of Zn_2GeO_4 powder: measured intensity I_{obs} (red circlues), calculated intensity I_{calc} (black line), difference I_{obs} - I_{calc} (blue line) and calculated reflection positions (green ticks, Zn_2GeO_4 top, ZnO bottom). Three evident reflections of ZnO are marked by asterisk symbols.

3.1.2 Preparation of Zn-Ge-O-N compounds towards $ZnGeN_2$

3.1.2.1 Experimental setup

The ammonolysis reaction of Zn_2GeO_4 precursors was carried out in a silica glass reaction tube with 4.5 cm diameter. The oxide powder was first contained in a ceramic boat and treated under a N_2-flux of 1.5 l/min during the heating until the reaction temperature (*T*) is reached. The heating rate was 250 K/h. The reaction temperature was in the range between *T* = 835 °C to *T* = 910 °C. A NH_3-flux of 0.05 l/min - 0.3 l/min (99.8 %, AirLiquide) was applied once the reaction temperature is reached. The samples were then reacted with ammonia during the dwelling period (*t*) varied between 1 h and 27 h to produce samples with varying oxygen content.

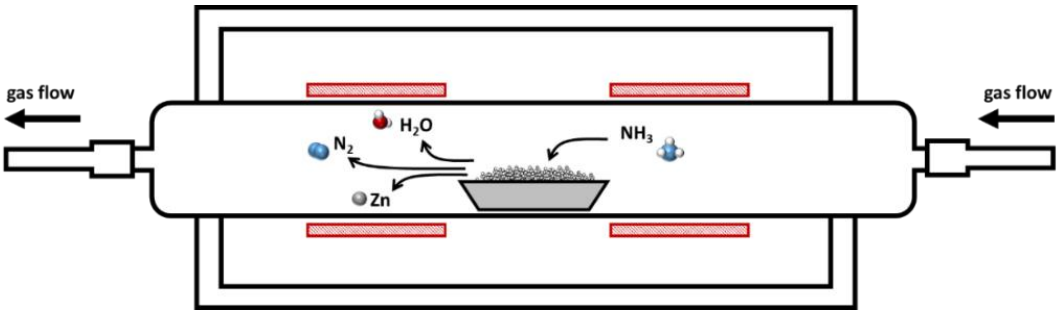

Figure 13 Schematic illustration of nitridation process of Zn_2GeO_4 precursor.

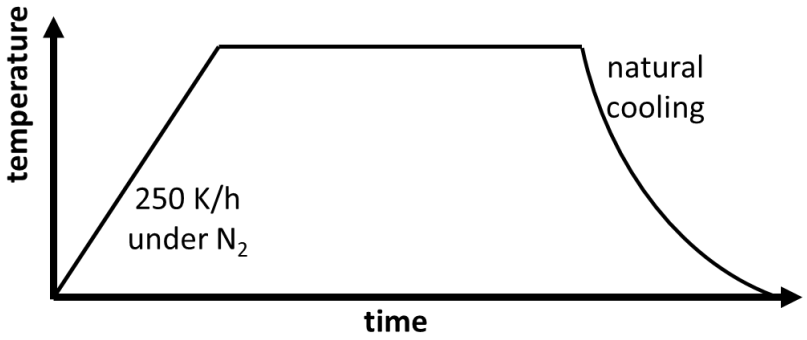

Figure 14 Schematic illustration of reaction temperature (*T*) during synthesis.

3.1.2.2 Reaction conditions and stability limit

Figure 15 illustrates the reaction conditions of all samples, including the reaction temperature *T* and dwelling time *t*. The phase-pure (one phase) and multi-phase samples (containing side phase) are plotted as solid circles and hollow circles, respectively. Therefore, we propose an empirical curve to distinguish between the phase-pure and multi-phase regions, as shown in the dotted line in Figure 15. This empirical curve represents the stability limit of the compounds during such a synthesis process. Synthesis conditions over the stability limit (temperature or dwelling time over the curve) lead to the decomposition of the oxide nitride. The decomposition product can be Ge or Ge_3N_4.

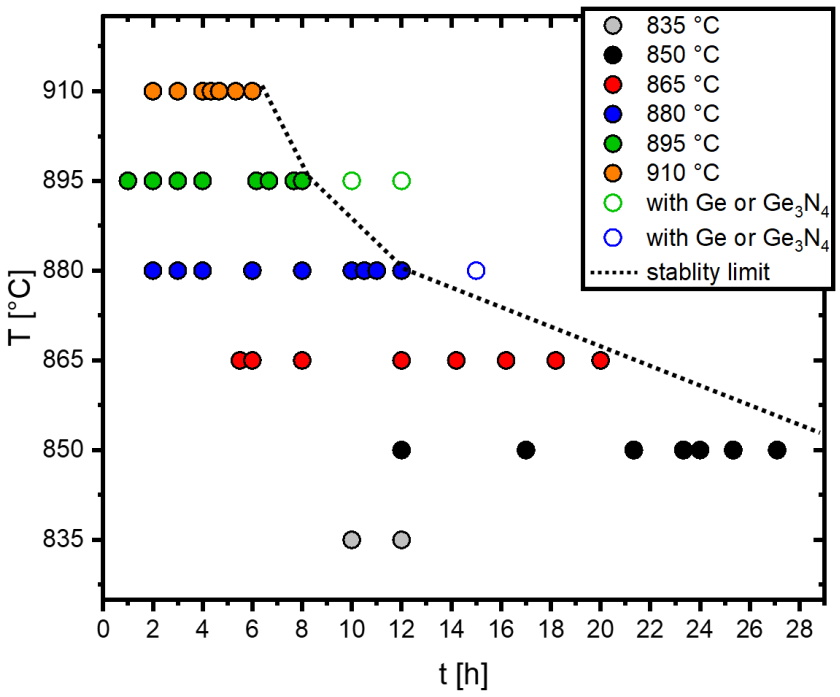

Figure 15 Plots of synthesis conditions (dwelling time *t*, reaction temperature *T*) of phase-pure Zn-Ge-O-N compounds (solid circles) and multi-phase samples containing Ge or Ge_3N_4 side phases (hollow circles). The proposed stability limits is expressed by a dotted line.

The powder samples at different stages of the reaction show different colours. Using low temperature or short dwelling time, one obtains light-yellow samples with a crystal structure in the wurtzite-type (Figure 16a). Increasing the reaction temperature or dwelling time gradually turns the colour of samples from light yellow to rose grey (Figure 16b insert). For example, when the combination of reaction temperature and

dwelling time approached the reaction conditions indicated by the dashed lines in Figure 15, the samples faded completely from light yellow and took on a rose-grey colour.

These rose grey samples crystallise in the β-$NaFeO_2$-type structure, confirmed by XRD (Figure 16b). Continuing to increase the reaction temperature or dwelling time beyond the reaction conditions represented by the dotted line in Figure 15, the samples obtained are in coffee grey (Figure 16c). The XRD pattern exposes that significant amounts of Ge or Ge_3N_4 side phases are present in the sample in addition to the β-$NaFeO_2$-type main phase.

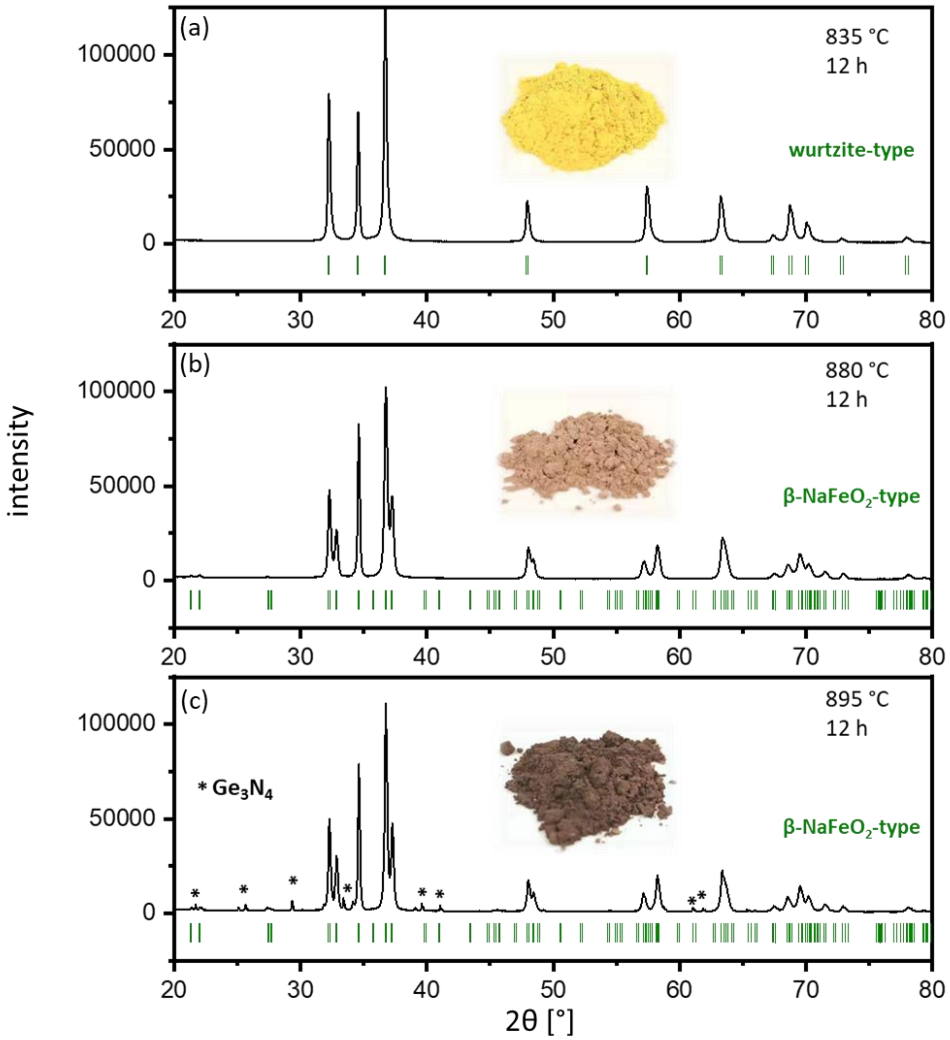

Figure 16 XRD patterns of samples prepared by conditions 835 °C – 12 h (a), 880 °C – 12 h (b), 895 °C – 12 h (c), together with Bragg position of the wurtzite-type structure (a) and the β-$NaFeO_2$-type structure (b) (c) shown as green lines. Optical photos of samples are shown as inserted images.

3.1.2.3 Effect of NH_3-flux in cooling

To facilitate the experimental investigation of crystal structure transformation of Zn-Ge-O-N, one desires 1) having Zn-Ge-O-N samples in the wurtzite-type structure and samples in the β-$NaFeO_2$-type; 2) these samples should be phase-pure.

First, the synthesis of specimens is the preparative basis of experimental characterisations. Second, the concern about the purity of the phase is rationale because phase-pure samples facilitate characterisation, such as chemical analysis (i.e. XRF, HE). For the chemical analysis of powder samples, where phases are mixed homogenously, collecting the signal from one phase from a multi-phase powder is challenging for the two methods we use in this work. Having multi-phase samples with a large fraction of side phases increases the complexity of the data evaluation, thus reducing characterisation accuracy.

In addition, the phase-pure sample simplifies the model of crystal structures involved in the refinement; for a phase-pure sample, a single-phase model can be used. This reduces the number of variables involved in the refinement and reduces the computational time consumption. For another, it avoids the computational errors caused by the cross-correction of the computational intensities of the different phases and increases the accuracy of the computational results.

The challenge of obtaining phase-pure Zn-Ge-O-N lies in the paradoxes between increasing the reaction temperature and time to obtain the β-$NaFeO_2$-type phase and the decomposition of products. The key of synthesis is to prevent the sample from decomposition at that condition combination of *T* and *t* required for β-$NaFeO_2$-type Zn-Ge-O-N. Therefore, the reaction process should be carried out under a protective atmosphere such as N_2 or the reaction atmosphere such as NH_3 until samples cool down to room temperature in order to avoid decomposition or oxidation of Zn-Ge-O-N.

N_2 is widely used as a protective atmosphere for the synthesis of nitrides since nitrogen is chemically stable and does not react with the products. However, Ge traces are present in the samples prepared at 880 °C - 10 h if one applies the N_2-flux as the cooling atmosphere (Figure 17a). The sample begins to decompose before it has reached the reaction stage of crystallisation into a β-$NaFeO_2$-type structure. Interestingly, when cooling the sample prepared by the same *T* and *t* combination under NH_3-flux of 0.15 l/min, one obtains a phase-pure sample without Ge trace (Figure 17b). Continuing to

increase the dwelling time to 12 hours allows obtaining phase-pure β-$NaFeO_2$-type Zn-Ge-O-N (Figure 17c).

The better stability of Zn-Ge-O-N under ammonia than under nitrogen is probably related to the chemical potential of the μ(N). The use of NH_3 can result in a higher effective chemical potential μ(N),[118] reducing the driving force of decomposition.

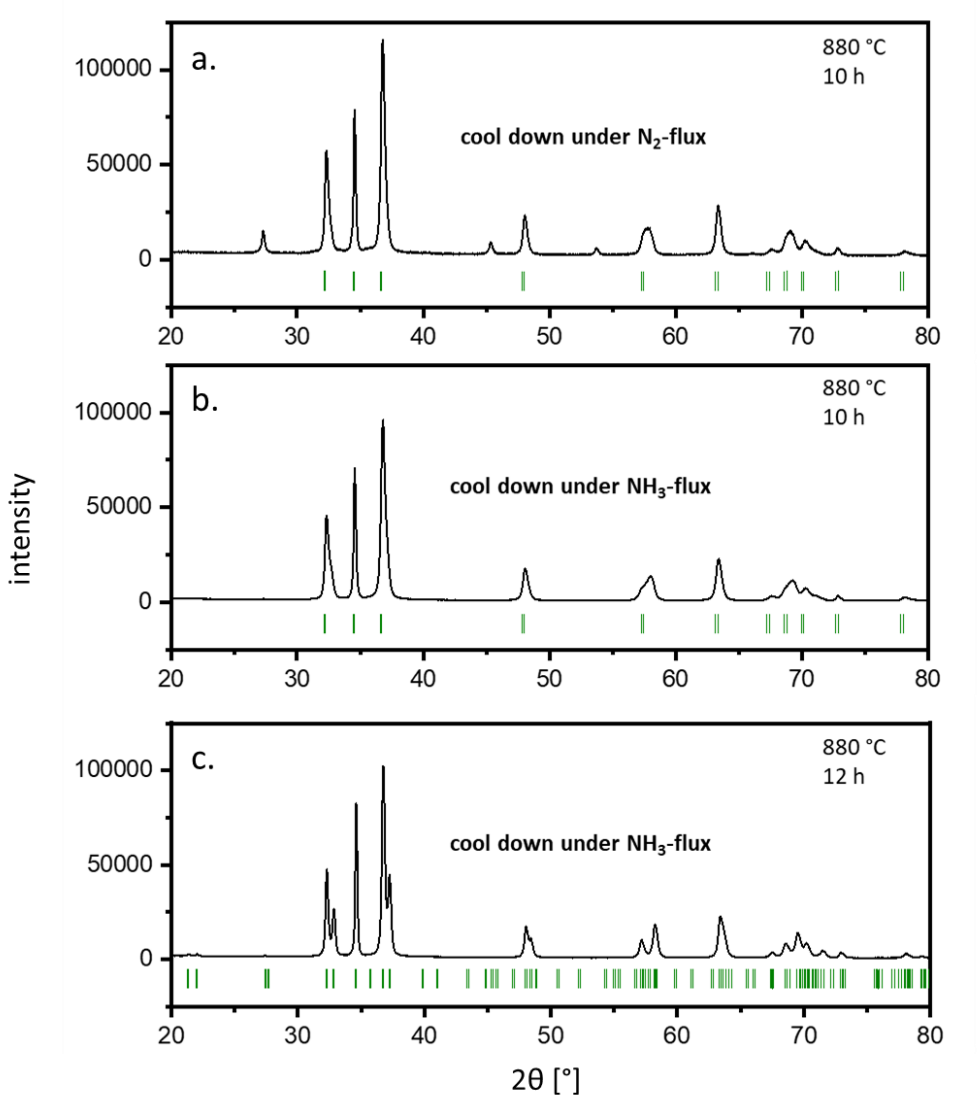

Figure 17 XRD patterns of samples prepared by conditions 880 °C – 10 h (a), 880 °C – 10 h (b), 880 °C – 12 h (c) with the cooling atmosphere of NH_3-flux or N_2-flux, together with Bragg position of the wurtzite-type structure (a) (b) and β-$NaFeO_2$-type structure (c) shown as green lines.

3.2 Elucidation of the reaction mechanism for the synthesis of $ZnGeN_2$ through Zn_2GeO_4 ammonolysis

The Zn-Ge-O-N samples are prepared by using the ammonolysis reaction of Zn_2GeO_4. The reaction mechanism was first discussed by Bacher et al..[119] They proposed that this reaction can be formulated in two subreactions:

$$Zn_2GeO_4 + 2v\,NH_3 \rightarrow Zn_2GeO_{4-3v}N_{2v} + 3v\,H_2O \quad 3.1$$

$$Zn_2GeO_4 + \frac{2u}{3}NH_3 \rightarrow Zn_{2-u}GeO_{4-u} + \frac{u}{3}\,Zn_3N_2 + u\,H_2O \quad 3.2$$

$$Zn_2GeO_4 + (\frac{2u}{3}+2v)\,NH_3 \rightarrow Zn_{2-u}GeO_{4-u-3v}N_{2v} + \frac{u}{3}\,Zn_3N_2 + (u+3v)\,H_2O \quad 3.3$$

Both subreactions are assumed to start with Zn_2GeO_4 precursor as initial reactants but follow different reaction paths. The subreaction represented by Formula 3.1 is governed by the replacement of oxygen by nitrogen. This subreaction is named as substitution of oxygen by Bacher,[119] here expressed as "O-substitution". Formula 3.2 shows the extraction of zinc and oxygen; according to Bacher, this reaction represents the displacement of zinc,[119] here named as "Zn-extraction".

The coefficients in these two formulas are expressed in terms of *v* (Formula 3.1) and *u* (Formula 3.2), respectively, to describe the consumption of ammonia and the change in chemical composition.

This section discusses the chemical composition of Zn-Ge-O-N, which was measured by combining chemical analyses (XRF and HE), and followed by a discussion on the reaction mechanism to understand the chemical composition evolution from oxide nitride towards pure nitride. The study of the reaction mechanism explores the sequence of both subreactions in the reaction. Clarifying the reaction pathway aids in understanding the structural and electronic features of this class of compounds

3.2.1 Chemical composition of the samples

The chemical composition of the samples can be calculated by determining the elemental ratio of the four elements. However, it is not easily accessible to measure the reliable elemental ratio over the four elements in Zn-Ge-O-N.

Instead of taking straightforward measurements of the four elemental ratios, Zn, Ge content and O, N content were separately measured using the XRF (Section 2.2.1) and HE (Section 2.2.2), respectively. The results output by instruments can be a weight content. The Zn/Ge and O/N ratios can be calculated from the measured results. These elemental ratios are atomic ratios, which facilitate calculating chemical composition. A simple conversion into atomic ratio can be made by introducing the molar mass of elements. The conversion formula is shown as

$$\frac{n(\mathrm{O})}{n(\mathrm{N})} = \frac{w(\mathrm{O})M(\mathrm{N})}{w(\mathrm{N})M(\mathrm{O})} \qquad 3.4$$

where n(O) and n(N) represent the molar fraction of O and N, w(O) and w(O) are the weight fraction in the sample. M(O) and M(N) are the molar mass of O and N, respectively.

Sequencently, with the Zn/Ge and O/N atomic ratio, one can calculate u and v by solving the formula set (Formula 3.5, Formula 3.6) based on the general formula $Zn_{2-u}GeO_{4-u-3v}N_{2v}$ (Formula 3.3). After that, the overall chemical composition is yielded by introducing v and u in the formula $Zn_{2-u}GeO_{4-u-3v}N_{2v}$. The calculated chemical composition of the Zn-Ge-O-N compounds in the form $Zn_{2-u}GeO_{4-u-3v}N_{2v}$ is listed in Table 1.

$$\frac{\mathrm{Zn}}{\mathrm{Ge}} = \frac{2-u}{1} \qquad 3.5$$

$$\frac{\mathrm{O}}{\mathrm{N}} = \frac{4-u-3v}{2v} \qquad 3.6$$

A clear trend between the experimental Zn/Ge ratio against the experimental O/N ratio is evident throughout the samples (Figure 18). The Zn/Ge ratio varies between 1 and 2, corresponding to the Zn/Ge ratio of the targeted product $ZnGeN_2$ (Zn/Ge = 1) and oxide precursor Zn_2GeO_4 (Zn/Ge = 2). The O/N ratio is in a range between 0 to c.a. 0.4. It is reasonable for samples with Zn/Ge $\approx$ 1, O/N $\approx$ 0 since the composition approximates towards $ZnGeN_2$. Interestingly, the Zn-richest sample with Zn/Ge $\approx$ 2 shows O/N $\approx$ 0.35 and contains significant nitrogen in compounds. As the Zn/Ge $\approx$ 2 is largely in line with the Zn/Ge in precursor Zn_2GeO_4, one assumes that this compound is in an early stage of reaction. This finding is in line with the previous study on Zn-Ge-O-N reported by Breternitz et al..[120]

Table 1 Experimentally determined Zn/Ge ratios and O/N ratios of the samples in this study together with the compositions as calculated from the formula $Zn_{2-u}GeO_{4-u-3v}N_{2v}$. Full synthesis conditions may be found in the Supporting Information (Table S1).

Sample Number	Zn/Ge ratio	O/N ratio	Nominal composition in formula $Zn_{2-u}GeO_{4-u-3v}N_{2y}$
1	1.91(7)	0.36(1)	$Zn_{1.91}GeO_{0.75}N_{2.10}$
2	1.28(8)	0.089(4)	$Zn_{1.28}GeO_{0.18}N_{2.07}$
3	1.13(1)	0.043(1)	$Zn_{1.13}GeO_{0.09}N_{2.03}$
4	1.12(7)	0.017(1)	$Zn_{1.12}GeO_{0.03}N_{2.05}$
5	1.09(6)	0.016(1)	$Zn_{1.09}GeO_{0.03}N_{2.04}$
6	1.06(1)	0.015(1)	$Zn_{1.06}GeO_{0.03}N_{2.02}$
7	1.06(5)	0.011(1)	$Zn_{1.06}GeO_{0.02}N_{2.03}$

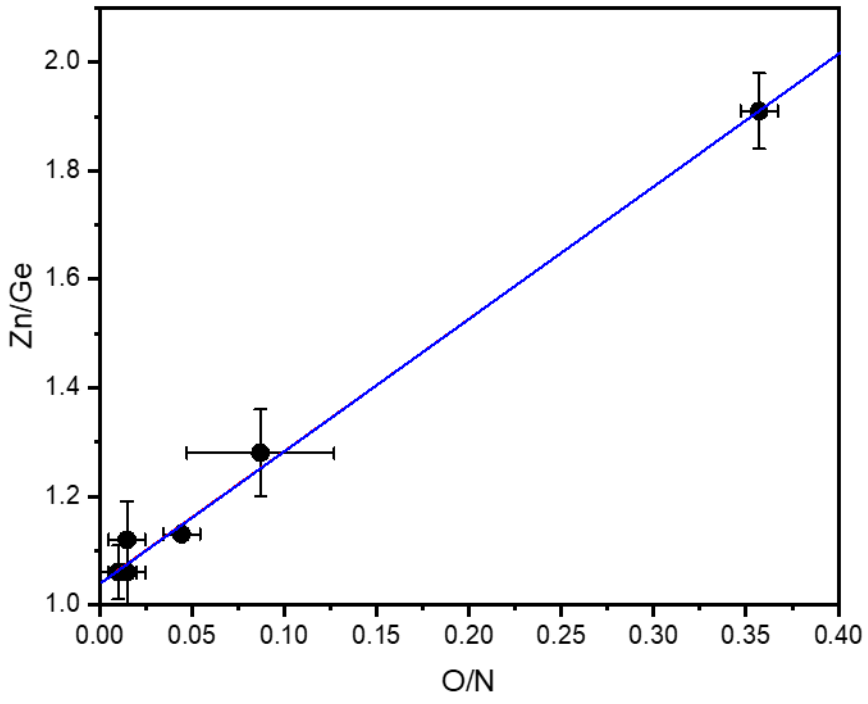

Figure 18 Experimentally determined Zn/Ge ratios against the experimentally determined O/N ratios. The blue line shows a linear fit of the data points with f(x) = 2.47(1)x + 1.02(1). Due to experimental equipment limitations of the carrier gas hot extraction method, a fraction of samples were measured.

3.2.2 Elucidation of the reaction mechanism

As mentioned at the beginning of this section 3.2, the reaction can be split into two subreactions 1) O-substitution, represented by the index *v*, and 2) Zn-extraction, represented by *u*. In the last section 3.2.1, the chemical composition of the compounds has been calculated by combining the formula $Zn_{2-u}GeO_{4-u-3v}N_{2v}$. Herein, the index *v* and *u* represent the contribution of these subreactions to the overall composition. Both subreactions act together on the chemical composition.

Therefore, the value of *v* and *u* contain the information on how the two subreactions affect the chemical composition of $Zn_{2-u}GeO_{4-u-3v}N_{2v}$. Furthermore, combining *v* and *u* with the reaction conditions allows us to investigate the role of these subreactions at different reaction stages. This is essential for understanding the reaction mechanism and developing a synthesis method to give targeted access to the designed chemical composition.

According to the last section, by knowing *v* and *u*, one can calculate the *u*/*v* ratio. The *u*/*v* ratio was defined as an indicator for the relative contribution of both subreactions. When plotting the *u*/*v* ratio with the Zn/Ge ratio, one obtains a clear linear trend with a general formula of linear fit:

$$\frac{u}{v} = 1.98(1) - 0.99(1)\frac{Zn}{Ge} \qquad 3.7$$

According to the formula $Zn_{2-u}GeO_{4-u-3v}N_{2v}$, the relationship between Zn/Ge ratio and index *u* is known as Formula 3.5. Thus, the linear fit formula can be expressed as:

$$\frac{u}{v} = 1.98(1) - 0.99(1) \times (2 - u) \qquad 3.8$$

By combining similar terms and omitting the calculation errors, the formula can be simplified to:

$$v = 0.99 \qquad 3.9$$

It is clear that $v \approx 1$ over the whole composition range of $Zn_{2-u}GeO_{4-u-3v}N_{2v}$ in this study. The variation in *u*/*v* ratio with Zn/Ge is mainly attributed to the variation in *u*. Throughout the reaction, *v* should vary in a range of 0 to 1 with reaction time. As no interval of variation in *v* was observed in this study, the samples analysed here were clearly in the later stage of the reaction where the variation of *v* is completed. In other

words, the variation of the chemical composition of $Zn_{2-u}GeO_{4-u-3v}N_{2v}$ is dominated by the subreaction Zn-extraction (represented by *u*). Furthermore, the O-substitution (represented by *v*) was completed in an early stage, before Zn-extraction. There is an evident sequence between them.

Thus, the general chemical formula $Zn_{2-u}GeO_{4-u-3v}N_{2v}$ can be simplified into $Zn_{2-u}GeO_{1-u}N_2$ by introducing $v = 1$. In this case, the chemical composition in the form $Zn_{2-u}GeO_{1-u}N_2$ can be calculated by having a value of *u*, which is related to the Zn/Ge ratio. Therefore, the chemical composition of a compound can be deduced by knowing only the cation ratio (using XRF only), thus simplifying the procedure for determining the chemical composition. One can use this simplified formula $Zn_{2-u}GeO_{1-u}N_2$ as a convenient approximation to the accurate chemical composition.

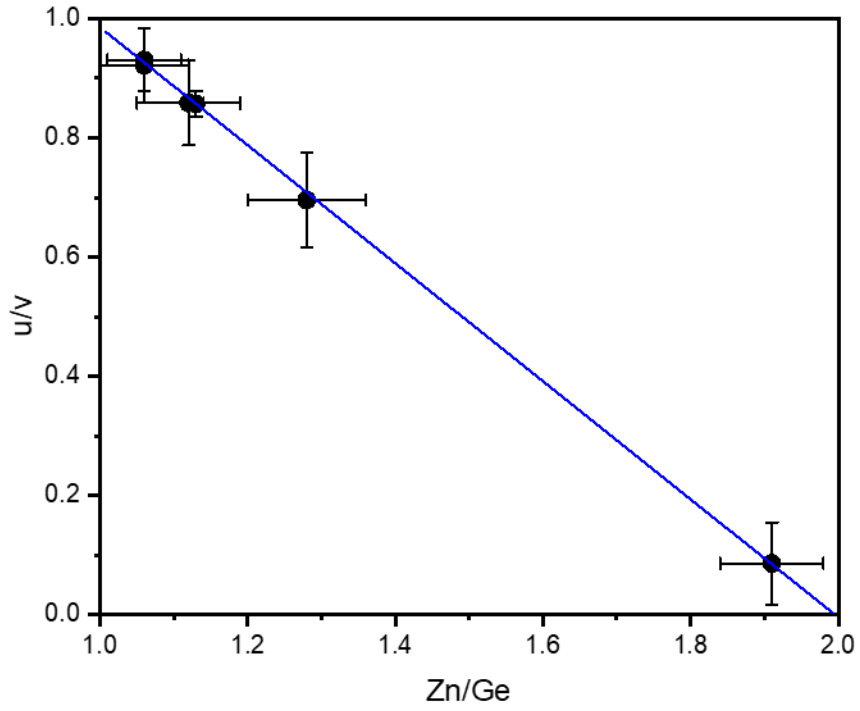

Figure 19 *u*/*v* ratio as a function of the Zn/Ge ratio throughout the composition range. The blue line depicts a linear fit of the data.

Breternitz et al. documented a study of oxygen-richer regimes of Zn-Ge-O-N, including the composition of Zn/Ge > 2.[120] While partial Zn-Ge-O-N compounds reported shows a large Zn/Ge ratio than the Zn_2GeO_4 precursor, most samples follow the same schema. This high Zn/Ge ratio is probably due to a slight loss of Ge in the earlier stage, before

the Zn-extraction. Therefore, it should be noted that the model is limited to the later stages of reaction predominated by the Zn-extraction. For compounds close to $ZnGeN_2$, which are in the later stages of the reaction, the model can be used to assist in chemical composition analysis. Therefore, it is important to understand the reaction mechanism of this reaction period to expose the material properties further.

3.2.3 Verification and implications of the reaction model

From a pure formula point of view, a change in *u* only synchronously changes the indicates of Zn and O in $Zn_{2-u}GeO_{1-u}N_2$. When $u = 0$, the formula is Zn_2GeON_2; when u = 1, the formula is $ZnGeN_2$. Therefore, the formula $Zn_{2-u}GeO_{1-u}N_2$ can be seen as a linear combination of the form:

$$k\ \mathrm{ZnGeN_2} + (1-k)\mathrm{ZnO} \tag{3.10}$$

The relationship between *k* and *u* can be determined by pure mathematical relations:

$$\frac{Zn}{Ge} = 2 - u = \frac{1}{k} \tag{3.11}$$

with

$$k = \frac{1}{2-u} \tag{3.12}$$

Although there is no evidence of the coexistence of $ZnGeN_2$ and ZnO, Formula 3.10 provides a clear description of the relationship between the elements. Furthermore, the separation of the formula is useful as one can clearly determine the parameter *k* independently from the cation and anion ratios and validate the model effectively.

By knowing the cation ratio, the relationship between parameter *k* and Zn/Ge ratio can be expressed as the following formula; here, *k* is labelled as k_c to describe the value of *k* related to the cation ratio.

$$\frac{\mathrm{Zn}}{\mathrm{Ge}} = \frac{1}{k_c} \tag{3.13}$$

Simple conversions can be made to obtain k_c expressions:

$$k_c = \frac{\mathrm{Ge}}{\mathrm{Zn}} \tag{3.14}$$

Similarly, the relationship between parameter *k* and O/N ratio can be expressed as the following formula; here, *k* is labelled as k_a to describe the value of *k* related to the anion ratio.

$$\frac{\mathrm{O}}{\mathrm{N}} = \frac{1-k_a}{2k_a} \qquad 3.15$$

The formula can be written as:

$$k_a = 1/(2 \cdot \frac{\mathrm{O}}{\mathrm{N}} + 1) \qquad 3.16$$

Herein, k_c and k_a represent the values calculated using cation ratio Zn/Ge and anion ratio O/N, respectively. Given that different methods independently measured Zn/Ge (using XRF) and O/N (using HE), the consistency between k_c and k_a reflects the validity of the model.

When plotting k_c as a function of k_a (Figure 20), one observes a clear trend between them, which can be fit using a linear formula of k_c = 1.07(3) k_a - 0.10(3). Although the fit takes into account the relative large experiment errors, it shows the behaviour of k_c with k_a largely in line with 1:1. The result reveals a significant consistency between these independently obtained values of k_c and k_a, thereby underlining the general assumption of the chemical formula $Zn_{2-u}GeO_{1-u}N_2$ and verifying that Zn-extraction (the contribution to composition represented by *u*) governs the chemical composition evolution at the later reaction stage.

As discussed in section 3.1, $Zn_{2-u}GeO_{1-u}N_2$ can adapt the wurtzite-type structure or the β-$NaFeO_2$-type structure. While the wurtzite-type structure contains 2 crystallographic sites in total, the β-$NaFeO_2$-type has 2 sites for cations and 2 sites for anions (Section 1.6). Here, the simplified $Zn_{2-u}GeO_{1-u}N_2$ formula suggests the same numbers of cations as the anions. Combining the possible crystal structures, this model implies that one would not expect an extended amount of defects, such as vacancies, on either the cation or the anion sites.

To further adapt the chemical formula to the possible crystal structures, one can convert the chemical formula from $Zn_{2-u}GeO_{1-u}N_2$ to $Zn_{1+x}Ge_{1-x}(O_xN_{1-x})_2$, with $u = (1-3x)/(1-x)$. The value of *x* is therefore in the range between 0 to 1/3 since $0 \leq u \leq 1$.

This new formula $Zn_{1+x}Ge_{1-x}(O_xN_{1-x})_2$ contains two cations and two anions in the formula unit, reflecting the cation numbers in the β-$NaFeO_2$-type structure,

demonstrating the relationship of chemical composition and crystal structure more straightforward. In addition, the parameter x in $Zn_{1+x}Ge_{1-x}(O_xN_{1-x})_2$ directly represents the amount of oxygen in compounds. Moreover, the form $Zn_{1+x}Ge_{1-x}(O_xN_{1-x})_2$ constrains the sum of cations to 2, and reflects the change in both types of cations, which facilitates the discussion on crystal structure and cation disorder in the following sections.

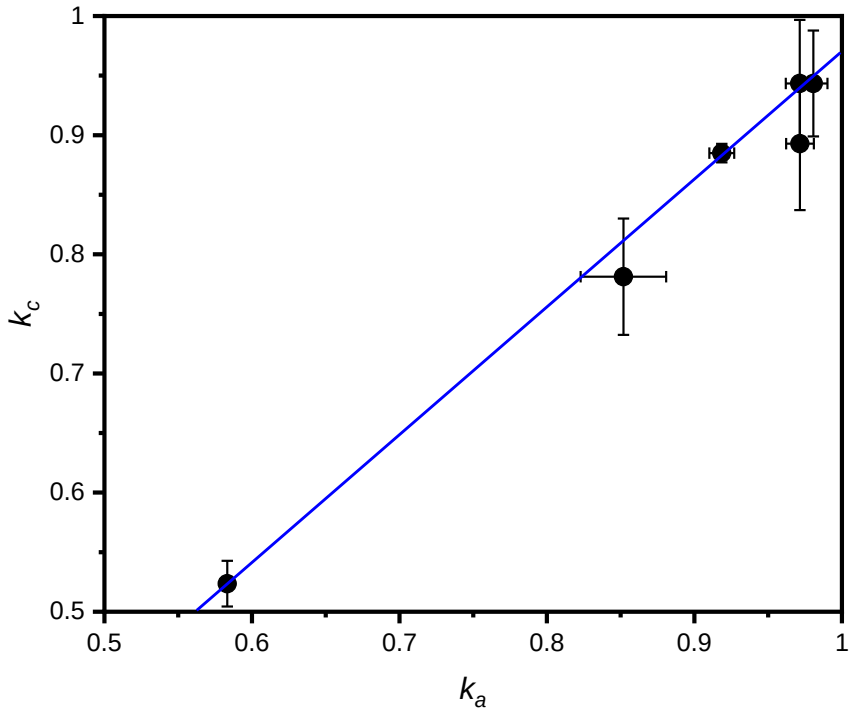

Figure 20 Plot of the parameter k as calculated from the cation ratio (k_c) independence of the same parameter as calculated from the anions ratio (k_a). The blue line signifies the linear fit $k_c = 1.07(3)\ k_a - 0.10(3)$.

3.2.4 Dynamic of the reaction

For samples of a temperature series, as dwelling time increases, the *x* index in the chemical formula $Zn_{1+x}Ge_{1-x}(O_xN_{1-x})_2$ reduces (Figure 21). There are clear linear trends between *x* and the dwelling time. The value of *x* is largely in the range between 1/3 to 0, considering the experimental error, responding to the oxygen-richest compounds and approximant towards pure $ZnGeN_2$. Furthermore, the intersections of the fitted lines with the *x*-axis are 5.8 h for 910 °C, 8.5 h for 895 °C, 12.2 h for 880 °C, 19.5 h for 865 °C and 28.3 h for 850 °C, which propose the stability limits of dwelling time under the reaction temperatures.

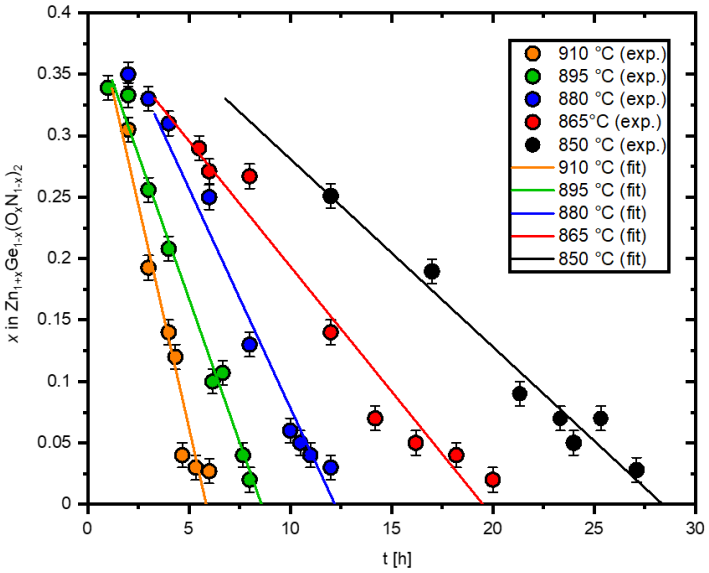

Figure 21 Plot of *x* in the chemical formula $Zn_{1+x}Ge_{1-x}(O_xN_{1-x})_2$ as the function of dwelling time *t*. Samples of different temperature series are in different colours. The lines signify the linear fit for different temperature series.

Furthermore, the fit lines steepen with increasing reaction temperature. This trend can be quantified by the slope of the linear fit (*k*) function, which represents the reaction rate constant. When plotting the natural logarithm of slope (*k*) with the reciprocal of reaction temperature (Figure 22), one can linear fit the plots using the Arrhenius equation[121-123]:

$$\ln k = -\frac{E_a}{R} \cdot \frac{1}{T} \qquad 3.17$$

where E_a is the activation energy, *R* is the gas constant with $R \approx 8.314$ J·mol^{-1}·K^{-1}, *T* is the reaction temperature. It should be noted that although we still use [°C] to describe the temperature series in Figure 22 to facilitate comparison with other figures, it is

necessary to convert T [°C] to T [K] with T [K] = T [°C] + 273.15 when performing calculations with the Arrhenius equation.

Fitting the plots by applying the Arrhenius equation (Figure 22), one obtains a fit formula with E_a = 290(21) kJ/mol. This activation energy corresponds to that of the subreaction Zn-extraction since this subreaction, Zn-extraction, predominates the composition variation in the study.

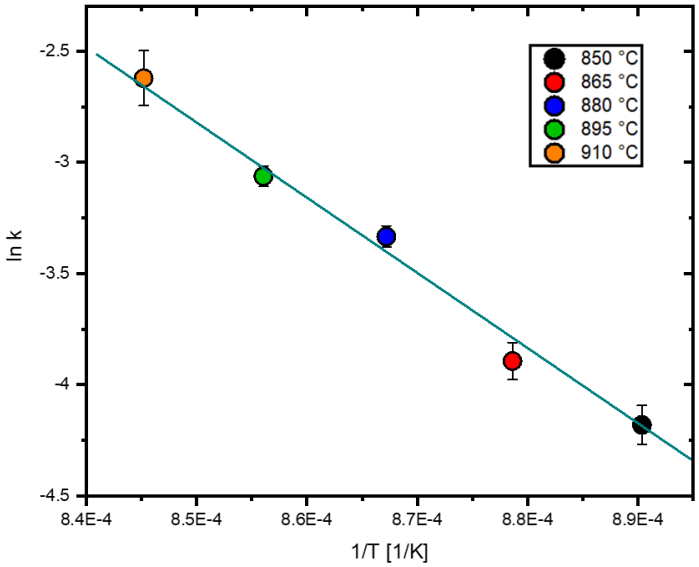

Figure 22 Plot of ln$k$ (k is the slope of linear fits in Figure 21) as a function of 1/T. The cyan line signifies the linear fit using the Arrhenius equation.

3.3 Crystal structure of $Zn_{1+x}Ge_{1-x}(O_xN_{1-x})_2$

3.3.1 Investigation of the crystal structure

Considering significant Ge and Ge_3N_4 side phases for a long dwelling over 10 hours for the series, we do not extend the study further to unstable regions. Here, we focus on the phase-pure samples of one temperature series. The samples prepared at 895 °C were taken as an exemplary series to show the change of XRD profile with dwelling time. Figure 23a shows the experimental XRD pattern of samples with LaB_6 standard in the range of 2θ between 20° and 100°.

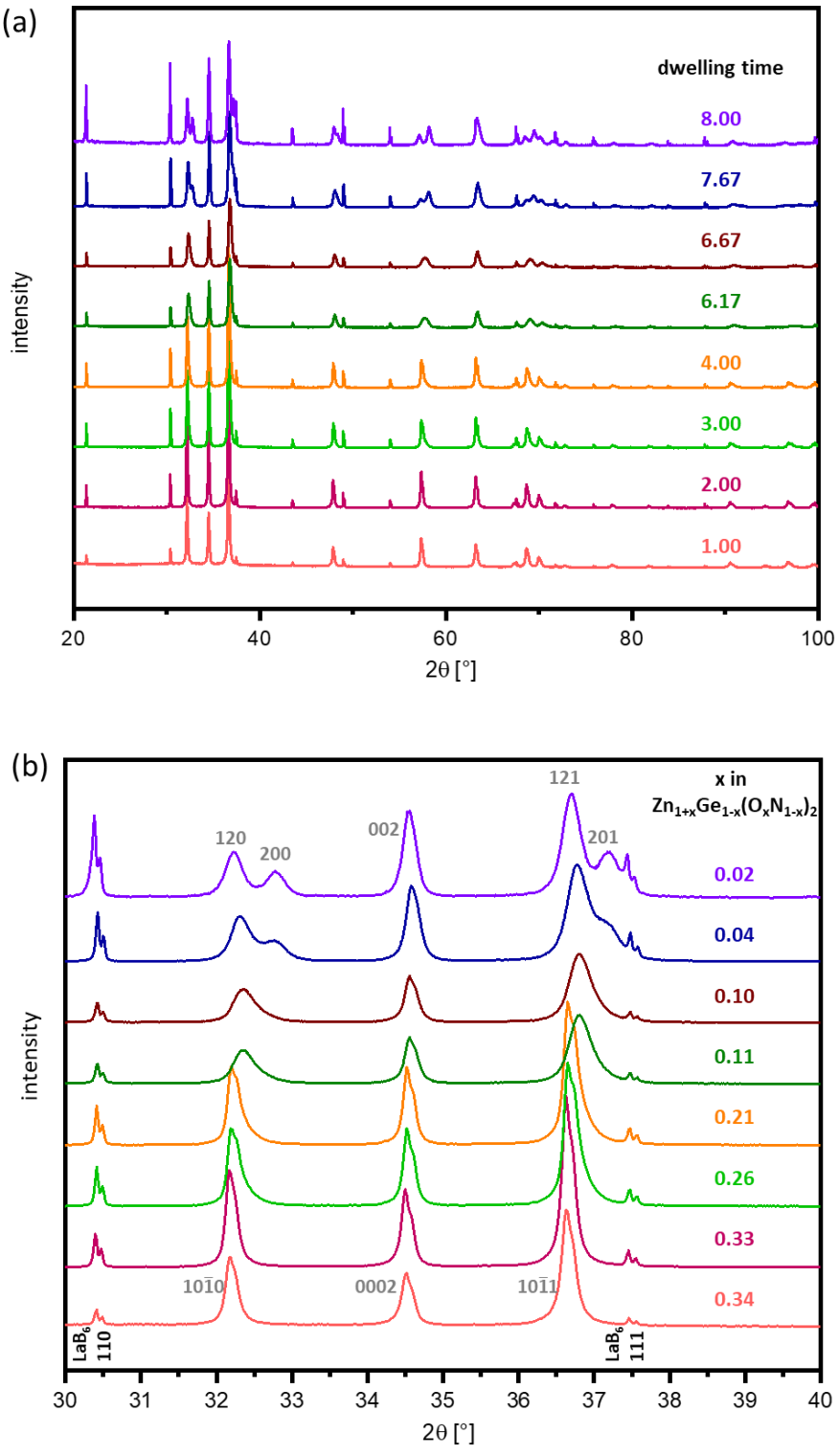

Figure 23 This figure takes samples prepared at 895 °C as an exemplary series. XRD patterns in the region of 20° – 100° 2θ (a) and 30° – 40° 2θ (b) as a function of dwelling time. The oxygen content in the chemical formula $Zn_{1+x}Ge_{1-x}(O_xN_{1-x})_2$ is indicated in (b). The reflections of $Zn_{1+x}Ge_{1-x}(O_xN_{1-x})_2$ are marked with *hkl* indices according to the hexagonal wurtzite-type structure (grey, bottom); the reflections of LaB_6 *hkl* indices according to the orthorhombic β-$NaFeO_2$-type structure (grey, top) and the *hkl* indices of LaB_6 standard (black, bottom) are given in the figure.

The three groups of strongest reflections of $Zn_{1+x}Ge_{1-x}(O_xN_{1-x})_2$ in the 2θ range between 30° - 40° are most indicative of distinguishing features of the XRD patterns (Figure 23b). In the discussed 2θ range, the oxygen-richest sample (t = 1 h, x = 0.34) shows three reflections, in line with the hexagonal wurtzite-type structure. These three reflections are indexed according to a hexagonal crystal system to $10\bar{1}0$, 0002 and $10\bar{1}1$. As the oxygen content decreases, the $10\bar{1}0$ and $10\bar{1}1$ peaks broaden asymmetrically until a clear splitting appears, indicating that the compound transforms into the β-$NaFeO_2$-type structure. However, the shape of 0002 peak is largely unaffected by the oxygen content. Therefore, one can conclude that the oxygen-rich samples ($0.10 < x < 0.34$) have the crystal structure roughly in the wurtzite-type structure. The meaning of "roughly" here is that the number and position of Bragg reflections in XRD patterns are in line with the wurtzite-type, yet the peak shape is not fully consistent with what would be expected for the wurtzite-type structure due to the broad $10\bar{1}0$ and $10\bar{1}1$ reflections, particularly for samples with $0.1 < x < 0.26$. This state, where it is difficult to define the exact crystal structure, is referred to here as the transition stage. It naturally raises the question of whether we should use the wurtzite-type structure model to describe the crystal structure of the compounds at the transition stage.

To answer this question, the peak width analysis of these peaks using WinPLOTR[124] was used to investigate the variation of peak width with chemical composition. Herein, the single peak analysis was performed for the peaks shown in Figure 23b and the responding peaks of samples in other temperature series. The peak splitting of reflections is evident in Figure 23b for $Zn_{1+x}Ge_{1-x}(O_xN_{1-x})_2$ with $x < 0.1$. Similarly, the single peak analysis was performed for the 120, 200, 121 and 201 peaks that appeared after splitting.

The plot of the peak width (FWHM) is shown in Figure 24 as a function of the oxygen content. Two horizontal straight lines exhibit the peak width of 110 and 111 reflections of the standard LaB_6. These two peaks are at 2θ of 30.4° and 37.5°, respectively. This 2θ range ($30.4° < 2\theta < 37.5°$) encompasses the three groups of strongest reflections of $Zn_{1+x}Ge_{1-x}(O_xN_{1-x})_2$ (Figure 23b). The peak widths of the two peaks can be seen as a representation of the upper and lower limits of the instrument-based peak widths in the discussed 2θ range since the LaB_6 is the reference specifically for the XRD device calibration.

Compared with the peak width of standard LaB_6, even the 0002 peak of $Zn_{1+x}Ge_{1-x}(O_xN_{1-x})_2$ that is not expected to split, is much broader than the standard LaB_6 peaks, indicative of the small domain size or microstrain in the samples.

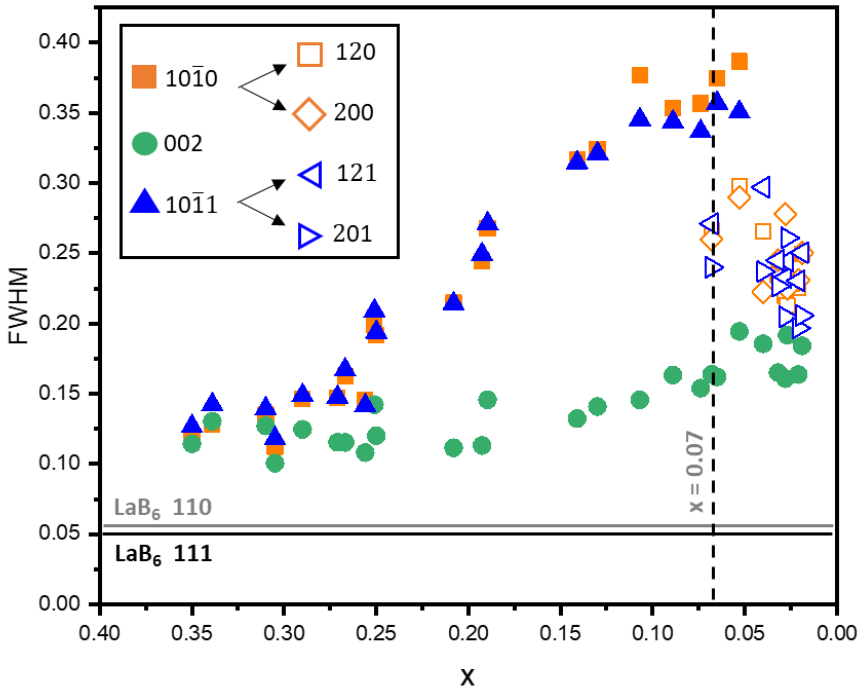

Figure 24 FWHM of $10\bar{1}0$, 120, 200, 002, $10\bar{1}1$, 121 and 201 peaks in patterns of $Zn_{1+x}Ge_{1-x}(O_xN_{1-x})_2$ and FWHM of 110 and 111 peaks of standard LaB_6 as the function of oxygen content (represented by x) of $Zn_{1+x}Ge_{1-x}(O_xN_{1-x})_2$.

The broadening of the $10\bar{1}0$ and $10\bar{1}1$ peak becomes more and more pronounced as x decreases (Figure 23b). FWHM of the $10\bar{1}0$ and $10\bar{1}1$ peak increases as oxygen content (represented by x) decrease until $x \approx 0.07$ (Figure 24). When x decreases to approximately 0.07, the peak splitting is evident. The peak analysis was further performed to the split peaks 120, 200 and peaks 121, 201, instead of $10\bar{1}0$ and $10\bar{1}1$. The relationship of the peaks is shown in Figure 24 inset and is highlighted in colours.

All samples exhibit a broader $10\bar{1}0$ and $10\bar{1}1$ peaks than the 0002 peak, with the exception of the oxygen richest sample with $x = 0.34(1)$, which corresponds to the sample at the very beginning of the reaction stage. The phenomenon for this material that with a broader $10\bar{1}0$ and $10\bar{1}1$ peak than 0002 peaks, suggests that the $10\bar{1}0$ peak and $10\bar{1}1$ peak of these samples are probably contributed by two refections close together; their profiles overlap into one peak.

In addition, one detail worth noting is that the tail of the $10\bar{1}0$ peak expands toward the larger 2θ. This asymmetry shape is reasonable because the intensity of the 120 peak, which is located at the smaller 2θ than 200 peak, is significantly greater than the intensity of the 200 peak (Figure 23b). Once the peak splitting has occurred while the two peak parts are not yet clearly separated, their overlap must lead to this asymmetric peak shape.

Therefore, the wurtzite-type structure model is not able to reflect peak splitting hidden in the asymmetric broadening for the samples at the transition stage. For this, we apply the β-$NaFeO_2$-type structure to describe the crystal structure of $Zn_{1+x}Ge_{1-x}(O_xN_{1-x})_2$. The reason is that most samples are with x in the range of $0 < x < 0.34(1)$ can be seen as in the transition stage. On the other hand, because the β-$NaFeO_2$-type structure space group is a subgroup of the wurtzite-type, one can refine patterns for all samples using the β-$NaFeO_2$-type model.

It is worth noting that if the peak splitting in the diffraction pattern is not obvious, the refinement using the orthorhombic β-$NaFeO_2$-type model can be more challenging to converge. The reason is that the two peaks that should split overlap almost exactly at the same 2θ if peak splitting is not obvious, leading to a strong correlation between the lattice constant *a* and *b*. Therefore, we use smaller relaxation factors of the shifts of the refined parameters in refinement to stabilise the refinement, although it consumes more computing time.

The wurtzite-type structure model was additionally used to refine the crystal structure for the diffraction patterns where the peak splitting is not obvious. The lattice constants and related information can be found in the Appendix (Table S4).

3.3.2 Lattice constants of $Zn_{1+x}Ge_{1-x}(O_xN_{1-x})_2$ and quantification of the crystal structure transformation

The lattice constants of $Zn_{1+x}Ge_{1-x}(O_xN_{1-x})_2$ are obtained by performing Rietveld and Le Bail refinements of diffraction patterns using the orthorhombic β-$NaFeO_2$-type structure model. While the parameter *a* and *b* vary significantly over the composition range, *c* is largely unaffected by the composition change (Figure 25).

For samples in the oxygen-rich regime ($0.07 < x < 0.34(1)$), the parameters *a*, *b* shrink with *x* decreases, leading to a clearly decreasing unit cell volume trend (Figure 26). The shrinking of the unit cell is rationalised by taking into account the Shannon radii of the cations: $r(Zn^{2+})$ = 0.6 Å and $r(Ge^{4+})$ = 0.39 Å.[125] For a decreasing *x* parameter, the fraction of the larger Zn^{2+} cation decreases. Thus, it results in a shrinking of the unit cell volume. In the oxygen-poor regime ($0 < x < 0.07(1)$), the *b* parameter grows rapidly until the compounds approach stoichiometric $ZnGeN_2$, i.e. $x = 0$. The abrupt change in the trend of parameter *b* indicates a significant phase change has occurred in the material in the composition range around $x = 0.07$. Therefore, when taking into account the overall trend of the lattice parameters over the composition range, it is clear that one can determine two distinct regions, i.e. the range of $0.07 < x < 0.34(1)$ and the range of $0 < x < 0.07(1)$.

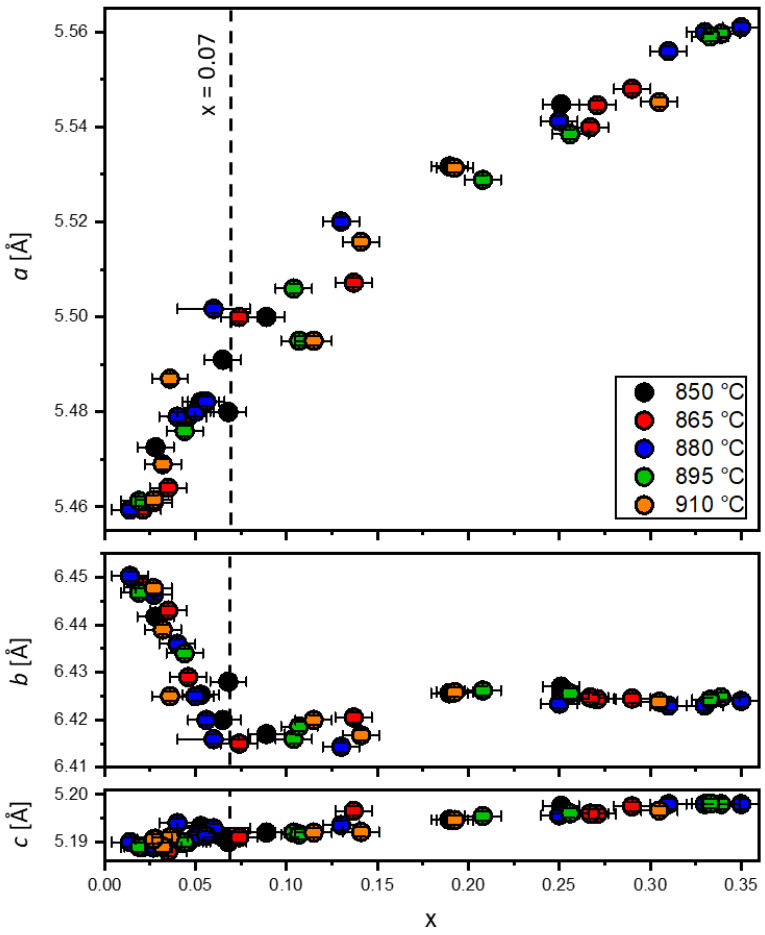

Figure 25 Change of the lattice parameters *a*, *b* and *c* as a function of the oxygen content. Plots in black, red, blue, green and orange represent the samples prepared at 850°C, 865°C, 880°C, 895°C and 910 °C.

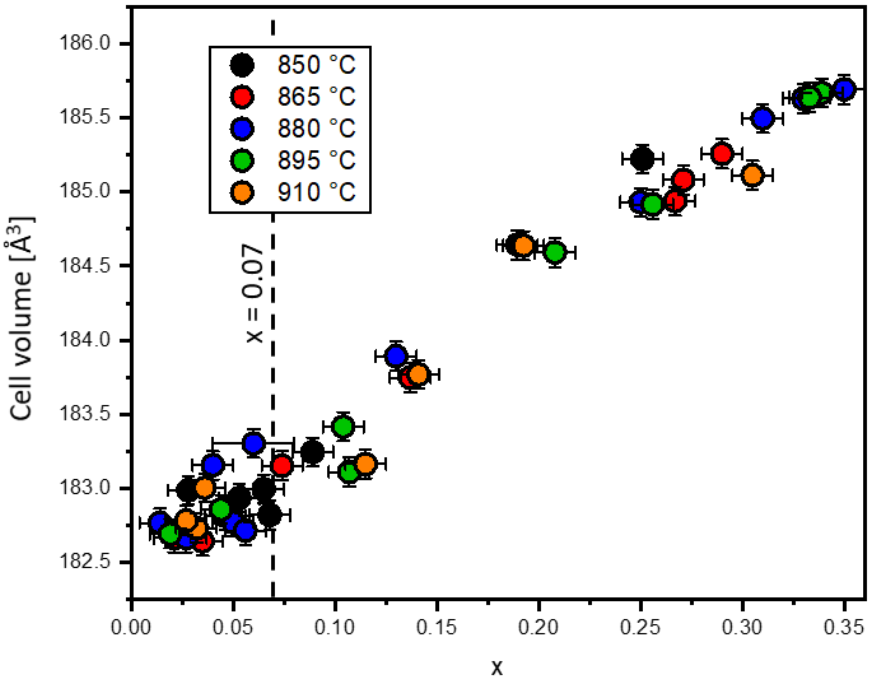

Figure 26 Change of the unit cell volume as a function of oxygen content.

As discussed in Section 3.3.1 with peak analysis, the samples we studied are mainly in the transition stage between the wurtzite-type structure and the β-$NaFeO_2$-type structure. In order to quantify the stage of the crystal structural transformation, one can describe the transformation stage by means of the deviation of the crystal structure from an idealised wurtzite-type structure. For this, the lattice parameters could be used to study the crystal structure in the transition stage quantitatively. Some of the literature uses *b*/*a* ratio to quantify the structure distortion for Zn-IV-N_2 (IV: Ge, Sn).[69, 126] It is useful to compare the lattice parameters *a* and *b* to determine whether the crystal structure is in the hexagonal setting. The *b*/*a* ratio of the orthorhombic β-$NaFeO_2$-type model for a hexagonal crystal structure must be $2/\sqrt{3}$ due to $a_{h1} = a_{h2}$ and γ =120° (Figure 27).

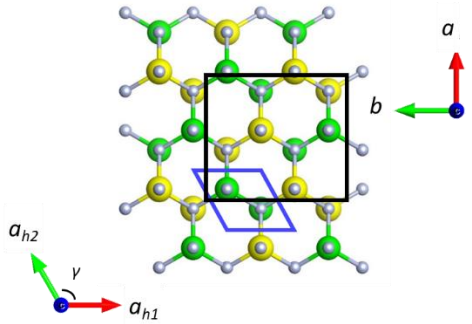

Figure 27 Schematic illustration of the relationship of lattice parameters between the orthorhombic β-$NaFeO_2$-type model and the hexagonal wurtzite-type model.

However, while the *b*/*a* ratio reflects the structural distortion in the ***a*-*b*** plane, it neglects the effect of lattice volume change and lattice constant *c*. Thus, according to the unit cell setting of an idealised wurtzite-type and β-$NaFeO_2$-type structure (Figure 27),[54] the factor α was established in this section to describe the crystal structural distortion. The factor α is expressed as:

$$\alpha = \frac{a_{h1} - a_{h2}}{\sqrt[3]{V_h}} \quad 3.18$$

where α is the crystal structural distortion parameter, a_{h1} and a_{h2} are the pseudo-hexagonal lattice parameter related to the orthorhombic lattice parameters as:

$$a_{h1} = \frac{b}{2} \quad 3.19$$

$$a_{h2} = \frac{a}{\sqrt{3}} \quad 3.20$$

V_h is the cell volume of the pseudo-hexagonal unit cell, is one-fourth of the volume of the orthorhombic unit cell.

$$V_h = \frac{abc}{4} \quad 3.21$$

Figure 28 shows the plot of the distortion factor (α) as a function of the oxygen content (x). The factor α obtained by experiments lies in a range between 0 for an idealised hexagonal unit cell and 0.023(3), which is in line with the value postulated by DFT crystal structure optimisation for ordered β-$NaFeO_2$-type $ZnGeN_2$ (Table 2).[44, 54, 65]

When approaching $ZnGeN_2$, i.e. $x \approx 0$, the distortion parameter α reaches the maximum of 0.023, suggesting that oxygen-poor $Zn_{1+x}Ge_{1-x}(O_xN_{1-x})_2$ in the β-$NaFeO_2$-type.[44, 54, 65] The distortion parameter α decreases with increasing oxygen content (represented by x), indicating a crystal structural transition towards the hexagonal crystal structure. One can observe a change in the slope of the profile at the stage of $x \approx 0.07$ with $\alpha \approx 0.01$. The value of α eventually approaches 0 until $x \approx 0.34$, suggesting the wurtzite-type structure for $Zn_{1+x}Ge_{1-x}(O_xN_{1-x})_2$ in the oxygen-richest regime.

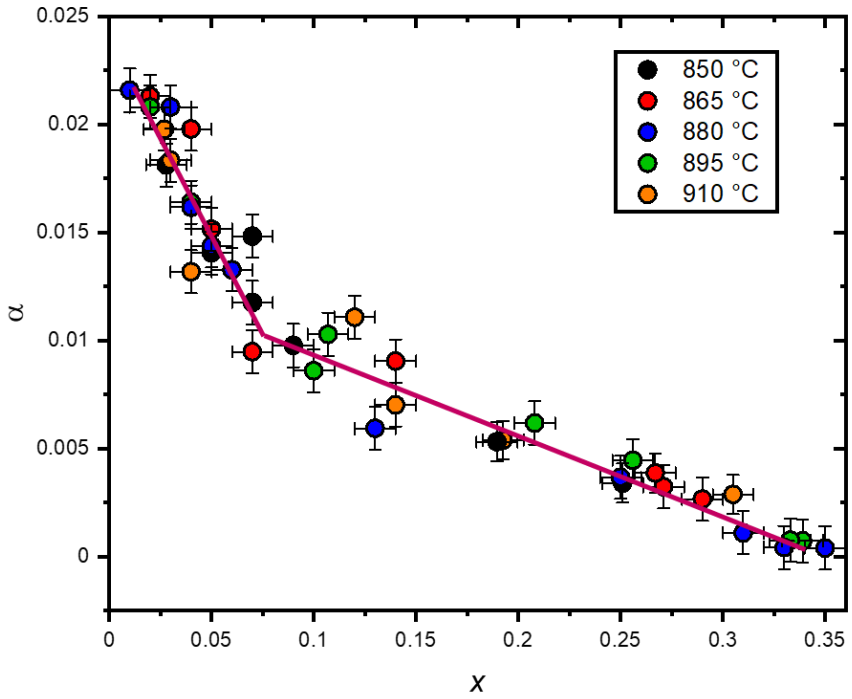

Figure 28 Plot of the distortion factor α as a function of parameter *x* in the chemical formula $Zn_{1+x}Ge_{1-x}(O_xN_{1-x})_2$, and segmented linear trendline (dark red).

Table 2 Lattice constant *a*, *b*, *c* of β-$NaFeO_2$-type $ZnGeN_2$ postulated by DFT calculation in literature, and the responding distortion factor α calculated using Formula 3.18.

Ref.	*a* / Å	*b* / Å	*c* / Å	α
Paudel[44]	5.36	6.33	5.11	0.020
Qualye[54]	5.522	6.521	5.264	0.020
Lambrecht[65]	5.413	6.388	5.156	0.194

3.4 Understanding cation disorder in $Zn_{1+x}Ge_{1-x}(O_xN_{1-x})_2$

Cation disorder, as discussed in Section 1.4, prevalent in Zn-IV-N_2 (IV: Ge, Sn), governs the crystal structure of the compounds. While the fully ordered case adopts the energetically favourable β-$NaFeO_2$-type structure, the compound crystallises into the wurtzite-type structure with fully disordered cations. In literature, discussions on cation disorder, including the exchange of $Zn2^+$-IV^{4+}, [44, 54, 75, 127] and combination of different structural segments,[65] are mainly based on the assumption of a stoichiometric Zn-IV-N_2 (IV: Ge, Sn).

This section extends the discussion of cation disorder to $Zn_{1+x}Ge_{1-x}(O_xN_{1-x})_2$, where $Zn/Ge \neq 1$. This raises new questions about how cation disorder is triggered and affected in $Zn_{1+x}Ge_{1-x}(O_xN_{1-x})_2$.

Herein, the cation disorder in $Zn_{1+x}Ge_{1-x}(O_xN_{1-x})_2$ is classified into intrinsic disorder and extrinsic disorder according to the different causes of disordered cations, followed by a discussion on the challenges and opportunities that come with them.

Furthermore, this section discusses the experimental study about the cation disorder in $Zn_{1+x}Ge_{1-x}(O_xN_{1-x})_2$. The analysis of cation disorder is based on understanding cation distribution in the crystal structure through site occupancy factor (SOF). The simultaneous Rietveld refinement of neutron diffraction data together with XRD data was performed to investigate site occupancy factor (SOF), which can describe the long-range cation distribution in the crystal structure. Combining cation distribution with the crystal structure and synthesis conditions allows drawing a comprehensive insight into the cation disorder in this material.

3.4.1 Intrinsic and extrinsic cation disorder

Intrinsic cation disorder

Herein, the intrinsic cation disorder refers to Zn-IV anti-sites, i.e. a pair of point defects (Zn_{IV} and IV_{Zn}) resulting from Zn^{2+} and IV^{4+} cation exchanging positions in the ordered structure (Figure 29 blue arrow). Because the anti-site defect must be preceded by defining two distinct cation sites in the crystal structure, the discussion of Zn-IV anti-site should be on the basis of the β-$NaFeO_2$-type structure model rather than the wurtzite-type. One cannot classify the anti-site defect based on the wurtzite-type model

since only one Wyckoff position 2b for cations in a wurtzite-type model. With an increasing degree of intrinsic cation disorder, the crystal structure ends up with site occupancy of 50% Zn^{2+} and 50% IV^{4+} for each cation site in Zn-IV-N_2 (IV: Ge, Sn), having a statistical distribution of cations.

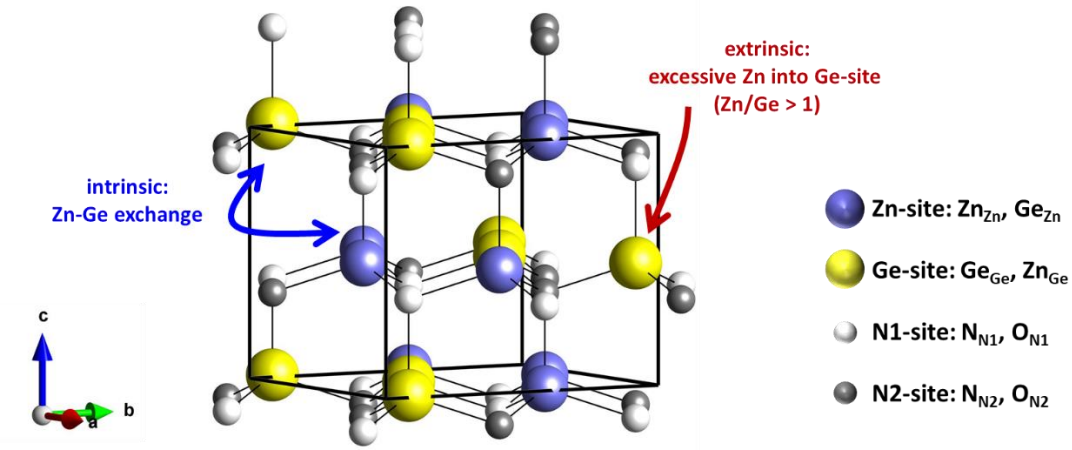

Figure 29 Illustration of the structure model for $Zn_{1+x}Ge_{1-x}(N_{1-x}O_x)_2$.

The Zn-IV anti-sites are the most energetically favourable point defect, according to Skachkov's calculation regarding a Zn-Ge-N exemplary system.[128] It is postulated by DFT calculation that this type of cation disorder in Zn-IV-N_2 (IV: Ge, Sn) efficiently narrows the bandgap.[75] Similar phenomena were observed in ternary phosphides such as $ZnGeP_2$ and $ZnSnP_2$.[129, 130] The local environment related to the anti-sites determines the overall behaviour of the optical bandgap value.[74, 131] At present, the study of bandgap narrowing due to cation disorder are mainly based on computational studies. The reason for the bandgap narrowing might be attributed to an intermediate band in the gap at the high disorder concentration,[75, 128] near-band edge tailing by the localisation effects,[74] or other effects on the electronic structure by the charge of motifs or orbital coupling.[127]

While it is not yet clear how exactly the bandgap is affected by this type of cation disorder, it is still a potential strategy to engineer the bandgap by utilising the unique disordered-based bandgap tunning mechanism.

Extrinsic cation disorder

Herein, the extrinsic cation disorder in $Zn_{1+x}Ge_{1-x}(O_xN_{1-x})_2$ represents the disordered cation caused by impurities, such as oxygen impurities and off-stochiometry. Oxygen impurities in nitrides come from many sources, such as: a) O-containing precursors –

oxygen is not completely eliminated during the synthesis process,[78] b) the growth environment - oxygen and H_2O in the reaction atmosphere cannot be fully avoided.[132] For $Zn_{1+x}Ge_{1-x}(O_xN_{1-x})_2$, impurities are present as oxygen incorporation in the crystal structure where oxygen ions share the same crystallographic position as nitrogen ions.[120] It is postulated by DFT that oxygen clustering with Zn-rich local motifs is energetically favourable.[78] Though it is still unclear what role oxygen incorporation plays in the local arrangement of cations, this finding hints that oxygen incorporation might lead to Zn-rich clustering affecting short-range cation disorder.[78]

Further to oxygen incorporation, another relevant extrinsic disorder in $Zn_{1+x}Ge_{1-x}(O_xN_{1-x})_2$ could be excessive Zn_{IV} or IV_{Zn}, which is prevalent due to the off-stoichiometry of compounds. The reason is that Zn/Ge ratio ($\neq 1$) in compounds is inconsistent with Zn-site/Ge-site (= 1) in the crystal structure. When Zn/Ge $\neq 1$ in a $Zn_{1+x}Ge_{1-x}(O_xN_{1-x})_2$, The cation that is in the majority necessarily encroaches on the site of another cation, forming Zn_{IV} or IV_{Zn} defects (Figure 29 red arrow).

For $Zn_{1+x}Ge_{1-x}(O_xN_{1-x})_2$, oxygen incorporation and Zn/Ge ratio are related to the chemical composition of compounds. Some reports postulated that tuning the chemical composition can achieve a superior carrier transport performance at perfect short-range order,[76] and forming charge-neutral defect by Zn_{Sn} and O_N reduces the degenerate carrier concentration.[126] Although the extrinsic disorder necessarily depends on the chemical composition, it is still unclear how exactly extrinsic disorder affects the material properties while tuning compositions. Experimental investigation of these types of cation disorders is currently an underexplored area of research.

3.4.2 Relationship of cation disorders with site occupancy factor (SOF)

The last section introduces extrinsic disorder and intrinsic cation disorder, respectively. This section discusses the relationship between extrinsic and intrinsic cation disorders and their relation to the cation distribution in the crystal structure, facilitating the understanding of how to quantitatively analyse the cation disorders based on the site occupancy factor (SOF).

First, it is essential to understand the order-disorder transformation from a pure crystal structural point of view to understand SOF in $Zn_{1+x}Ge_{1-x}(O_xN_{1-x})_2$. Assuming a compound with fixed composition on the pure crystal structural perspective, the overall

disordered state of compounds is conceivable in a way that the disordered state results from the facile exchange of cations of different cation sites of an ordered state (Figure 30).

In this study, all $Zn_{1+x}Ge_{1-x}(O_xN_{1-x})_2$ are Zn-rich with Zn/Ge > 1. The most ordered state of the crystal structure is that Zn fully occupies Zn-site, and the excess zinc occupies part of the Ge-site, forming extrinsic disorder Zn_e (Figure 30 top).

In addition to the most ordered $Zn_{1+x}Ge_{1-x}(O_xN_{1-x})_2$, the Zn-Ge exchange causes the pairs of Ge_{Zn} (represented by Ge_i) and additional Zn_{Ge} (represented by Zn_i), which are the intrinsic disordered in $Zn_{1+x}Ge_{1-x}(O_xN_{1-x})_2$. Then, the pairs of Ge_{Zn} and additional Zn_{Ge} are accessible due to the exchange of Zn_{Zn} and Ge_{Ge} (Figure 30 bottom).

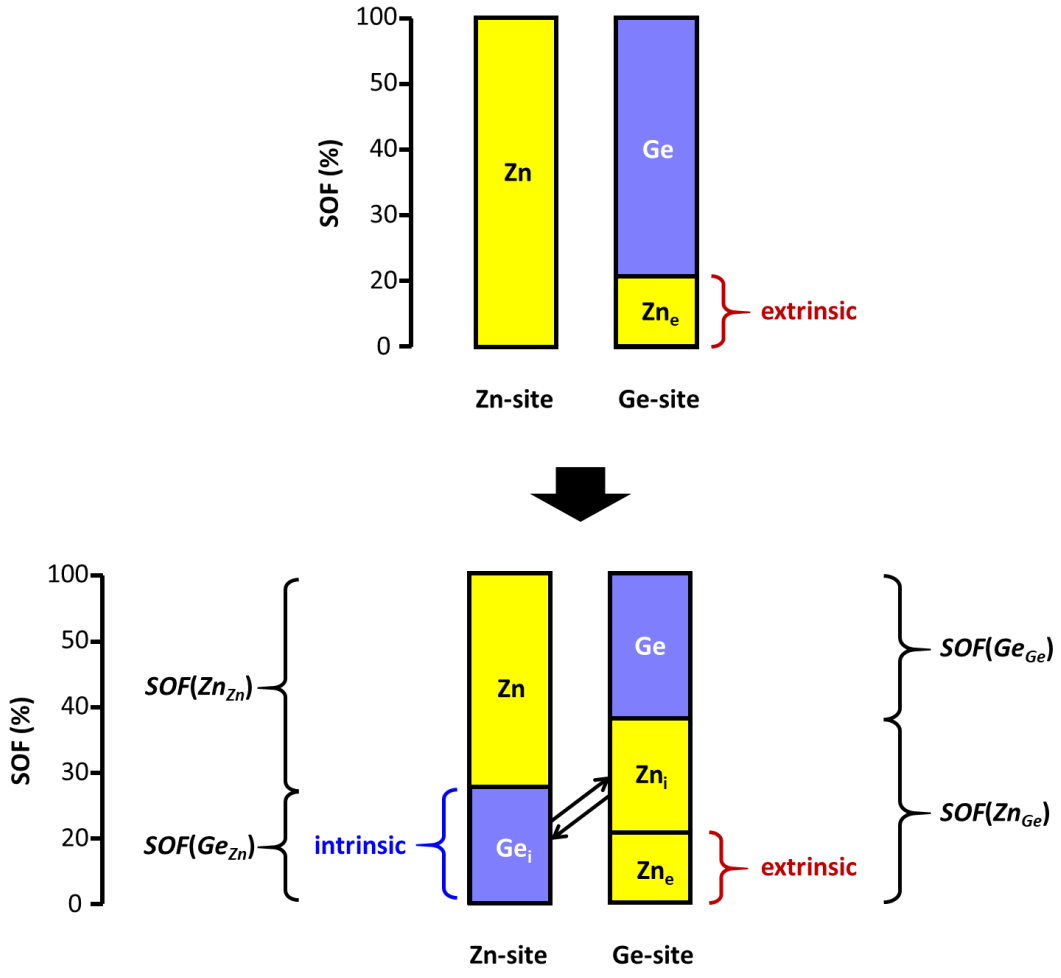

Figure 30 Illustration of a conceivable order-disorder transformation, and the relationship of cation disorder with SOF, which can be obtained by Rietveld refinement. Zn_{Zn} represents Zn on Zn-site, Ge_{Zn} represents Ge on Zn-site, Zn_{Ge} represents Zn on Ge-site and Ge_{Ge} represents Ge on Ge-site. Zn_e stands for extrinsic disorder on Ge-site. Zn_i an Ge_i represents the intrinsic disorder caused by Zn-Ge exchange.

Using Rietveld refinement, one is able to deconvolute the site occupancy factor (SOF) of atoms on crystallographic sites (Section 2.2.1). Herein, the *SOF*(Zn_{Zn}), *SOF*(Ge_{Zn}) are the fraction of Zn or Ge on the Zn-site, the *SOF*(Zn_{Ge}), *SOF*(Ge_{Ge}) are the fraction of Zn or Ge on the Ge-site (Figure 30 bottom). These SOF values are accessible by simultaneous refinement. No vacancies are considered using the form $Zn_{1+x}Ge_{1-x}(O_xN_{1-x})_2$, thus:

$$SOF(Zn_{Zn}) + SOF(Ge_{Zn}) = 1 \quad 3.22$$

$$SOF(Zn_{Ge}) + SOF(Ge_{Ge}) = 1 \quad 3.23$$

The relationship between intrinsic disorder Ge_i and Zn_i, Ge_i and the SOF obtained with Rietveld refinement is:

$$Ge_i = Zn_i = SOF(Ge_{Zn}) \quad 3.24$$

The amount of extrinsic disorder can be expressed as:

$$Zn_e = 1 - SOF(Ge_{Ge}) - Zn_i \quad 3.25$$

which can be written as the following formula by combining with Formula 3.24:

$$Zn_e = 1 - SOF(Ge_{Ge}) - SOF(Ge_{Zn}) \quad 3.26$$

For the fully disordered state of $Zn_{1+x}Ge_{1-x}(O_xN_{1-x})_2$, the cation should be distributed statistically in the two cation sites, hence:

$$SOF(Ge_{Ge}) = SOF(Ge_{Zn}) = \frac{1-x}{2} \quad 3.27$$

$$SOF(Zn_{Ge}) = SOF(Zn_{Zn}) = \frac{1+x}{2} \quad 3.28$$

$$Zn_e = x \quad 3.29$$

Therefore, the maximal intrinsic cation disorder is a function of the chemical composition with (1-*x*)/2. On the other hand, the extrinsic cation disorder correlates directly with the chemical composition.

3.4.3 Simultaneous Rietveld refinement of neutron and XRD data sets

In order to experimentally study the cation disorder in $Zn_{1+x}Ge_{1-x}(O_xN_{1-x})_2$, in which there are isoelectronic Zn^{2+} and Ge^{4+}, neutron diffraction was performed to investigate

the site occupancy factor (SOF) based on an orthorhombic β-$NaFeO_2$-type structural model (Figure 29). Knowing the SOF allows us to understand the long-range cation disorder in the material through the distribution of Zn and Ge in cation sites. Furthermore, the XRD data was simultaneously refined with the neutron data. While XRD is not suitable for distinguishing Zn^{2+} and Ge^{4+} in compounds, high-resolution data is accessible through this method to gain accurate lattice constants, particularly measuring the synthesised powder together with reference LaB_6. Therefore, simultaneous refinement of neutron diffraction data with XRD data can significantly increase the accuracy of results, as it takes advantage of both diffraction methods.

The simultaneous Rietveld refinement of neutron diffraction and XRD data is performed using FULLPROF[99]. It is possible to simulate the situation in which different atoms occupy the same site by constraining the atomic coordinates (x, y, z) in this program to reflect the intrinsic and extrinsic cation disorders.

In this work, the Zn and Ge on the Zn-site are refined with the same coordinates (x_1, y_1, z_1). The cations on the Ge-site are refined with (x_2, y_2, z_2). O and N can occupy the anion sites N1-site and N2-site. Similarly, the anions on the N1-site and N2-site are refined with coordinates (x_3, y_3, z_3) and (x_4, y_4, z_4), respectively.

The initial site occupancy factors can be set as if the crystal structure of the $Zn_{1+x}Ge_{1-x}(O_xN_{1-x})_2$ is in the most ordered state, with:

$$SOF(Zn_{Zn}) = 1 \tag{3.30}$$

$$SOF(Ge_{Zn}) = 0 \tag{3.31}$$

$$SOF(Zn_{Ge}) = x \tag{3.32}$$

$$SOF(Ge_{Ge}) = 1 - x \tag{3.33}$$

Furthermore, to simulate the intrinsic cation disorder caused by the exchange of Zn and Ge, the SOF of the different ions must be correlated. In this FULLPROF[99], the correlation between SOFs can be realised by restraining the change of SOFs (ΔSOF).

For Zn-Ge exchange in $Zn_{1+x}Ge_{1-x}(O_xN_{1-x})_2$, whenever Zn enters the Ge-site from the Zn-site, the same amount of Ge must enter the Zn-site from the Ge-site. The number of atoms on each site should be maintained.

Therefore, for Zn, the decrease in *SOF*(Zn_{Zn}) must be equal to the increase in SOF(Zn_{Ge}):

$$-\Delta SOF(Zn_{Zn}) = \Delta SOF(Zn_{Ge}) \quad 3.34$$

Similarly, for Ge, the increase in *SOF*(Ge_{Zn}) must be equal to the decrease in *SOF*(Ge_{Ge}):

$$\Delta SOF(Ge_{Zn}) = -\Delta SOF(Ge_{Ge}) \quad 3.35$$

Meanwhile, Zn and Ge change by exactly the opposite amount on each site:

$$\Delta SOF(Zn_{Zn}) = -\Delta SOF(Ge_{Zn}) \quad 3.36$$

$$\Delta SOF(Zn_{Ge}) = -\Delta SOF(Ge_{Ge}) \quad 3.37$$

Thus, the correlation of the SOF of all the involved cations can be described by the following formula:

$$\Delta SOF(Zn_{Zn}) = -\Delta SOF(Zn_{Ge}) = \Delta SOF(Ge_{Ge}) = -\Delta SOF(Ge_{Zn}) \quad 3.38$$

By the same token, the relationship between the anions can be expressed as:

$$\Delta SOF(N_{N1}) = -\Delta SOF(N_{N2}) = \Delta SOF(O_{N2}) = -\Delta SOF(O_{N1}) \quad 3.39$$

In addition to the crystal structure model, the software can realise the simultaneous calculation of the diffractograms for the identical model to reflect the fact that the Neutron and XRD patterns are from the same compound. Therefore, we performed the strategy to refine multiple diffraction patterns using a composite refinement method, to increase the reliability of the calculation (Table 3).

It is worth noting that LaB_6 powder as the reference was added into $Zn_{1+x}Ge_{1-x}(O_xN_{1-x})_2$ powder for XRD experiments to enhance the accuracy of lattice parameter calculation. Thus, the additional LaB_6 phase should be involved in the refinement of the XRD pattern. As we use LaB_6 only to calibrate the zero shift of the XRD pattern without involving the atomic details of LaB_6, the Le Bail method was used to calculate the LaB_6 phases of the XRD pattern to reduce the time consumption of the calculations.

Table 3 Strategy of the simultaneous refinement as shown in a brief table description.

Experimental data	Neutron diffraction pattern	XRD pattern	
Phases	oxide nitride	oxide nitride	LaB_6
Refinement method	Rietveld		Le Bail

In the present work, all parameters related to the material itself, including

a. lattice constants,
b. atomic coordinations,
c. displacement factors,
d. SOFs,
e. spherical harmonics,

were refined simultaneously for the neutron diffraction and the XRD pattern to reflect the material consistency for different experiments.

Other parameters that are relevant to or affected by experimental conditions, including:

a. zero point,
b. systematic shift,
c. scale factor,
d. peak function parameters,
e. asymmetry parameters,
f. background parameters,

were refined independently according to the experiment setup. Figure 31 shows plots of neutron diffraction and XRD with the simultaneous refinement method. Further plots of refinement are shown in Appendix.

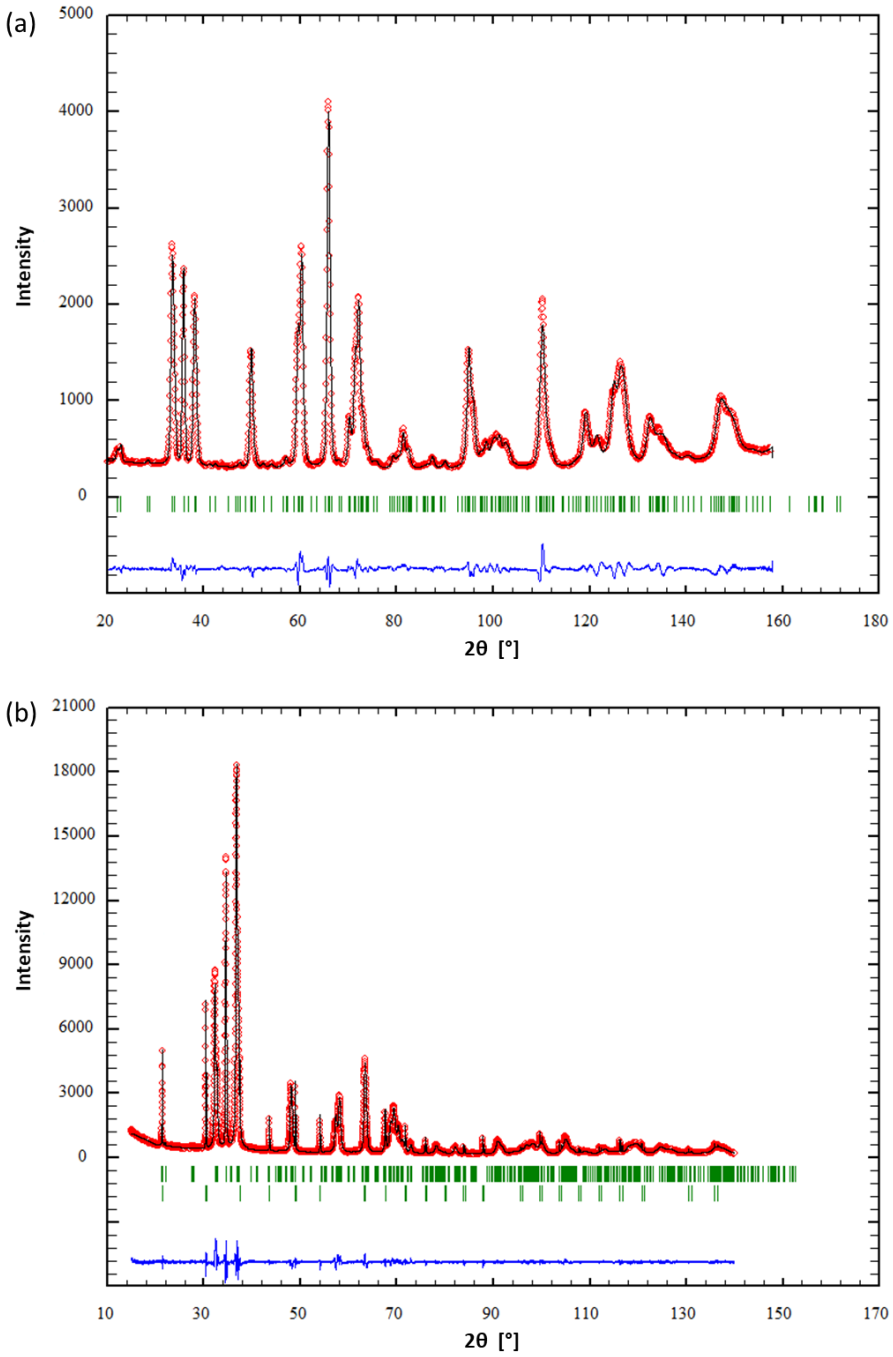

Figure 31 Plot of simultaneous refinement of neutron pattern (a) and XRD pattern (b): measured intensities (red circles), calculated profile (black line), the difference between measured and calculated intensities (blue line), and calculated reflection positions (green ticks, $Zn_{1+x}Ge_{1-x}(O_xN_{1-x})_2$ in (a) and top in (b), LaB_6 bottom in (b)).

3.4.4 Cation disorder in the crystal structure

When plotting the extrinsic cation disorder Zn_e as a function of the chemical composition, all plots match the linear formula $f(x) = x$ (Figure 32). The rationale is that the extrinsic cationic disorder essentially reflects the excessive Zn over the Ge-site due to the off-stochiometry and correlates directly to the chemical composition. Furthermore, the refinement uses a chemical constraint based on the chemical formula $Zn_{1+x}Ge_{1-x}(N_{1-x}O_x)_2$, no considering the extended amount of vacancies; hence the share of cations in the unit cell is fixed. Thus, the great consistency between Zn_e and x confirms the validity of the chemical constraint used in the refinement.

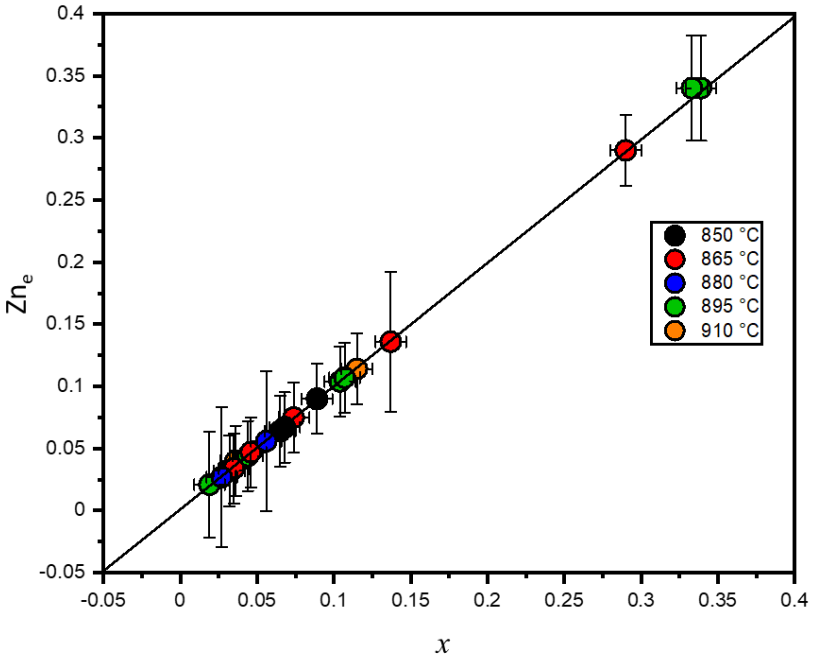

Figure 32 Plot of extrinsic cation disorder Zn_e as a function of chemical composition (represented by x). The black line represents the function that $f(x) = x$.

On the contrary to extrinsic disorder, there is no clear trend between intrinsic cation disorder (represented by Ge_{Zn}) and oxygen content (represented by x) (Figure 33). Nevertheless, a general phenomenon can be observed that while the samples with the lowest degree of the intrinsic disorder appear in the oxygen-poor region, the sample with the most intrinsic disorder has a significant amount of oxygen content.

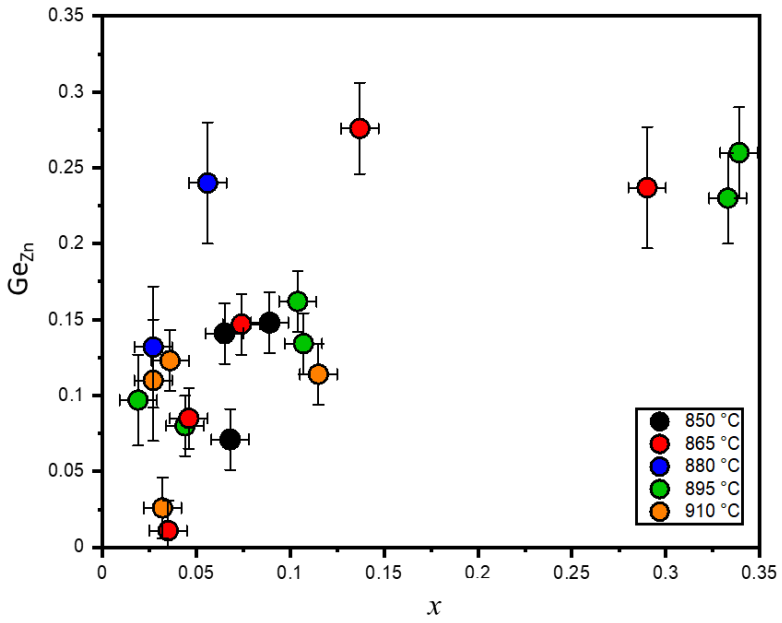

Figure 33 Plots of intrinsic disorder (here represented directly by Ge_{Zn}, instead of Ge_i or Zn_i) as a function of chemical composition (represented by x).

While plotting Ge_{Zn} as a function of the dwelling time, one observes clear trends between them for a temperature series (Figure 34). However, due to the time limitation of beamtime, we only measured a limited number of samples for different temperature series by different instruments (section 2.1.3), so here we fit data points that exhibit a linear trend with a straightforward linear function to reflect the trend of intrinsic cation disorder over time. While the fits suffer from relatively large experimental errors, it is clear that as the dwelling time t decreases, the amount of intrinsic cation disorder reduces towards 0. The compounds are predicted to be fully ordered when $Ge_{Zn} = 0$. Based on the fit lines here, we can infer that a completely ordered structure might appear with the reaction conditions 6 hours for 910 °C, 9.5 hours for 895 °C, 14.1 hours for 880 °C, 18.3 hours for 865 °C and 29.4 hours for 850 °C, in a great consistency with the stability limits predicted by the dynamic of reaction in Section 3.2.4 (Figure 34 square symbols). This consistency of longest dwelling time predicted by independent methods suggests the validity of these fitting and that the pure $ZnGeN_2$ tends to be ordered. In addition, it should be noted that these analyses are based on simple statistics for a limited number of data points and are more validating for sample regions that tend to be ordered. For samples with short reaction times (relative to the reaction times for

each temperature series), significant deviations can be observed, e.g. Ge_{Zn} values for samples 895 °C for 1 hour, 895 °C for 2 hours and 865 °C for 5.5 hours are significantly smaller than predicted values. This implies that Ge_{Zn} may not simply vary linearly with time on the overall reaction. Further investigation with more experimental data is required to elaborate their relationship.

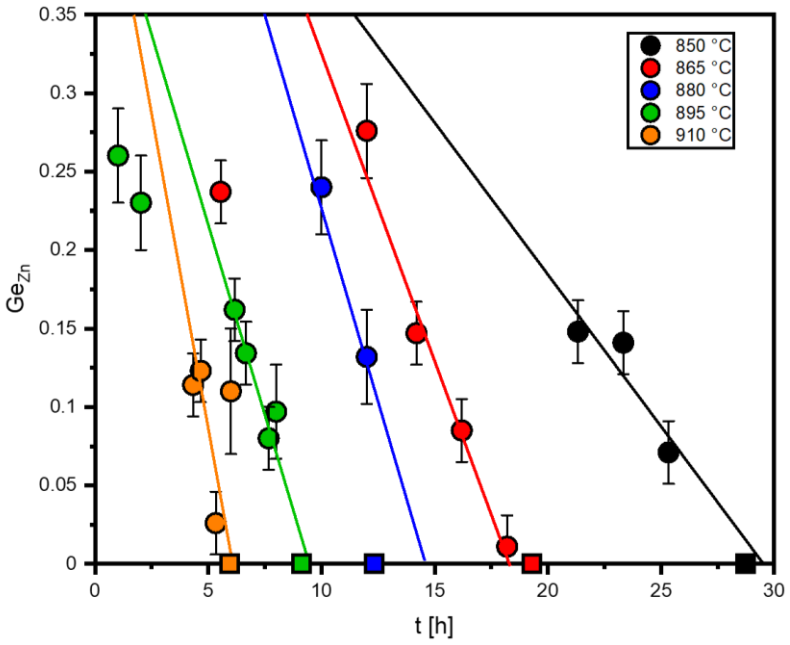

Figure 34 Plot of intrinsic disorder Ge_{Zn} as a function of synthesis conditions (dwelling time *t* and reaction temperature *T*). Lines in colours represent the linear fit of plots. The colourful square symbols represent the conditions for $ZnGeN_2$ predicted by *x*/*t* linear fit in Figure 21.

Furthermore, as the higher reaction temperature is applied for the synthesis, a more rapid decrease of intrinsic cation disorder with time is observed. Since intrinsic cationic disorder has been distinguished by definition from the chemical composition-related extrinsic disorder, it is reasonable to believe that the decease rate of intrinsic disorder with temperature is due to a mechanism independent of the composition, hence independent of the chemical reaction. Instead, this mechanism is likely to be a temperature-dependent mechanism, probably the Zn-Ge exchange. Applying the Arrhenius equation[121-123] (Section 3.2.4, Formula 3.17, reproduced below),

$$\ln k = -\frac{E_a}{R} \cdot \frac{1}{T}$$

and setting the slope of fit lines as the reaction rate factor (*k*), one obtains the linear relationship (Figure 35). The activation energy of the Zn-Ge exchange on the two cation

sites is c.a 230(46) kJ/mol, slightly smaller than the activation energy of subreaction Zn-displacement of 290(21) kJ/mol (Section 3.2.4). Still, the difference between them is largely within calculation error.

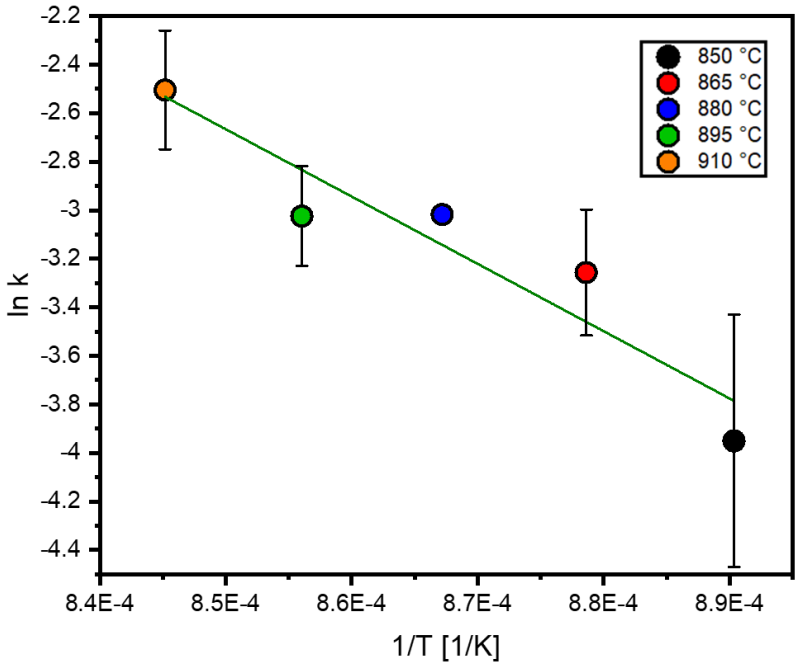

Figure 35 Plot of parameter k in the fit formula as a function of reaction temperature. The cyan line signifies the linear fit using the Arrhenius equation.

The relationship of $Zn_e = f(\alpha)$ (Figure 36a) is similar to the relationship of $x = f(\alpha)$ (Figure 28). This is rationale since Zn_e correlates directly with chemical composition as mentioned (Figure 32).

When plotting the intrinsic disorder Ge_{Zn} as a function of structure distortion factor α, most data points are distributed around a straight line (Figure 36b). This line crosses through the point (0.02, 0) corresponding to values of the full ordered β-$NaFeO_2$-type $ZnGeN_2$ based on DFT. In addition, this line reaches the point (0, 0.28), suggesting the intrinsic cation disorder in the wurtzite-type $Zn_{1+x}Ge_{1-x}(O_xN_{1-x})_2$ is c.a. 0.28, largely in line with the predicted value of 1/3 for the oxygen-richest $Zn_{1+x}Ge_{1-x}(O_xN_{1-x})_2$ ($x \approx 1/3$) according to $Ge_{Zn} = (1-x)/2$ (Formula 3.27). This finding suggests an increase in cation disorder with larger oxygen content, which is in accordance with the phenomenon observed by the crystal structure transformation (Section 3.3.1) that the oxygen-richest $Zn_{1+x}Ge_{1-x}(O_xN_{1-x})_2$ crystallise into the wurtzite-type structure, which should be disordered.

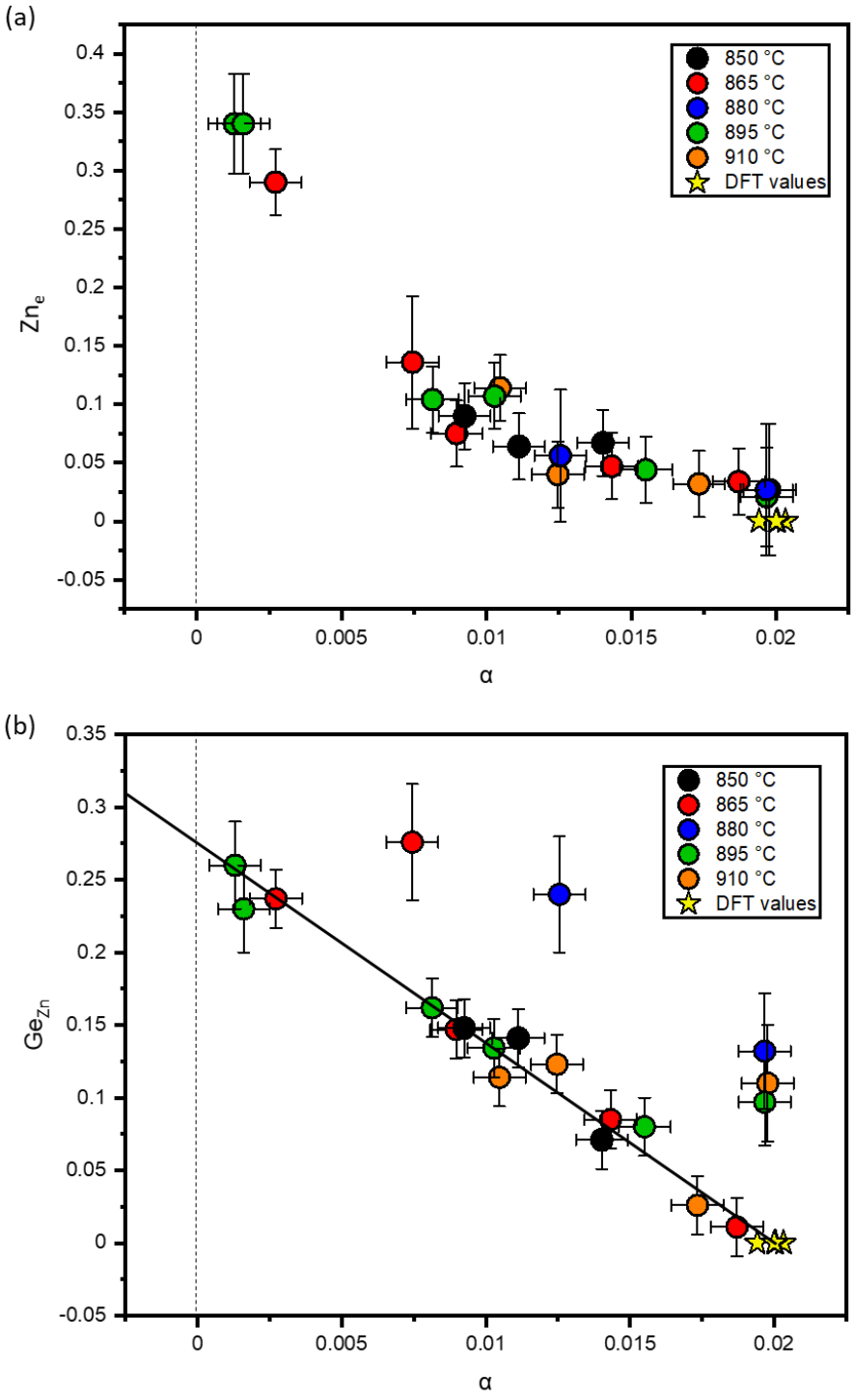

Figure 36 Plot of extrinsic cation disorder as a function of structure disorder parameter α (a); Plot of extrinsic cation disorder (experimental values: circular; DFT values[44, 54, 65]: stars) as a function of structure disorder parameter α. The black line represents a linear trendline (b).

3.5 Bandgap energy tuning of the $Zn_{1+x}Ge_{1-x}(O_xN_{1-x})_2$ system

The bandgap energy (E_g) is an essential property for semiconductors. For solar cell applications, the theoretical conversion efficiency can be discussed as a function of the bandgap energy.[19] Therefore, tunable bandgap energy is an attractive characteristic for a promising candidate for solar cell material.

This section discusses the bandgap energy tuning mechanisms of $Zn_{1+x}Ge_{1-x}(O_xN_{1-x})_2$ system based on the composition and cation disorder and attempts to answer the question of how to achieve precise control of the bandgap energy by experimental means and what are the major factors determining the bandgap energy of this material.

3.5.1 Bandgap energy control by reaction conditions

Figure 37 shows the optical bandgap energy (E_g) for different temperature series of samples *versus* dwelling time *t*. A clear trend is observed between the bandgap energy and the dwelling time *t* for a temperature series. The bandgap energy tends to increase with rising *t*. In addition, the rate of increase of the bandgap energy rises significantly as the temperature of the reaction used for synthesis increases, which is exhibited by the change of the slops of interpolation lines. Furthermore, the increase of bandgap energy is not linear over the dwelling time range for a temperature series. The bandgap first increases slowly between 2.7 eV and 2.8 eV before entering a phase of significant increase. The rising trend slows down significantly when the bandgap energy reaches 3.4 eV. This could be rationalised that the reaction has proceeded to the end and the chemical composition is close to $ZnGeN_2$. Continuing to increase the reaction time does not result in a significant change in the chemical composition of compounds. This is, of course, based on the assumption that there is a necessary correlation between bandgap energy and chemical composition. Nonetheless, by varying the *T*-*t* combination, it is possible to achieve a straightforward control of the bandgap energy of samples.

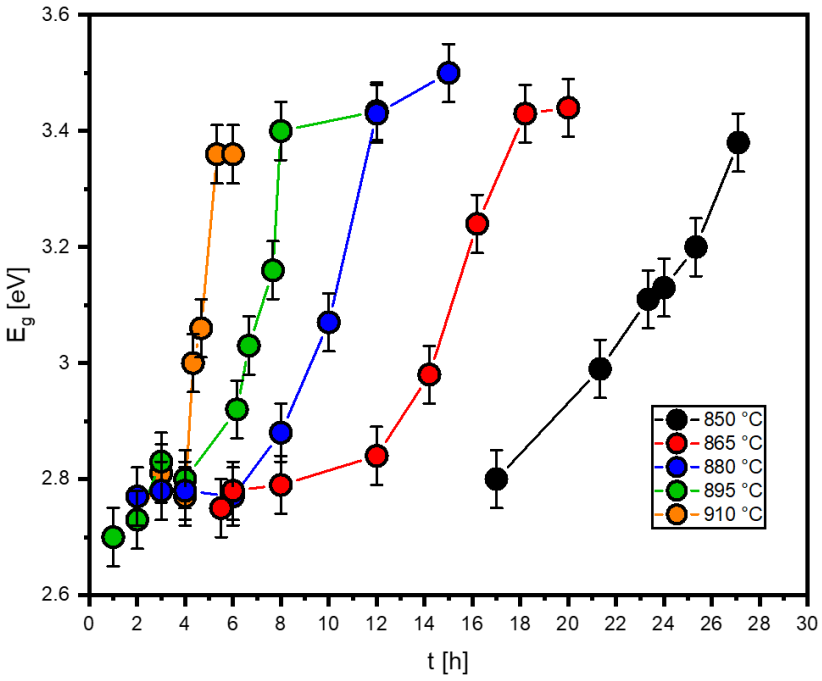

Figure 37 Plots of the optical bandgap energy (E_g) of samples as a function of the reaction conditions (t, T). Samples prepared by different reaction temperatures are in different colours.

3.5.2 Bandgap energy tuning through structural distortion

A clear trend can be observed between the crystal structure, represented by the crystal structural distortion parameter (α) (Section 3.3.2), and the optical bandgap energy (E_g) (Figure 38). The relationship between factor α and bandgap energy is largely linear in the range of $0.005 < x < 0.02$. However, over the entire range of x (considering the range $x < 0.005$), they exhibit a non-linear relationship.

Based on the definition of factor α, the value of $\alpha = 0$ is for the wurtzite-type and $\alpha = 0.023$ for the β-$NaFeO_2$-type $Zn_{1+x}Ge_{1-x}(O_xN_{1-x})_2$. The bandgap energy varies with crystal structure transformation from 2.7 eV to 3.5 eV. While the wurtzite-type $Zn_{1+x}Ge_{1-x}(O_xN_{1-x})_2$ show similar bandgap energy of about 2.7 eV - 2.8 eV, β-$NaFeO_2$-type $Zn_{1+x}Ge_{1-x}(O_xN_{1-x})_2$ samples with the largest distortion factor shows bandgap energy of about 3.54(5) eV, in line with the DFT values of 3.65 eV.[65] This finding suggests that the transformation of the crystal structure from wurtzite-type to β-$NaFeO_2$-type triggers an increase in the bandgap energy. By the intuitive trend of the data, we can empirically surmise that perfectly ordered $Zn_{1+x}Ge_{1-x}(O_xN_{1-x})_2$, which

should be with α ≈ 0.02 based on DFT, should have optical bandgap energy of about 3.4 eV and perfectly disordered $Zn_{1+x}Ge_{1-x}(O_xN_{1-x})_2$ should be about 2.7 eV.

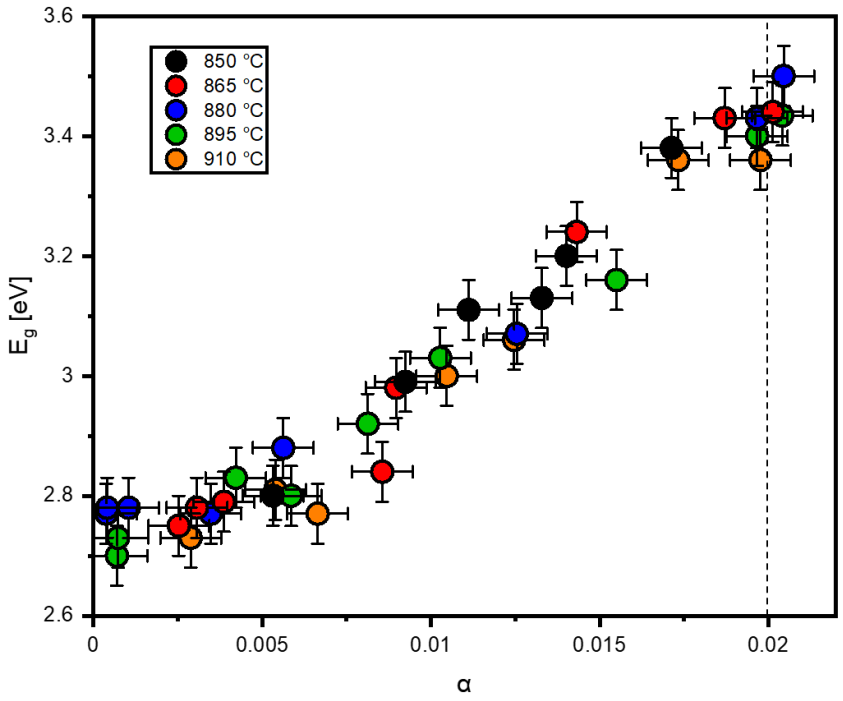

Figure 38 Plots of the optical bandgap energy (E_g) of samples as a function of the structural distortion parameter *α*. Samples prepared by different reaction temperatures are in different colours.

3.5.3 Bandgap energy tuning through chemical composition and extrinsic cation disorder

When plotting the optical bandgap energy (E_g) as a function of the chemical composition (represented by *x*), one observes a non-linear relationship between them (Figure 39). Given the relationship between chemical composition and extrinsic cation disorder Zn_e (Figure 32), Figure 39 can be seen as an E_g - Zn_{Ge}^* description.

The decrease of bandgap with oxygen content (represented by O/N ratio) was reported by other recent studies focussing on $Zn_{1+x}Ge_{1-x}(N_{1-x}O_x)_2$ thin films and nanoparticles.[81, 133] The narrowing of the bandgap can be explained by the upward shift of the valence band maximum induced the *p-d* repulsion between Zn 3*d* and N 2*p* + O 2*p* orbitals.[48, 133, 134]

In some literature, $Zn_{1+x}IV_{1-x}(O_xN_{1-x})_2$ (IV: Ge, Sn) was reported as an alloy system between ternary nitride and ZnO.[7, 81, 88, 89, 92, 136] Thus, we applied a fit by using Vegard's law, taking into account the bowing effect according to the hypothesis of the alloy system of $ZnGeN_2$ and ZnO, which could be expressed as a linear combination of the form (Section 3.2.3, Formula 3.10, reproduced here):

$$k\ \mathrm{ZnGeN_2} + (1-k)\mathrm{ZnO}$$

Therefore, the bandgap energy can be expressed using a proposed formula to reflect the bowing effect:

$$E_g^{ZnGeON} = kE_g^{ZnGeN_2} + (1-k)E_g^{ZnO} + bk(1-k) \qquad 3.40$$

where b is the bowing coefficient, E_g^{ZnO} is the bandgap energy of ZnO with E_g^{ZnO} = 3.22 eV, reported by Makula et al..[135] E_g^{ZnGeN2} represents the bandgap value of $ZnGeN_2$.

The value of k directly reflects the chemical composition (discussed in section 3.2.3), can be correlated to the cation ratio with k = Ge/Zn (Section 3.2.3, Formula 3.14); hence can be expressed as a function of x according to chemical formula $Zn_{1+x}Ge_{1-x}(O_xN_{1-x})_2$:

$$k = \frac{1-x}{1+x} \qquad 3.41$$

Performing the bowing model, one obtains a non-linear fit with a bowing coefficient of b = 2.8(1) eV (Figure 39 orange curve). The bandgap value of $ZnGeN_2$ (x = 0) was predicted to be 3.45 eV, largely in line with reported values in the range from 3.3 to 3.65 eV. [44, 45, 53, 54, 65] The bandgap energy for the oxygen-richest $Zn_{1+x}Ge_{1-x}(O_xN_{1-x})_2$ (x = 1/3) is predicted to be 2.72 eV.

However, the experimental data did not match the bowing curve perfectly with $R^2 \approx 0.89$. The experimental data showed systematic differences below predicted values in the range of $0.05 < x < 0.15$, although the differences are largely within the calculation errors. This finding implies that the material system follows a more complex bandgap tuning mechanism, although compositionally similar to an alloy system.

In addition, a non-linear fit with exponential decay matches well the experimental data (Figure 39 green curve). The fit exhibits an estimated bandgap of ≈ 3.67 eV for x = 0, reflecting the $ZnGeN_2$, perfectly matching the postulated value of 3.65 eV by DFT.[65] In addition, the oxygen-richest $Zn_{1+x}Ge_{1-x}(O_xN_{1-x})_2$ ($x \approx 1/3$) show very similar optical bandgaps in a range between 2.7 eV and 2.8 eV.

It is worth noting that the exponential decay mechanism remains unclear. A possible reason might be that this bandgap variation is likely to be affected by mechanisms such as alloying and cation disorder at the same time, thus exhibiting an exponential decay-like profile.

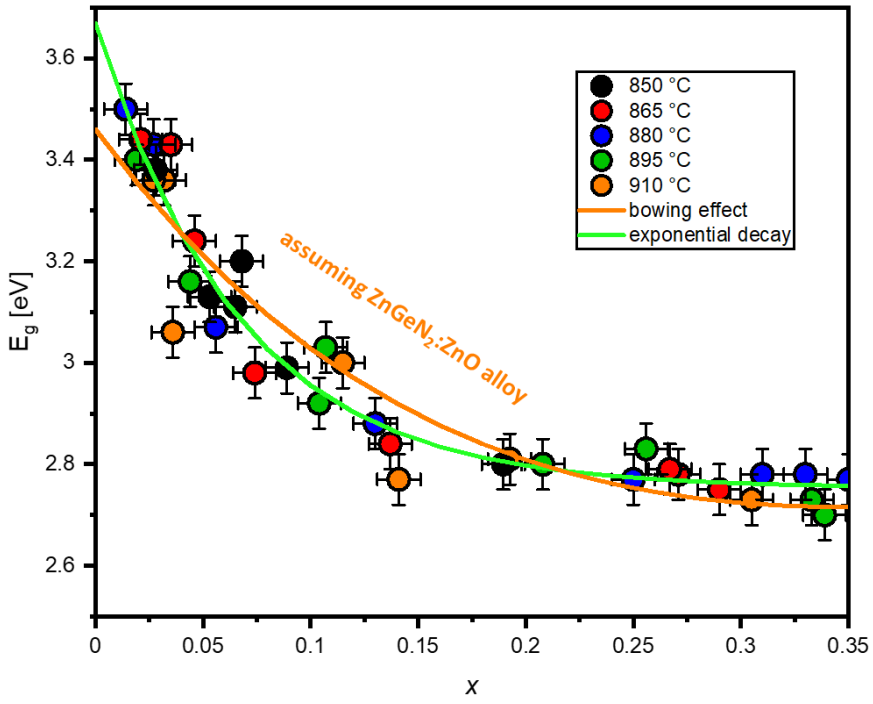

Figure 39 Plots of the optical bandgap energy (E_g) of samples as a function of the oxygen content / extrinsic cation disorder Zn_e. Samples prepared by different reaction temperatures are in different colours. The green line represents the fit according to the exponential decay function that $f(x) = y^0 + A \cdot \exp(-x/B)$. The red dash line represents the fitting considering the bowing effect of a $ZnGeN_2$:ZnO alloy.

3.5.4 Bandgap energy tuning through intrinsic cation disorder

Figure 40 shows the relationship between the intrinsic cation disorder represented by Ge_{Zn} and the optical bandgap. Most data points are distributed around a straight line, although some data points show a significant distance from the trendline due to experimental errors.

As more intrinsic cation disorder in the crystal structure, the $Zn_{1+x}Ge_{1-x}(O_xN_{1-x})_2$ shows smaller bandgap energy. The bandgap energy narrowing with the intrinsic cation

disorder is probably due to a lowered conduct band minimum (CBM) related to Ge_{Zn} and a defect band close to valence band maximum (VBM) caused by Zn_{Ge}.[75, 128]

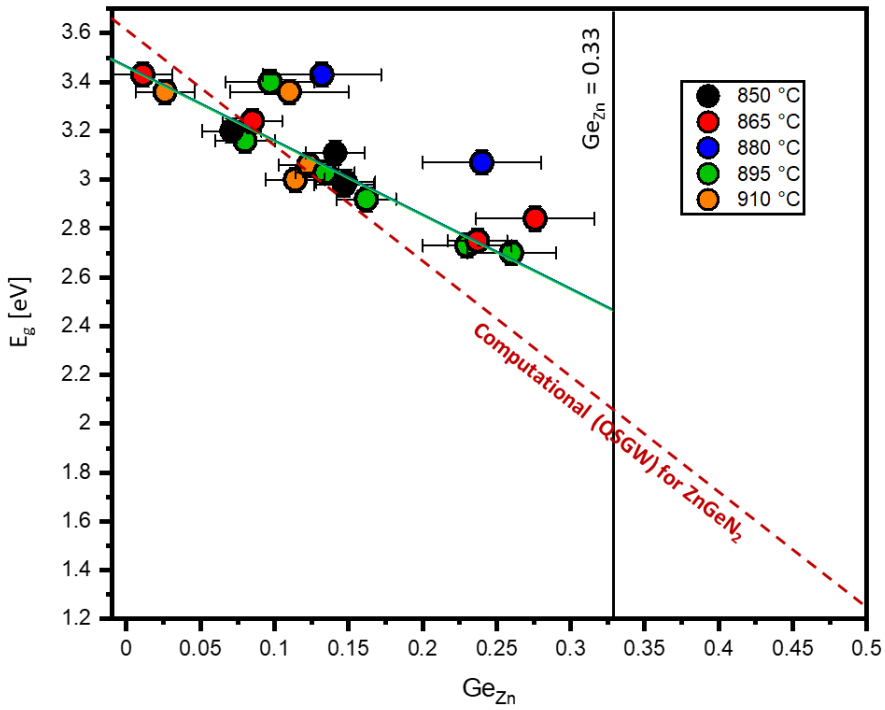

Figure 40 Plots of the optical bandgap as a function of intrinsic cation disorder Ge_{Zn} that was obtained by simultaneous refinement. Samples prepared by different reaction temperatures are in different colours. The linear trendline of experimental values for $Zn_{1+x}Ge_{1-x}(O_xN_{1-x})_2$ (green line) and computational trendline for $ZnGeN_2$ (dark red dash line)[65] are shown.

According to the trendline, one can estimate the optical bandgap of the fully ordered $Zn_{1+x}Ge_{1-x}(O_xN_{1-x})_2$ ($E_g \approx 3.48$ eV) through its intersection with $Ge_{Zn} = 0$ and the optical bandgap energy of a fully disordered oxygen-richest $Zn_{1+x}Ge_{1-x}(O_xN_{1-x})_2$ ($E_g \approx 2.46$ eV) with $Ge_{Zn} = 1/3$. These estimated values are largely in line with the prediction in Section 3.5.2 and Section 3.5.3, indicative of the reliability of $E_g = f(Ge_{Zn})$ evaluation.

Moreover, when one linearly connects the computational band gap values of the two limit states of $ZnGeN_2$[65] (fully ordered states: $Ge_{Zn} = 0$; fully disordered states: $Ge_{Zn} = 0.5$) in the plot, one obtains a trend line (Figure 40 red dash line). This line is more skewed than that of the $Zn_{1+x}Ge_{1-x}(O_xN_{1-x})_2$. This difference is probably due to the oxygen content and that Zn/Ge ≠ 1 in the oxide nitrides.

3.6 Conclusions

Powder of zinc germanium oxide nitride was successfully synthesised by nitridation of Zn_2GeO_4 under NH_3. The synthesis window for phase-pure $Zn_{1+x}Ge_{1-x}(O_xN_{1-x})_2$ was found by varying the dwelling time and reaction temperature. Ensuring that the sample is at the proper ammonia flux throughout the synthesis process, including the cooling stage, is the key to obtaining β-$NaFeO_2$-type $Zn_{1+x}Ge_{1-x}(O_xN_{1-x})_2$.

Through a comprehensive study on the chemical composition of $Zn_{1+x}Ge_{1-x}(O_xN_{1-x})_2$, the overall reaction mechanism of the nitridation of $ZnGeO_4$ was established. The reaction is formally divided into two reaction steps: nitrogen is first introduced into the material before the Zn-extraction. While the first step reacts at an early stage, the latter stage predominates the chemical composition. This finding provides insight into the reaction mechanism and allows a compositional control of the materials, hence a more targeted synthesis.

In addition, experimental evidence of the crystal structure transformation with chemical composition is observed that oxygen-rich $Zn_{1+x}Ge_{1-x}(O_xN_{1-x})_2$ adopt the wurtzite-type and oxygen-poor $Zn_{1+x}Ge_{1-x}(O_xN_{1-x})_2$ show the β-$NaFeO_2$-type structure. For samples in the transition state, even those in the oxygen-rich region, significantly asymmetric peaks are present in XRD pattern of $Zn_{1+x}Ge_{1-x}(O_xN_{1-x})_2$ as evidence of peak splitting to support the argument that these samples adopt the orthorhombic crystal structure rather than the wurtzite-type. The β-$NaFeO_2$-type structure was used to evaluate the lattice constants in order to investigate this crystal structural transformation. While lattice constant a and b vary evidently over the composition range, c is largely unaffected. Furthermore, an abrupt change of b was observed at the composition with $x \approx 0.07$. Moreover, a distortion factor α was established to quantify the stage of the crystal structure transformation. The investigation based on $\alpha = f(x)$ reveals two distinct stages of structural transformation, more rapid structural transformation in the composition range of $0 < x < 0.07$ than the range of $0.07 < x < 0.33$.

Simultaneous refinement of neutron and XRD data was performed to investigate the cation distribution in the crystal structure to understand the cation disorder effect in $Zn_{1+x}Ge_{1-x}(O_xN_{1-x})_2$. The long-range cation disorder is studied by using the SOF of the cations in different crystallographic sites of $Zn_{1+x}Ge_{1-x}(O_xN_{1-x})_2$. While the extrinsic

cation disorder is strictly related to oxygen content, the intrinsic cation disorder induced by cation exchange is largely independent of oxygen content.

Furthermore, a simple linear relationship between intrinsic cation disorder and reaction time and the resulting inferred reaction conditions for a fully ordered sample match empirical expectations. The validity of this linear relationship for samples at the beginning of the reaction needs further investigation. Nevertheless, it is possible to engineer the intrinsic disorder in this by reaction conditions. In addition, the intrinsic cation disorder shows a linear correlation with the structure distortion factor α.

Given this experimental evidence and the anticipated importance of the cation ordering in this class of material, the investigation of the relationship among the composition, crystal structure and cation disorder effect of this material was performed based on the targeted synthesis.

The optical bandgap energy of $Zn_{1+x}Ge_{1-x}(O_xN_{1-x})_2$ can be controlled by varying reaction conditions. The bandgap energy varies from 2.7 eV to 3.4 eV as the crystal structure transforms from the wurtzite-type structure to the β-$NaFeO_2$-type structure.

While the $E_g = f(x)$ plots over the composition range can be fitted using Vegard's law with the bowing effect based on the assumed $ZnGeN_2$:ZnO alloy ($R^2 = 0.89$), systematic errors between plots and fit curve could be observed. Therefore, a complex combination of different mechanisms may dominate $E_g = f(x)$. This theoretical model of bandgap affected by composition involving additional disorder effects needs to be further explored. Furthermore, the linear relationship of optical bandgap energy over intrinsic cation disorder is observed in this work. The bandgap energy of the inferred fully ordered samples are in agreement with the values calculated by DFT.

It is important to put these results in the perspective of the overall bandgap energy trend among these mechanisms: the oxygen-rich samples in the disordered wurtzite-type structure tends to have a narrower bandgap than the oxygen-poor samples in the ordered β-$NaFeO_2$-type. With the bandgap in the range of 2.7 eV to 3.4 eV, $Zn_{1+x}Ge_{1-x}(O_xN_{1-x})_2$ may not be a promising candidate for solar cells.

Nevertheless, the study of the $Zn_{1+x}Ge_{1-x}(O_xN_{1-x})_2$ system provides a potent exemplary model for understanding disorder effects in Zn–IV–N_2 (IV: Ge, Sn) materials.

Chapter IV

Study of zinc tin oxide nitride

As discussed in section 1.3.1, the synthesis of $ZnSnN_2$ material is challenging, particularly the bulk materials, which hampers the fundamental study of this material. Therefore, the synthesis of bulk $ZnSnN_2$ must precede the further experimental investigation of crystal structure based on high-resolution diffraction data.

This chapter introduces a new synthetic method of Zn-Sn-O-N powder to fulfil the preparative basis of experimental studies. The samples prepared by this method have high crystallinity; hence diffraction patterns with well-defined reflections are possible. In addition, the analysis of the crystal structure of these samples was performed based on XRD, attempting to figure out which structural type these compounds adopt. Finally, combining UV-Vis and chemical analysis, we hope to answer the question of how the bandgap energy is tunable with the chemical composition.

4.1 A new method to synthesise bulk zinc tin oxide nitride

Zinc tin oxide nitride in the form of a well-crystallised powder was achieved through a solid-state reaction route. Binary nitrides Zn_3N_2 and Sn_3N_4 were used as precursors to allow a straightforward reaction. The following sections introduce the preparation of binary nitrides before discussing the solid-state reaction route towards Zn-Sn-O-Ns.

4.1.1 Preparation of binary nitride precursors

Synthesis of Zn_3N_2 powder

Zn_3N_2 powder was prepared by nitridation of metallic Zn under ammonia with the reaction:[136]

$$3\,Zn + 2\,NH_3 \xrightarrow{\Delta} Zn_3N_2 + 3\,H_2\uparrow \qquad 4.1$$

A schematic illustration of the synthesis experiment is shown below (Figure 41).

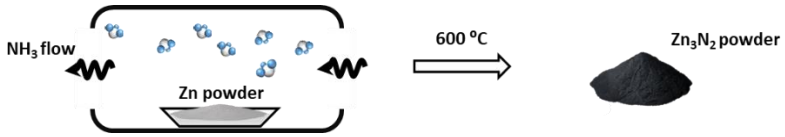

Figure 41 Schematic illustration of the synthesis of Zn_3N_2 powder.

In this work, 2g of metallic zinc powder (Zinc dust, < 10 µm, ≥ 98 %, Aldrich) were reacted in a silica glass reaction tube with 4.5 cm diameter. The powder was treated under a nitrogen flow of 1.5 l/min until the reaction temperature of 600 °C is reached. Then, the nitridation stage is performed under an ammonia flow of 0.1 l/min for 6 hours. Finally, the sample cools down naturally under an ammonia atmosphere. It is worth noting that the Zn_3N_2 precursor should be stored in an inert atmosphere since it will react with water vapour in air and eventually transform into zinc oxide.[116]

Synthesis of Sn_3N_4 powder

Sn_3N_4 powder was prepared using the two-step method reported by Qu et al..[137] Sn_3N_4 powder was obtained by nitridation of a viscous gel-like precursor (Figure 42).

First, the mixture of 1 g $SnCl_4 \cdot H_2O$ (extra pure, ≥ 98 %, Acros), 1 g Urea (ph. Eur, ≥ 99.5 %, Carl Roth) and 2 ml ethanol was first stirred for 30 min to obtain a transparent viscous solution. After that, the solution was aged overnight and annealed at 510 °C for 4 h under 0.1 l/min ammonia flow. The heating rate was set to 250 K/h to avoid boiling the viscous solution. After the reaction, the sample cools down naturally under ammonia.[137]

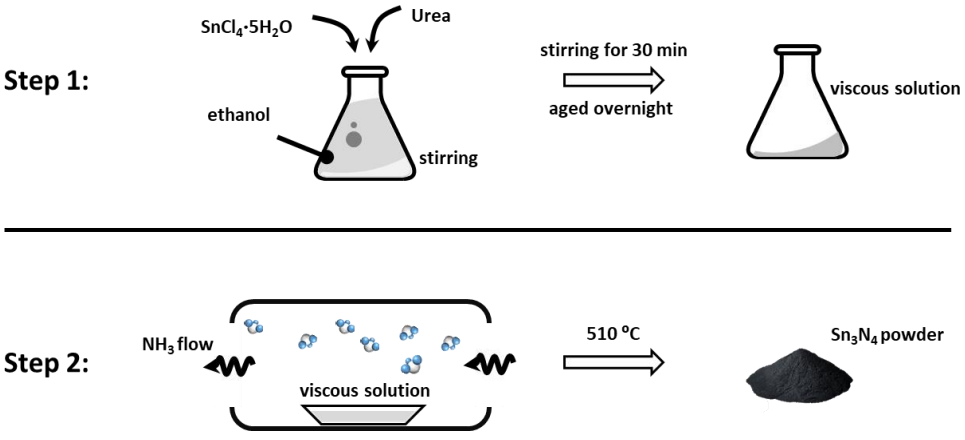

Figure 42 Schematic illustration of the synthesis of Sn_3N_4 powder.

XRD experiment shows that Zn_3N_2 powder and Sn_3N_4 prepared in this work are well-crystallised and exhibit phase purity (Figure 43), which is advantageous for further use as precursors for synthesising zinc tin oxide nitrides.

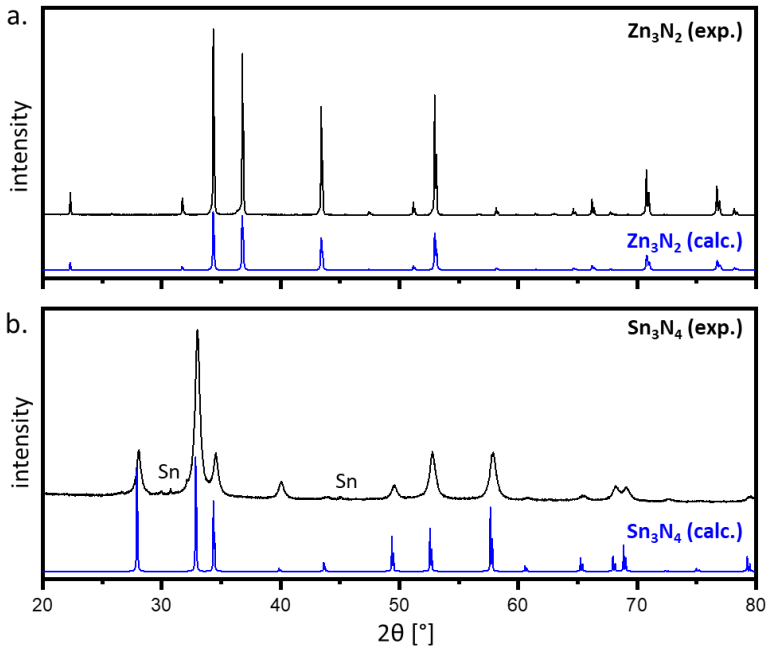

Figure 43 Experimental XRD pattern of Zn_3N_2 precursors prepared by nitridation under NH_3 at 600 °C for 6 hours (a, black line) and calculated XRD pattern of Zn_3N_2 (a, blue line). Experimental XRD pattern of Sn_3N_4 precursors prepared by nitridation under NH_3 at 510 °C for 4 hours (b, black line) and calculated XRD pattern of Sn_3N_4 (b, blue line).

A negligible Sn side phase was found in Sn_3N_4 samples. It is worth noting that the crucibles used for the preparation of Sn_3N_4 are lightly stained black. These black stains cannot be dissolved by aqua regia; instead can be completely removed by heating in air at high temperatures. In the experiments, we removed the stains by heating the stained crucibles in a muffle furnace to 1100°C and holding them there for several hours. Considering that organic components (urea) were used for preparing Sn_3N_4, it is likely that these black stains are carbon black.

4.1.2 Preparation of the Zn-Sn-O-N

Zn-Sn-O-N powder was prepared by a solid-state approach using the Zn_3N_2 and Sn_3N_4 precursors. The proposed reaction is:

$$Zn_3N_2 + Sn_3N_4 \xrightarrow{\Delta} 3\ ZnSnN_2 \qquad 4.2$$

It is worth noting that while the targeted product should be $ZnSnN_2$ according to the mentioned reaction formula, avoiding oxygen impurities in the product was challenging. Therefore, Zn-Sn-O-N powder was obtained with this method (Figure 44).

Herein, Zn_3N_2 and Sn_3N_4 powder were mixed with a molar ratio of 1:1. The mixture of binary nitrides was pressed in pellets and then annealed for 4 hours at 500 °C- 650 °C with 0.1 l/min ammonia flow. Both the heating and cooling processes are carried out under an ammonia atmosphere. Next, the as-annealed products were washed with 0.06 mol/l hydrochloric acid to remove oxide side products and the Zn_3N_2 reactant. After thorough stirring, the suspension was filtered and washed with deionised water. Finally, the filtered mud is placed in the air and dried overnight to obtain powders in black as the products.

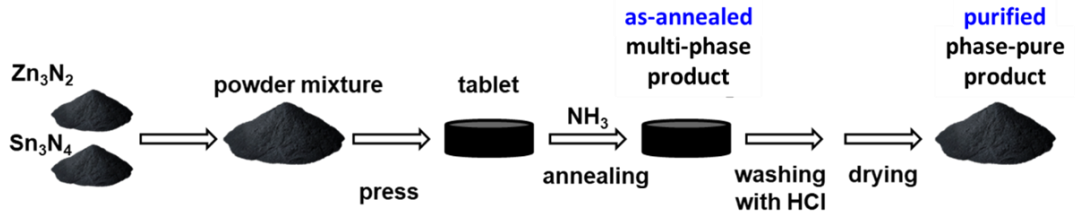

Figure 44 Schematic illustration of the synthesis of Zn-Sn-O-N powder using Zn_3N_2 and Sn_3N_4 precursors.

It is noteworthy that Sn remains visible at the bottom of the suspension after stirring for more than one hour, indicating that Sn is barely soluble in the hydrochloric acid solution at the concentration explored here. Therefore, it is important to avoid using the bottom suspension for filtering to prevent the presence of Sn in the filtered sample. The as-purified sample is largely phase-pure and exhibits the XRD profile in line with the calculated pattern of $ZnSnN_2$ (Figure 45), which is based on the assumption of the wurtzite-type structure. Thus, the purification step (washing and drying) allows us to obtain phase-pure samples containing the targeted nitride phase and further investigate these materials based on phase pure specimens.

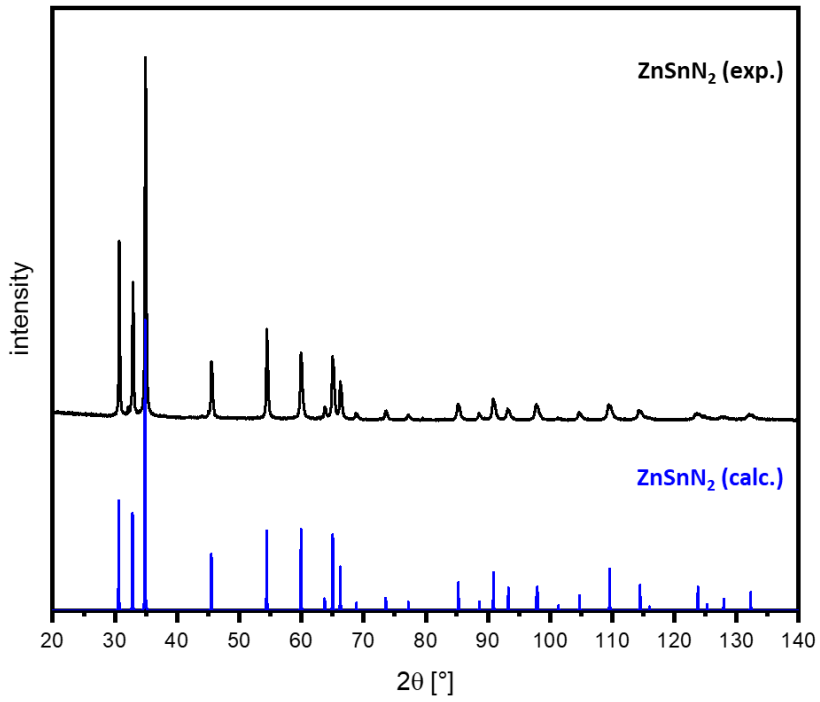

Figure 45 Measured XRD pattern of the as-purified sample synthesised at 560 °C for 4 hours (black) and the calculated XRD pattern of a wurtzite-type $ZnSnN_2$ (blue).

4.1.3 Phases in the as-annealed products

While one expects the phase pure samples according to the proposed reaction: $Zn_3N_2 + Sn_3N_4 \rightarrow 3\ ZnSnN_2$, the as-annealed samples, which are at the intermediate step of the synthesis, are not phase-pure; instead, they contain reactants such as Zn_3N_2 or Sn_3N_4 and the side phase Sn, which is probably due to the decomposition of Sn_3N_4 during the synthesis.

In order to optimise the synthesis method to improve the yield of Zn-Sn-O-N, the phase weight fractions of the as-annealed samples are calculated by multi-phase Rietveld refinement of XRD patterns (Figure 46 and Appendix).

It should be noted that the precise chemical composition and the crystal structure of the targeted nitride phases were not known as a *prior* since the chemical and structural analysis is challenging from the multi-phase powder samples. Thus, to understand the phases in the sample, one can use the wurtzite-type $ZnSnN_2$ model to mimic the targeted phase in the sample, simplify the calculation and focus on the share of phases to gain

an insight into the synthesis method. The refinement was performed by assuming the targeted nitride phase is pure $ZnSnN_2$ in a wurtzite-type structure to facilitate calculation.

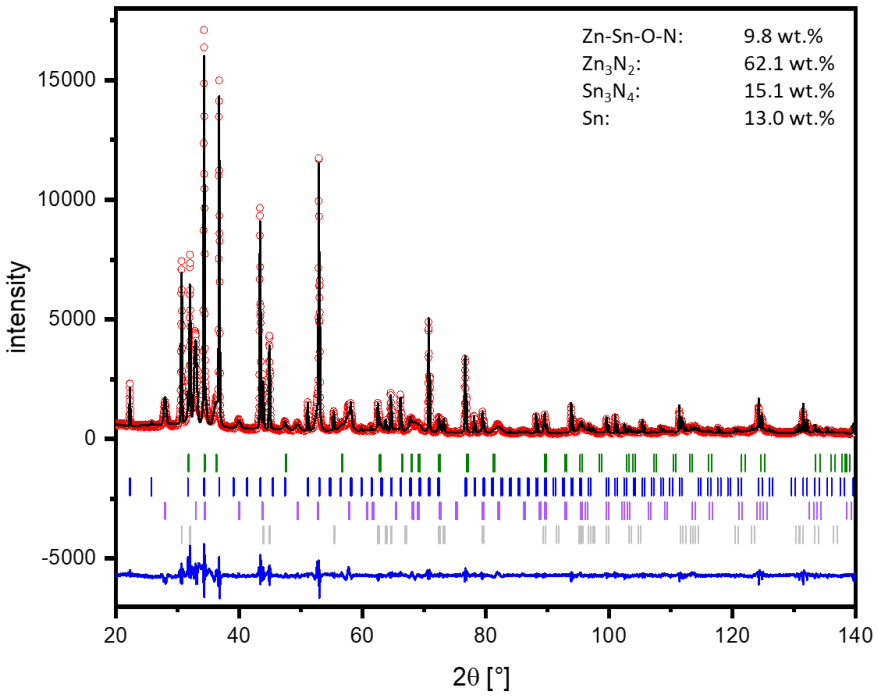

Figure 46 Powder XRD profile multi-phase refinement using the Rietveld method for the sample prepared at 500 °C - 10 h: measured intensities (red circles), calculated profile (black line), difference between measured and calculated intensities (blue line) and calculated reflection positions of wurtzite-type Zn-Sn-O-N phase (oliver ticks), Zn_3N_2 phase (blue ticks), Sn_3N_4 phase (lavender ticks) and Sn phase (grey ticks).

The calculated weight fraction of phases in as-annealed products are shown as Pie charts by combining the synthesis conditions (Figure 47). It is evident that the synthesis conditions significantly affect the share of phases. A combination of "low *T* – long *t*" is not advantageous for obtaining the targeted nitride phases due to the large fraction of side phases in the samples, such that over 90 wt. % side phases apart from the targeted "$ZnSnN_2$" phase in the sample prepared at 500 °C for 10 hours.

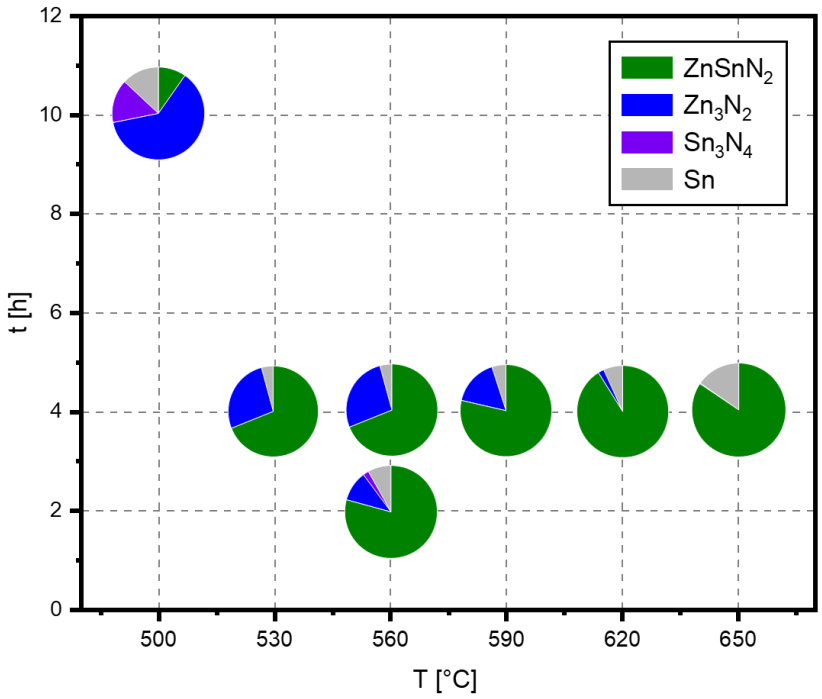

Figure 47 Position of the pie diagrams represents the synthesis conditions (*t*, *T*). The pie diagrams show the weight fraction of phases in the as-annealed samples.

From a general view, it should be noted that an increase in reaction temperature accelerates the chemical reactions, including the synthesis of the targeted Zn-Sn-O-N phase and the Sn-related side reactions.

When assuming the anticipated activation energies between these two reactions are different, the reaction rate (k) of the reactions should change differently with temperature since:

$$\frac{\partial k}{\partial T} = f(E_a) \qquad 4.3$$

Thus, adjusting the reaction conditions, including reaction temperature and time, allows for optimising the syntheses.

According to the quantified study of phase share and reaction conditions, the "high *T* - short *t*" strategy significantly allows us to obtain as-annealed samples with the weight fraction of the Zn-Sn-O-N phase over 70 wt.%. Increasing the reaction temperature might be a solution to promote the main reaction for gaining the targeted Zn-Sn-O-N phase. Reducing the reaction time aids in hampering the appearance of Sn.

For the time series (t = 4), increasing the reaction temperature reduces the share of the residual binary nitrides significantly while slightly increasing the amount of the Sn in the as-annealed samples. As a result, one can obtain the sample with the highest fraction of the targeted phase using the reaction temperature of 620 °C. We did not pursue the synthesis in the higher reaction temperature over 650 °C, as the share of the side phase, Sn, starts to increase significantly from here onwards, implying that either Sn_3N_4 had decomposed rapidly before conversion to targeted Zn-Sn-O-N phase or that the targeted phase was no longer stable at that temperature. Neither of these is what one would desire and is not conducive to improving the yield of the $ZnSnN_2$ phase.

4.1.4 Chemical composition of the Zn-Sn-O-N

As mentioned in 4.1.2, phase-pure Zn-Sn-O-N powder can be obtained by applying a purification step. These phase-pure Zn-Sn-O-N allow determining the chemical composition through the XRF method. Understanding the chemical composition of these compounds allow us to conclude the optimisation strategy for the synthesis method. Further, the chemical analysis facilitates understanding the relationship between chemical composition on crystal structure or material properties.

Herein, the Zn/Sn ratio was determined by XRF. All samples prepared using this method are off-stochiometric with Zn/Sn > 1. The Zn-Sn-O-N material systems can be seen here as a derivative by replacing Ge^{4+} in the Zn-Ge-O-N with Sn^{4+}, as they are both derived from the Zn-IV-N_2 (IV: Ge, Sn) material family. This naturally raises the expectation that the Zn-Sn-O-N material system would have similar chemical expressions and structural properties to the Zn-Ge-O-N material system. Therefore, according to the discussion of the chemical composition of the Zn-Ge-O-N material system in section 3.2.3 and Hamilton et al.[138], the chemical composition of Zn-Sn-O-N could be assumed to be in the formula of $Zn_{1+x}Sn_{1-x}(O_xN_{1-x})_2$.

It is important to note that trace amounts of Sn (< 1 wt.%) may remain in the purified sample (not all samples). For this, the relationship of the measured Zn/Sn ratio and the chemical composition (x) is:

$$\frac{Zn}{Sn} = \frac{(1+x)\cdot n(Zn_{1+x}Sn_{1-x}(O_xN_{1-x})_2)}{(1-x)\cdot n(Zn_{1+x}Sn_{1-x}(O_xN_{1-x})_2)+n(Sn)} \qquad 4.4$$

where the molar fraction $n(Zn_{1+x}Sn_{1-x}(O_xN_{1-x})_2)$ and $n(Sn)$ can be linked with their weight fraction obtained by Rietveld refinement of the XRD pattern (Figure 48), with:

$$\frac{n(Zn_{1+x}Sn_{1-x}(O_xN_{1-x})_2)}{n(Sn)} = \frac{w(Zn_{1+x}Sn_{1-x}(O_xN_{1-x})_2)}{w(Sn)} \cdot \frac{M(Sn)}{M(Zn_{1+x}Sn_{1-x}(O_xN_{1-x})_2)} \qquad 4.5$$

The molar mass $M(Zn_{1+x}Sn_{1-x}(O_xN_{1-x})_2)$ is approximated as $M(ZnSnN_2)$ = 212.1 g/mol to facilitate the calculation since x is not known as *prior*. The molar mass $M(Sn)$ = 118.71 g/mol.

Hence, the chemical composition (x) of the sample containing a small amount of Sn can be expressed by combining Formula 4.4 and 4.5 as:

$$x = \frac{0.56\times\left(\frac{Zn}{Sn}-1\right)\times\frac{w(Zn_{1+x}Sn_{1-x}(O_xN_{1-x})_2)}{w(Sn)}+\frac{Zn}{Sn}}{0.56\times\left(\frac{Zn}{Sn}+1\right)\times\frac{w(Zn_{1+x}Sn_{1-x}(O_xN_{1-x})_2)}{w(Sn)}} \qquad 4.6$$

For the sample prepared at 560 °C – 4 h with measured Zn/Sn = 1.30(5) and $w(Sn)$ = 0.62(4) wt.%, the calculated chemical composition x = 0.137(39) considering Sn impurity, largely in line with the composition x = 0.130(21) assuming a phase-pure sample. The differences in the results are within the calculation error. The chemical composition of the Zn-Sn-O-N calculated using the cation ratio Zn/Sn and $w(Sn)$ are listed in Table 4 in the form $Zn_{1+x}Sn_{1-x}(O_xN_{1-x})_2$.

Table 4 Experimentally determined Zn/Sn ratios of the $Zn_{1+x}Sn_{1-x}(O_xN_{1-x})_2$ using XRF method and chemical composition calculated according to $Zn_{1+x}Sn_{1-x}(O_xN_{1-x})_2$.

Sample	T [°C]	t [h]	Zn/Sn ratio (measured)	Sn trace [wt.%]	chemical composition in formula $Zn_{1+x}Sn_{1-x}(O_xN_{1-x})_2$
1	530	4	1.37(5)	-	$Zn_{1.16}Sn_{0.84}(O_{0.16}N_{1.84})_2$
2	560	2	1.47(3)	-	$Zn_{1.19}Sn_{0.81}(O_{0.19}N_{1.81})_2$
3	560	4	1.30(5)	0.62(4)	$Zn_{1.14}Sn_{0.86}(O_{0.14}N_{1.86})_2$
4	590	4	1.45(3)	0.07(5)	$Zn_{1.18}Sn_{0.82}(O_{0.18}N_{1.82})_2$
5	620	4	1.56(4)	0.27(4)	$Zn_{1.22}Sn_{0.78}(O_{0.22}N_{1.78})_2$
6	650	4	1.98(9)	0.11(4)	$Zn_{1.33}Sn_{0.67}(O_{0.33}N_{1.67})_2$

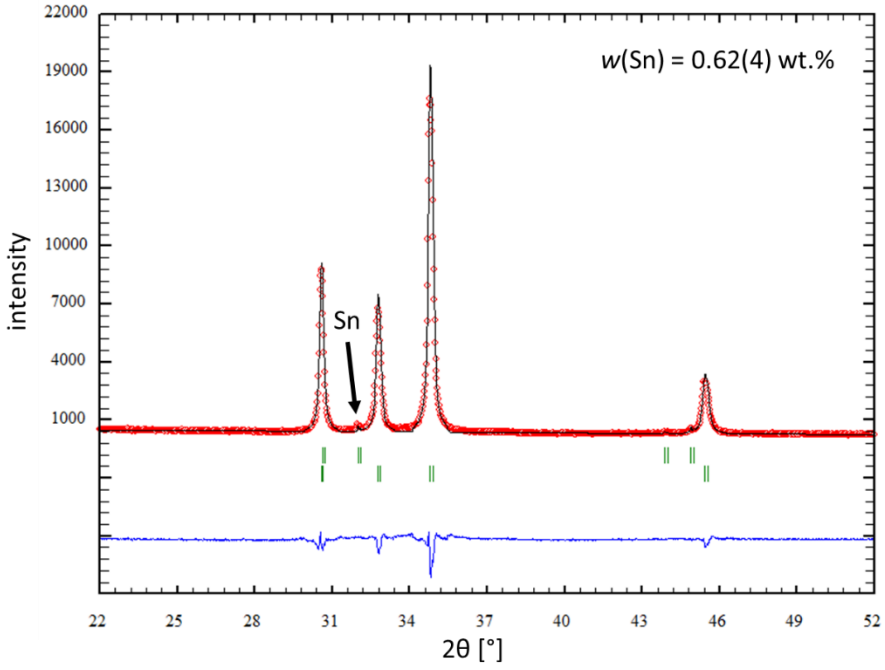

Figure 48 Powder XRD profile multi-phase refinement using the Rietveld method for the sample prepared at 560 °C - 4 h: measured intensities (red circles), calculated profile (black line), difference between measured and calculated intensities (blue line) and calculated reflection positions (green ticks, $Zn_{1+x}Sn_{1-x}(O_xN_{1-x})_2$ top, Sn bottom). Futher refinements are shown in Appendix.

When plotting the chemical composition (represented by x) as a function of the reaction temperature (Figure 49), one observes a general trend that increasing the reaction temperature leads to a higher amount of Zn and O in the sample. The sample prepared using the condition of 500 °C - 10 h is not involved in this figure since the phase fraction of $Zn_{1+x}Sn_{1-x}(O_xN_{1-x})_2$ was below 10 wt.% of the as-annealed product and collecting the $Zn_{1+x}Sn_{1-x}(O_xN_{1-x})_2$ powder from the filtration device was a challenge. It is clear that the chemical composition of the samples prepared in the present work varies in the range of $0.13(2) < x < 0.33(3)$, corresponding to the ratio of Zn/Sn between $1.30(5) <$ Zn/Sn $<1.98(9)$. The sample with the lowest Zn fraction and oxygen content was obtained at 560 °C for 4 hours, which is the most approximant prepared in this work towards pure $ZnSnN_2$. In addition, continuing to reduce the reaction time to 2 hours at the temperature of 560 °C would instead result in an oxygen and zinc enriched sample. The reduction in reaction time is justified since Sn_3N_4 as the reactant is depleted after 4 hours of reaction (Figure 47), thereby no significance to continue to increase the reaction time. Although we cannot ignore the differences in the chemical composition of the samples with $ZnSnN_2$, the composition range of these samples exhibits the potential of this synthetic method for the preparation of oxide nitride as $ZnSnN_2$

approximations, which allows further investigation on the crystal structure and other properties of these materials.

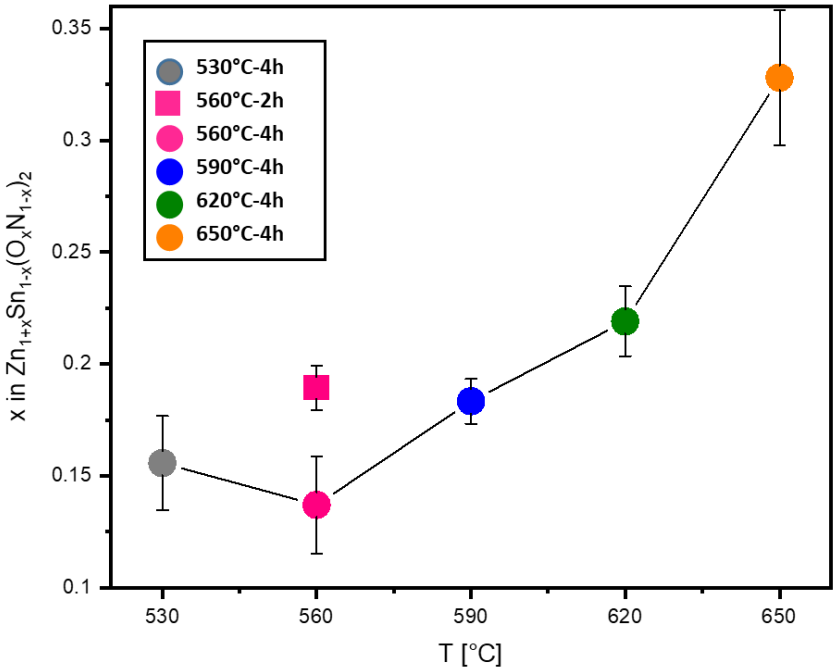

Figure 49 Plot of chemical composition (represented by *x*) as a function of the reaction temperature.

4.2 Crystal structure of the zinc tin oxide nitrides

4.2.1 Investigation of the crystal structure

As the exemplary study on $Zn_{1+x}Ge_{1-x}(O_xN_{1-x})_2$ discussed in Section 3.2.1, we expect a similar trend of crystal structure transformation in the $Zn_{1+x}Sn_{1-x}(O_xN_{1-x})_2$ since $Zn_{1+x}Ge_{1-x}(O_xN_{1-x})_2$ and $Zn_{1+x}Sn_{1-x}(O_xN_{1-x})_2$ are similar members of $Zn_{1+x}IV_{1-x}(O_xN_{1-x})_2$ (IV: Ge, Sn) family. The $Zn_{1+x}Sn_{1-x}(O_xN_{1-x})_2$ can be thought of as a compound by replacing Ge^{4+} with Sn^{4+} in the former.

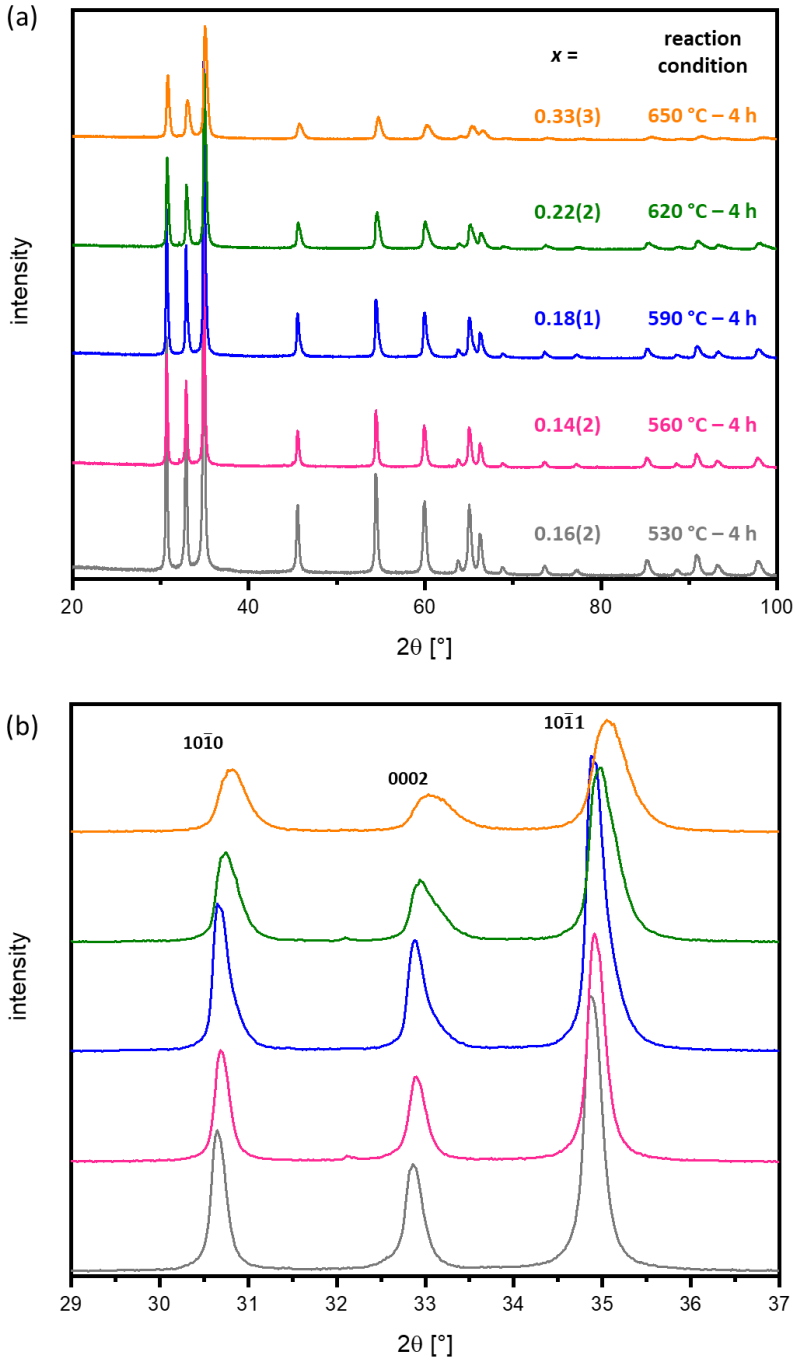

Figure 50 XRD patterns of samples prepared for 4 hours at 530 °C (grey), 560 °C (pink), 590 °C (blue), 620 °C (olive) and 650 °C (orange) in the region of 20 ° - 100 ° (a) 33 ° - 34 ° 2θ (b). The *hkl* indices according to hexagonal wurtzite-type structure (black, top) are given in the figure.

The wurtzite-type and the β-$NaFeO_2$-type structures are the two possible structures for $Zn_{1+x}Sn_{1-x}(O_xN_{1-x})_2$. Thus, the two groups of strongest reflections 10$\bar{1}$0 and 10$\bar{1}$1 should be the most indicative of distinguishing features of the XRD patterns to distinguish the

two possible crystal structures (splitting of peaks in β-$NaFeO_2$-type structure: $10\bar{1}0$ into 200 and 120, $10\bar{1}1$ into 201 and 121). Figure 50 shows the XRD patterns of the $Zn_{1+x}Sn_{1-x}(O_xN_{1-x})_2$. However, no peak splitting was observed. All $Zn_{1+x}Sn_{1-x}(O_xN_{1-x})_2$ adpot the wurtzite-type structure.

As discussed on the XRD pattern in $Zn_{1+x}Ge_{1-x}(O_xN_{1-x})_2$ in Section 3.3.1, the lower the oxygen content, the more significant the peak separation. Therefore, assuming a similar trend for $Zn_{1+x}Sn_{1-x}(O_xN_{1-x})_2$, signs of peak splitting are most likely to be observed on the $Zn_{1+x}Sn_{1-x}(O_xN_{1-x})_2$ sample with the lowest oxygen content.

Thus, we use the oxygen-poorest sample (prepared at 560 °C - 4 h) as an example. Once the samples prepared in the present work show features of the β-$NaFeO_2$-type structure, the phenomenon, such as weak reflections and peak splitting, should be the most obvious for this oxygen-poorest sample. Figure 51a shows the experimental XRD pattern of this oxygen-poorest sample. In addition, by setting the SOF and lattice constants in the crystal structure model, different cation arrangements (disorder-order) and crystal structures (hexagonal-orthorhombic) can be simulated (Figure 51b, c, d, e), to compare with the experimental pattern.

While $SOF(Zn_{Sn}) = SOF(Zn_{Zn}) = (1 + x)/2$ and $SOF(Sn_{Sn})$, $SOF(Sn_{Zn}) = (1 - x)/2$ reflect the disordered cations, the ordered situation can be simulated by setting $SOF(Zn_{Zn}) = 1$, $SOF(Zn_{Sn}) = 1 - x$ and $SOF(Sn_{Sn}) = x$ (Section 3.4.2, discussion on SOF for $Zn_{1+x}Ge_{1-x}(O_xN_{1-x})_2$). The crystal structure distortion against a hexagonal structure can be simulated by adjusting the lattice parameters *a*, *b* and *c* to adapt an $\alpha \neq 0$. Herein, α is modified to 0.02 (empirical value based on $Zn_{1+x}Ge_{1-x}(O_xN_{1-x})_2$ system) to reflect the β-$NaFeO_2$-type structure.

No evidence of the orthorhombic 110 and 011 reflections in response to cation ordering was found in the XRD pattern of this oxygen-poorest sample (comparing Figure 51a, c, e). Furthermore, no evidence of the peak splitting in response to the lattice distortion was observed in the experimental pattern (comparing Figure 51a, d, e). The simulated pattern assuming disordered cation and no structure distortion matches well with the experimental pattern.

This finding suggests that the zinc tin oxide nitrides prepared in the present work adopt the hexagonal wurtzite-type structure. However, it should be noted that although no clear evidence of the presence of the β-$NaFeO_2$-type structure over the compositional

range in this work, it cannot be asserted that samples with lower oxygen content would not crystallise into the β-$NaFeO_2$-type structure. Therefore, further optimisation of the synthesis method to continue to reduce the oxygen content of the compounds may be the key to further experimentally investigating the ordering of cations in this material.

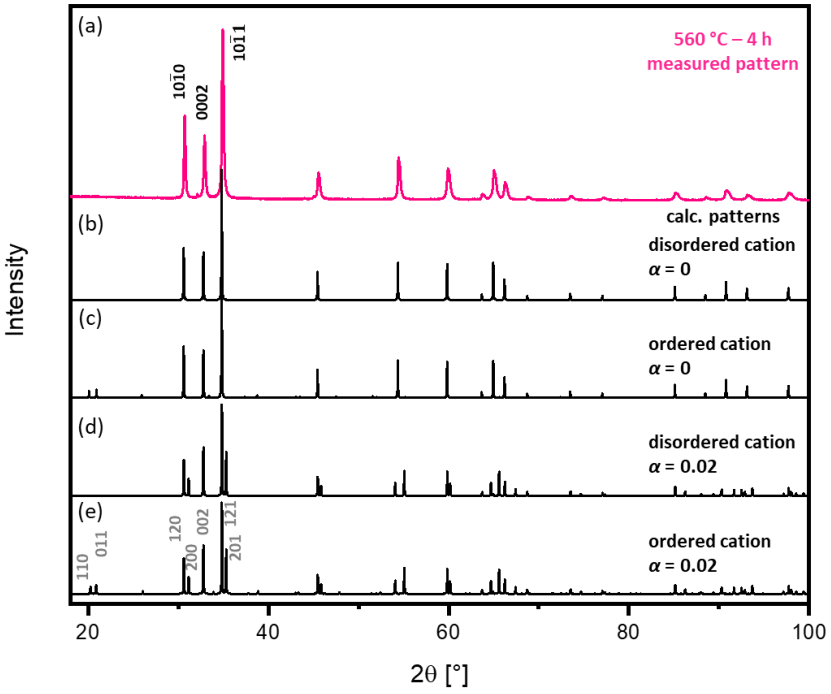

Figure 51 XRD patterns in the region of 18 ° - 38 ° 2θ. The measured XRD of the sample prepared at 560 °C for 4 hours is in pink. The calculated patterns are in black. The *hkl* indices according to hexagonal wurtzite-type structure (black, top) and the *hkl* indices according to the orthorhombic β-$NaFeO_2$-type structure (grey, bottom) are given in the figure.

4.2.2 Lattice constants of $Zn_{1+x}Sn_{1-x}(O_xN_{1-x})_2$

Since the absence of evidence of the β-$NaFeO_2$-type structure, we performed the Rietveld refinements using the structural model of a wurtzite-type phase. The SOF of the model were preset according to the chemical formula $Zn_{1+x}Sn_{1-x}(O_xN_{1-x})_2$ and fixed during the refinement to reflect the statistical distribution of cations in off-stochiometric compounds. The Rietveld refinements were mainly performed to confirm the overall crystal structure and to extract the lattice parameters. Further, an anisotropic line broadening correction was used since the 000*l* reflections are systematically broader

than the remaining reflections (Figure 52 and Appendix), indicative of smaller particle size in the 000*l* direction.

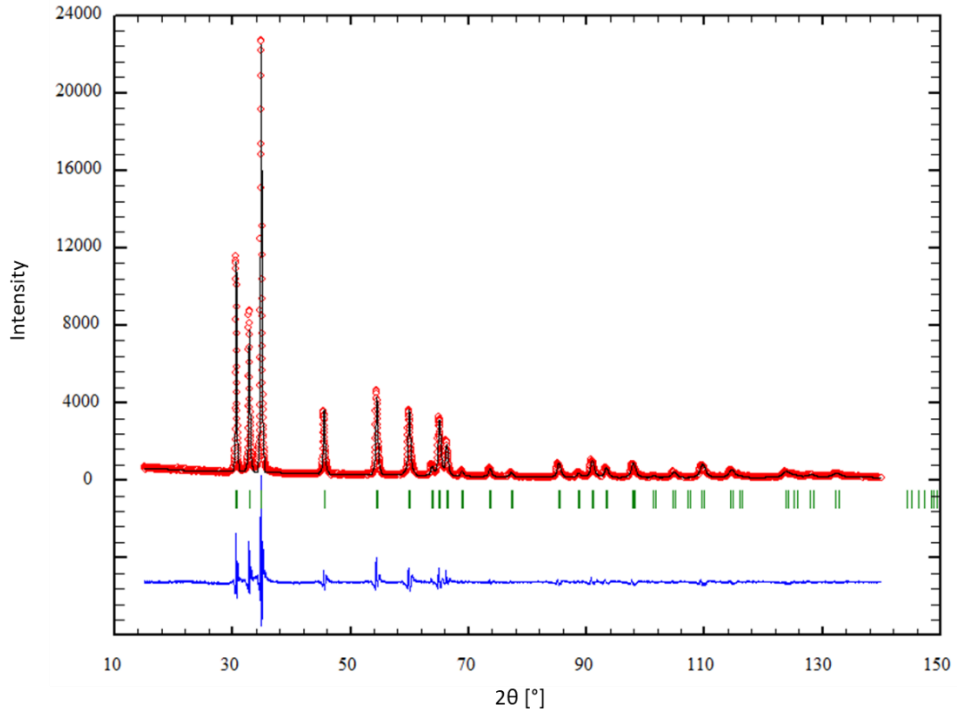

Figure 52 Plot of Rietveld refinement of XRD profile of $Zn_{1+x}Sn_{1-x}(O_xN_{1-x})_2$ (590 °C - 4 h): measured intensity (red circles), calculated intensity (black line), difference I_{obs}-I_{calc} (blue line) and calculated reflection positions (green ticks).

The lattice parameters a_1, a_2 and, particularly, c in the $Zn_{1+x}Sn_{1-x}(O_xN_{1-x})_2$ vary linearly over the composition range (Figure 53), preserving Vegard's law if assuming $ZnSnN_2$ and the oxygen-richest oxide nitride as two ends. In addition, the lattice parameters increase as the composition evolves towards pure nitrides. This phenomenon can be rationalised by regarding the ionic radii: $r(Zn^{2+})$ = 0.6 Å, $r(Sn^{4+})$ = 0.55 Å, $r(O^{2-})$ = 1.35 Å and $r(N^{3-})$ = 1.46 Å,[125] and the change of their shares in these compounds. The samples are oxygen-rich and off-stochiometric with an O/N ratio greater than 0 and Zn/Sn ratio over 1, but which reduce to O/N = 0 and Zn/Sn = 1 when approaching pure $ZnSnN_2$. Although the share of larger Zn^{2+} shrinks from oxide nitride to $ZnSnN_2$, larger N^{3-} replaces the smaller O^{2-} in the structure. And more importantly, the difference in radius between O^{2-} and N^{3-} is more considerable than that between Zn^{2+} and Ge^{4+}, and according to the formula $Zn_{1+x}Sn_{1-x}(O_xN_{1-x})_2$, each Zn-Sn substitution is accompanied by double O-N substitutions. As a result, the change in the share of anions with a larger

difference in radii dominates the trend of lattice parameters and affects the unit cell volume in the same way (Figure 54).

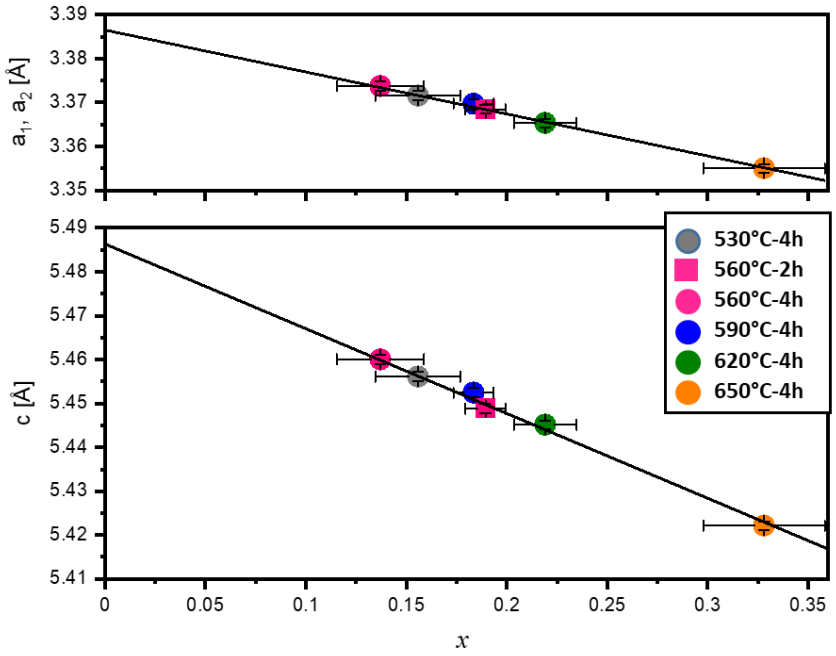

Figure 53 Change of the lattice parameters a_1, a_2 (blue) and c (green) as a function of the oxygen content (represented by x). The fitting was performed by using a linear formula.

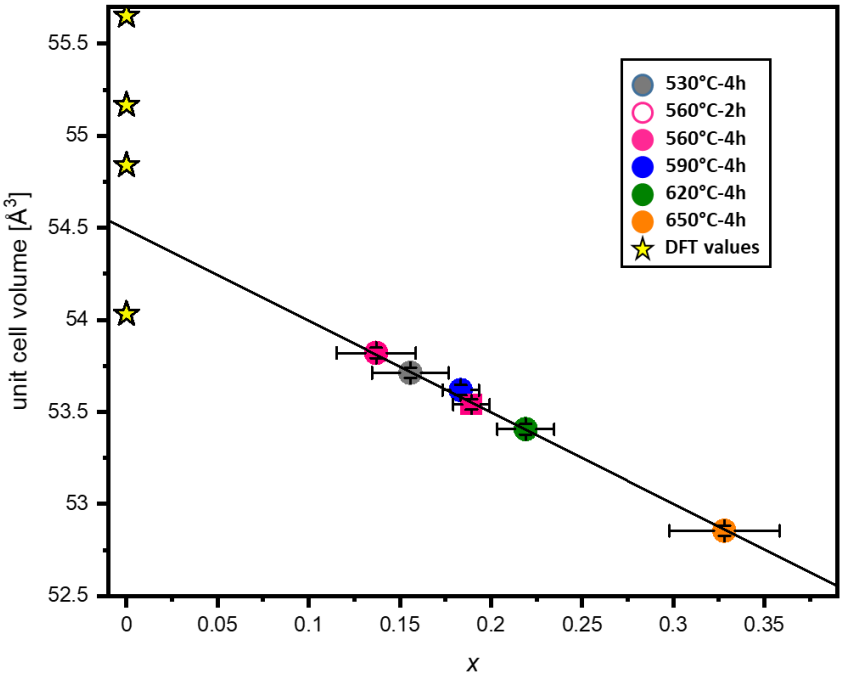

Figure 54 Change of the unit cell volume as a function of the oxygen content (represented by x). The fitting was performed by using a linear formula. The star symbols show the DFT values for $ZnSnN_2$.[63, 65, 72, 126]

4.2.3 Structural inhomogeneity: hints from the overall asymmetric peak broadening in XRD patterns

While all $Zn_{1+x}Sn_{1-x}(O_xN_{1-x})_2$ are well-crystallised and adopt the wurtzite-type structure, anomalous overall asymmetric peak broadening can be observed in the XRD patterns of the $Zn_{1+x}Sn_{1-x}(O_xN_{1-x})_2$ prepared in this work (Figure 55). Furthermore, evident asymmetric peak broadening occurs in the XRD patterns of samples prepared at a temperature over 590 °C. For these samples, one can observe the clear "peak tails" towards higher 2θ for all peaks, including peak 0002, which should be largely unaffected by the potential transformation of crystal structure (wurtzite-type to β-$NaFeO_2$-type structure). Therefore, the overall asymmetric peak broadening is probably due to other causes.

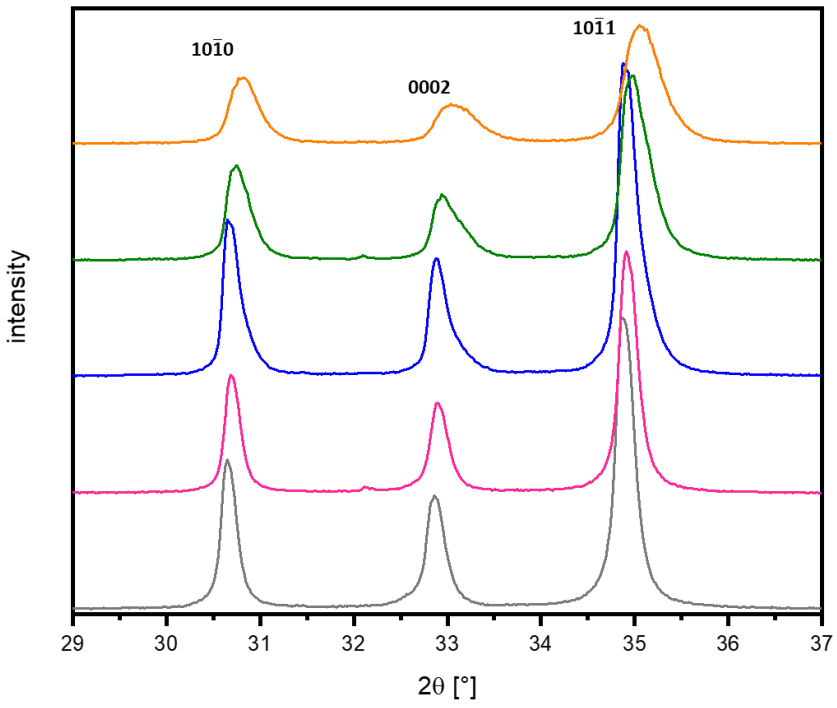

Figure 55 XRD patterns of samples prepared for 4 hours at 530 °C (grey), 560 °C (pink), 590 °C (blue), 620 °C (olive) and 650 °C (orange) in the region of 33 ° - 34 ° 2θ. The *hkl* indices according to hexagonal wurtzite-type structure (black, top) are given in the figure.

The possible causes of the asymmetric peaks in XRD patterns could be due to the instrument setting (i.e. radiation components, Cu-Kα_1 and Cu-Kα_2 for this instrument) or the material itself. Herein, a single-peak analysis of the 0002 reflection was performed (Figure 56), considering Cu-Kα_1 and Cu-Kα_2 radiations, to investigate whether the peak asymmetry sterns from the radiation components.

It is not possible to accurately fit the peak shape of the experimental pattern by considering the different wavelengths of the radiation components. Evident "peak tails" can be observed by comparing the experimental and calculated 0002 reflection in Figure 56.

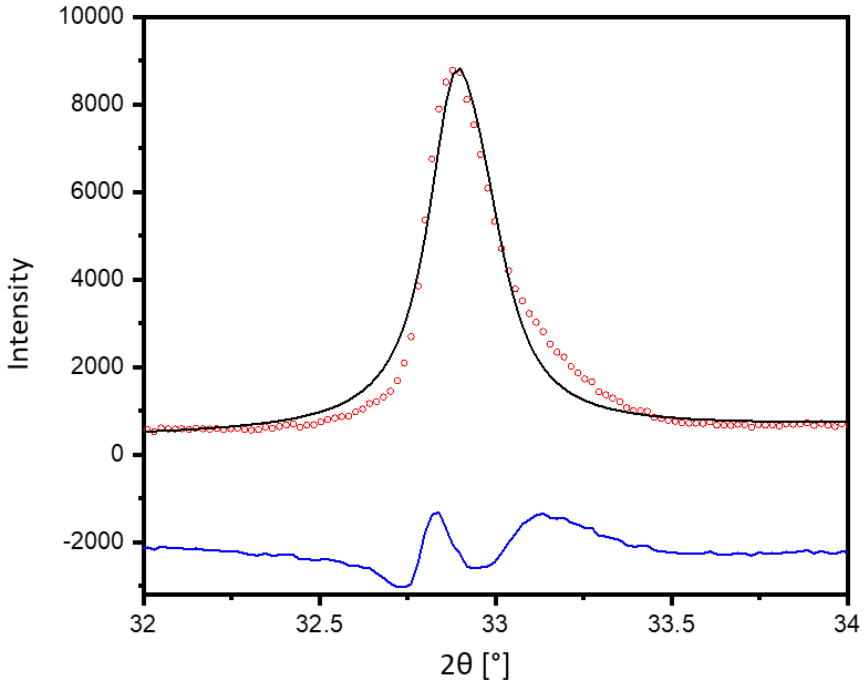

Figure 56 Plot of the single peak fitting of the 0002 peak in XRD pattern of $Zn_{1+x}Sn_{1-x}(O_xN_{1-x})_2$ (590 °C - 4 h): measured intensity (red circles), calculated intensity (black line), and difference I_{obs}-I_{calc} (blue line).

A possible explanation for this peak asymmetric broadening, other than the instrument effect or the crystal structure transformation, is that the material itself causes the peak asymmetric broadening. When the crystal structure is not overall homogenous, the strain on the crystal structure might broaden the peaks. The distribution of the lattice parameters could affect the shape of a peak. Applying a microstrain model into the refinement might be a solution. However, for such a non-asymmetric case observed for the $Zn_{1+x}Sn_{1-x}(O_xN_{1-x})_2$, the general single-phase microstrain model is no longer be

applicable since the microstrain model in FULLPROF assumes symmetric distribution of lattice parameters. To validate if lattice parameter variation is a possible cause, we duplicate the phase and refine lattice parameters and peak shapes of the two phases independently (Figure 57).

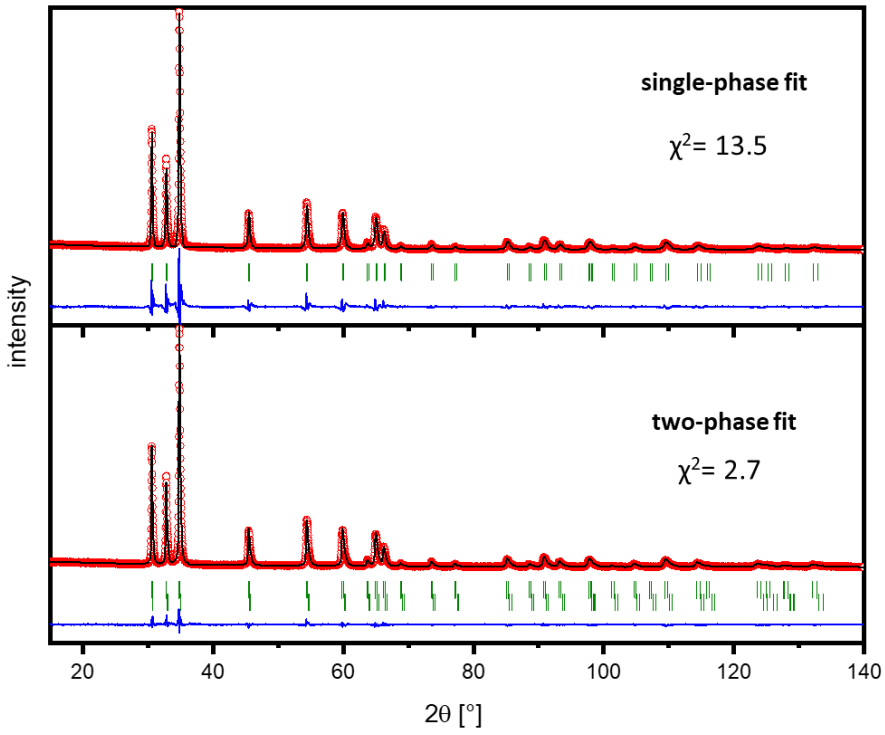

Figure 57 Plot of whole pattern XRD profile (590 °C - 4 h) refinement with the Rietveld method shown in the region of 15 ° - 140 ° 2θ: measured intensities (red circles), calculated profile (black line), the difference between measured and calculated intensities (blue line) and calculated reflection positions (green ticks).

The peak shape can be well fitted with the model assuming two $Zn_{1+x}Sn_{1-x}(O_xN_{1-x})_2$ phases (Figure 58) in the sample. Therefore, one may assume that the sample is inhomogeneous in the lattice parameters, although these phases are both in the wurtzite-type structure.

It should be noted that the successful two-phase fit should not be seen as evidence of the literal presence of two discrete phases in compounds. Instead, introducing the second phase can be thought of as an approximation to a phase continuum with the local gradient in lattice parameters. The inhomogeneity in lattice parameters is probably due to that the sample is inhomogeneous with respect to the chemical composition since it

is confirmed that the lattice parameters of $Zn_{1+x}Sn_{1-x}(O_xN_{1-x})_2$ are the function of oxygen content (x) with linear correlations (Section 4.2.2).

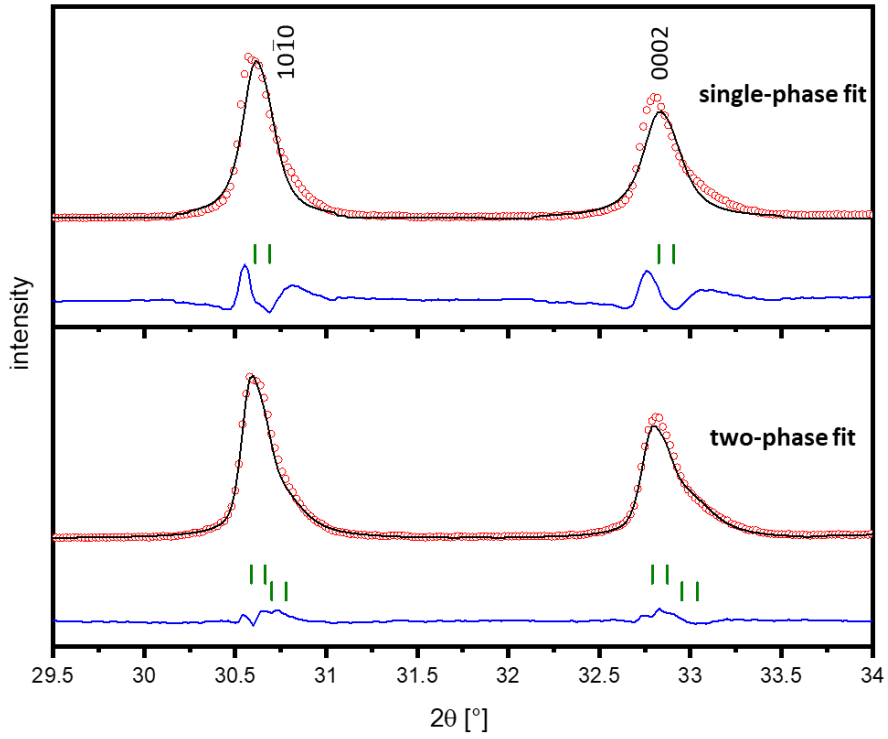

Figure 58 Plot of whole pattern XRD profile (590 °C - 4 h) refinement with the Rietveld method shown in the region of 29.5 ° - 34 ° 2θ: measured intensities (red circles), calculated profile (black line), the difference between measured and calculated intensities (blue line) and calculated reflection positions (green ticks).

4.3 Tuning of the bandgap energy

All $Zn_{1+x}Sn_{1-x}(O_xN_{1-x})_2$ powders prepared in this work are black, indicating a strong light absorption over the visible spectrum. For powders, the reflectance of the UV-Vis spectrum can be used to investigate the optical bandgap energy (Section 2.3).

By extrapolation of the reflectance spectra, one can estimate the optical bandgap energy without considering the electronic transitions.[110] As shown in Figure 59, trend lines can be obtained through the nearest linear region to the tail, and the direct extrapolation yields bandgap energy of the samples.

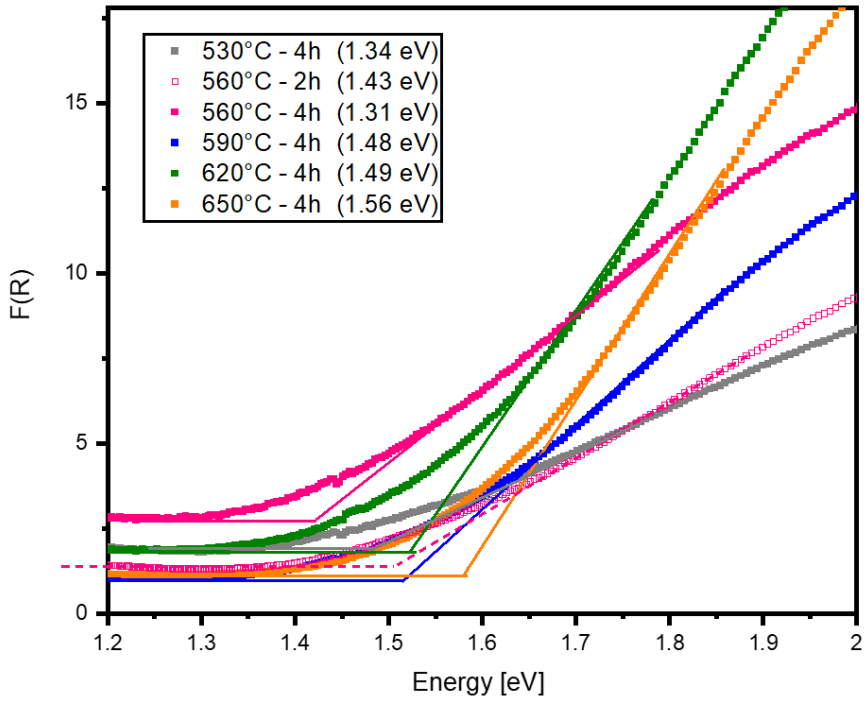

Figure 59 Graphical representation of F(*R*) spectra (plots) and versus energy without considering electronic transitions. The linear trend lines are based on the extrapolation method.

Figure 60 shows these bandgap energy corresponding to the different samples as a function of the chemical composition (represented by *x*). It is evident that the bandgap energy without considering the type of transition increases as the oxygen content and the share of Zn in cations increase. The results largely align with the calculation postulated by Pan et al. based on the computational study of an increasing bandgap trend with oxygen content.[76, 139] However, while their finding suggests an essentially

linear bandgap increase for compositions (x > 0.1), the bandgap estimated by the F(R) plots exhibits a non-linear trend.

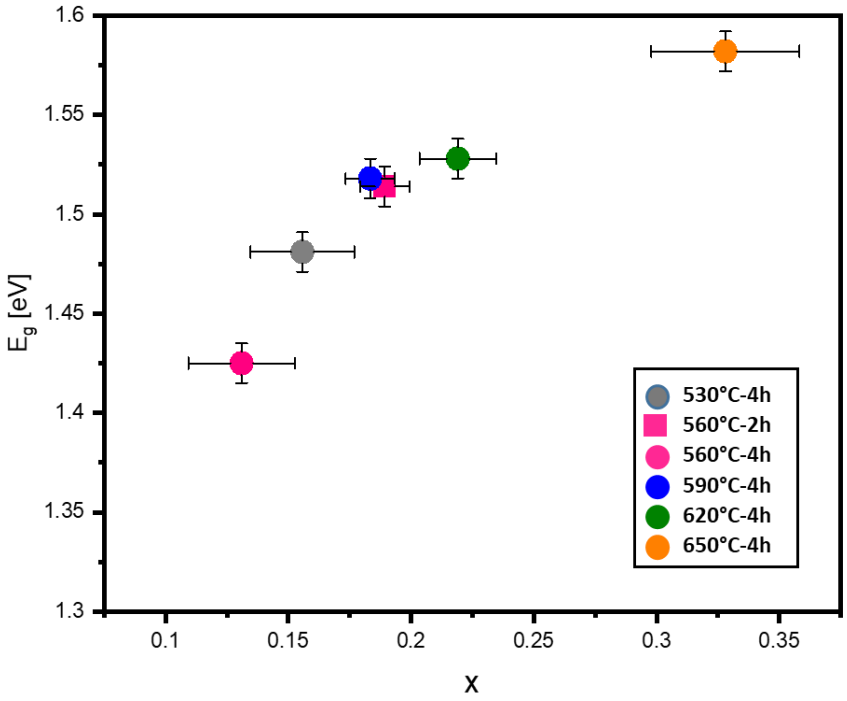

Figure 60 Plots of optical bandgap determined by the direct extrapolation of Kubelka-Munk plots without considering the type of transition (direct or indirect) as a function of the parameter x in the formula $Zn_{1+x}Sn_{1-x}(O_xN_{1-x})_2$.

Furthermore, the transition type (indirect or direct transition) on the $Zn_{1+x}Sn_{1-x}(O_xN_{1-x})_2$ can be investigated by performing Tauc plots, which can be drawn using the Kulbelka-Munk plots with $[F(R)E]^{1/n}$ with n = 2 for indirect transition and n = ½ for direct transition (Section 2.3).

Herein, the $Zn_{1+x}Sn_{1-x}(O_xN_{1-x})_2$ prepared at 530 °C - 4 h was used as an example to show the Tauc plots calculated using n = ½ and n = 2, respectively (Figure 61). Due to the differences in numerical scales resulting from the calculation formulae, the two plots are normalised to facilitate comparing the profiles. While a clear linear zone can be observed on the plots representing the indirect transition, no evident linear zone is found for direct transition. Therefore, one can conclude an indirect transition for $Zn_{1+x}Sn_{1-x}(O_xN_{1-x})_2$ rather than the direct transition. By extrapolating the Tauc plot $[F(R)E]^{1/2}$, the indirect bandgap energy can be estimated from the intersection of the linear zone extension and the background line (Figure 62).

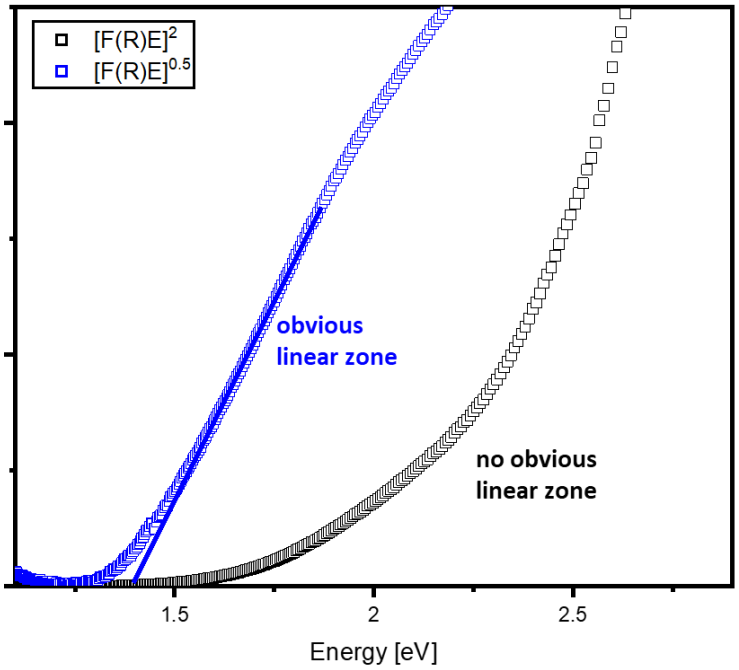

Figure 61 Tauc plot of the $Zn_{1+x}Sn_{1-x}(O_xN_{1-x})_2$ (530 °C – 4 h): for the indirect transition with $[F(R)E]^{0.5}$ (blue square) and the direct transition with $[F(R)E]^2$ (black square). The blue line highlights the linear zone for the indirect transition plots.

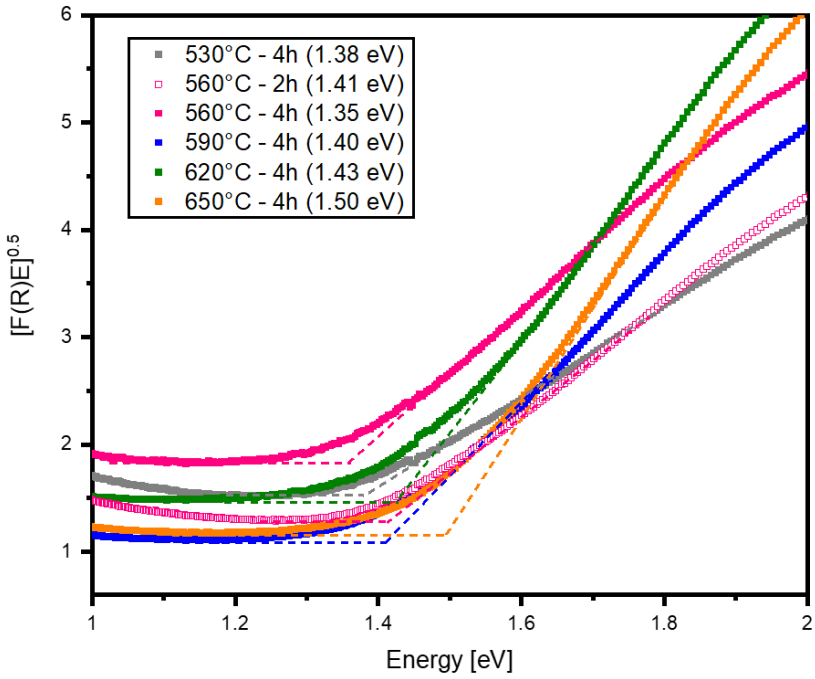

Figure 62 Graphical representation of Tauc plots (indirect transition). The linear trend lines (dash lines) are based on the extrapolation of linear zone.

The indirect bandgap energy of $Zn_{1+x}Sn_{1-x}(O_xN_{1-x})_2$ is plotted as a function of chemical composition (represented by x) (Figure 63). The indirect bandgap energy increases from 1.35 eV and 1.50 eV as oxygen content increases from x = 0.16 to x = 0.33. Further, one observes a clear linear relationship between indirect bandgap and chemical composition. Fitting the plots by a linear function, one obtains $E_g = 0.71(4)x + 1.27(1)$ with $R^2 = 0.99$. The indirect bandgap energy of $ZnSnN_2$ (x = 0) is predicted to be 1.27 eV using the linear function. This estimated direct bandgap is largely in line with the values of 1.12 eV postulated by DFT calculation.[61-63, 66]

It is worth noting that the debate on the band structure of the $ZnSnN_2$ remains: while most fundamental studies postulate direct bandgap values for $ZnSnN_2$, which varies in a wide range between 1.12 eV - 2.09 eV due to the cation disorder effect,[61-63, 66] the bandstructure for the fully disorder $ZnSnN_2$ is still questionable, as the valence band maximum at Y and Γ k-points are so close that it is difficult to figure out whether this is a direct or indirect bandgap.[63] This discovery provides a new clue to solving the puzzle about the band structure of disordered $ZnSnN_2$ with the hints of the indirect bandgap for the wurtzite-type $ZnSnN_2$.

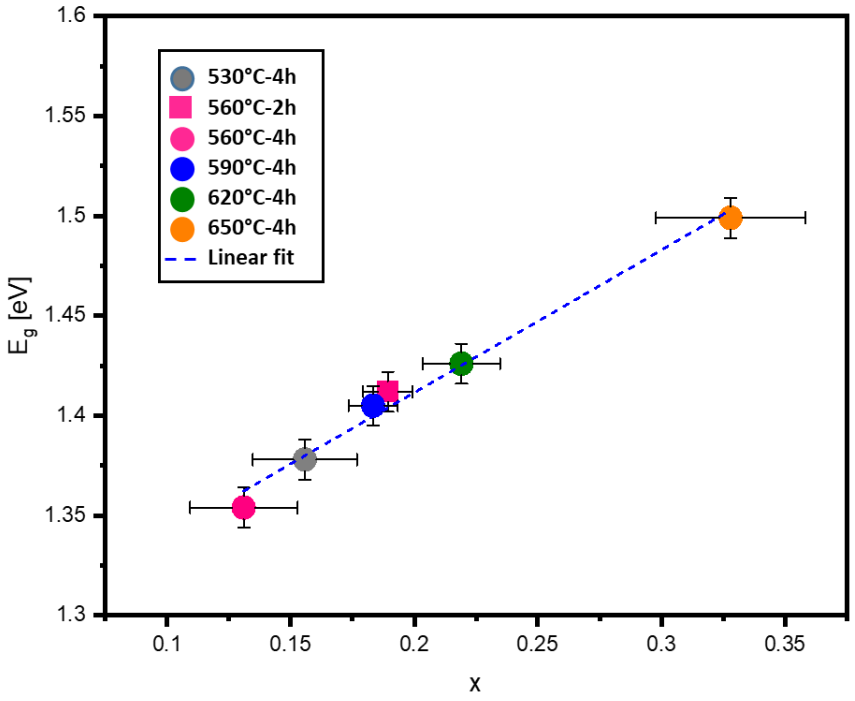

Figure 63 Plots of indirect bandgap energy of $Zn_{1+x}Sn_{1-x}(O_xN_{1-x})_2$ as a function of the oxygen content (represented by x) and linear fit (blue dash line).

4.4 Conclusions

Powder of $Zn_{1+x}Sn_{1-x}(O_xN_{1-x})_2$ was successfully prepared through a solid-state route using binary nitrides as precursors. By controlling the reaction conditions, we obtain compounds with oxygen content between $x = 0.13$ to $x = 0.33$, corresponding to a wide Zn/Sn range between 1.30 to 1.98. This synthesis method opens the possibility to investigate this class of materials based on bulk samples. All samples prepared in the present work crystallise into the wurtzite-type structure; no evidence of the presence of the β-$NaFeO_2$-type structure in the compounds was found. Thus, this work suggests a statistical distribution of cations in $Zn_{1+x}Sn_{1-x}(O_xN_{1-x})_2$, which should crystallise in the wurtzite-type structure. Nonetheless, the possibility that cations in $Zn_{1+x}Sn_{1-x}(O_xN_{1-x})_2$ with a chemical composition closer to stochiometric $ZnSnN_2$ would exhibit an ordered arrangement cannot be ruled out.

In addition, there is a clear correlation between chemical composition and lattice parameters and unit cell size. Furthermore, the optical bandgap energy of $Zn_{1+x}Sn_{1-x}(O_xN_{1-x})_2$ has been investigated. This work suggests that $Zn_{1+x}Sn_{1-x}(O_xN_{1-x})_2$ have an indirect bandgap, which varies linearly with chemical composition. This opens the possibility for targeted bandgap energy tuning through controlled chemical composition.

Chapter V

Summary

Zn-IV-N_2 (IV: Ge, Sn), as promising absorber materials for solar cell applications, have attracted intense attention in the past few years as earth-abundant alternatives of the wurtzite-derived group III-nitrides. With a postulated power conversion efficiency of around 22 %,[140] this class of material is potent to fulfil commercial photovoltaic applications. This class of ternary nitride provides a unique bandgap tunability through the cation disorder effect, in addition to alloying with other elements, allowing the bandgap in a broader absorption range of sunlight. However, the disorder effect on the crystal structure and the material properties remains poorly understood, is still one of the bottlenecks to developing high-efficiency solar cells.

This work uses the oxygen-containing approximants $Zn_{1+x}IV_{1-x}(O_xN_{1-x})_2$ (IV: Ge, Sn) as an exemplary system to understand the phase relations and structure-property relationship of the Zn-IV-N_2 (IV: Ge, Sn). Simultaneous Rietveld refinement of neutron and X-ray diffraction data was performed to evaluate the cation disorder in the $Zn_{1+x}Ge_{1-x}(O_xN_{1-x})_2$. Understanding the cation disorder in the structure further allows the investigation of the effect of cation disorder on the optical bandgap energy, which is essential for solar cell application.

Furthermore, a new synthesis method for $Zn_{1+x}Sn_{1-x}(O_xN_{1-x})_2$ powder is proposed in this work. Rietveld refinement of XRD patterns of the well-crystallised powders facilitates understanding the crystal structure of $Zn_{1+x}Sn_{1-x}(O_xN_{1-x})_2$. In addition, bandgap analysis was performed by UV-Vis methods. The structure-bandgap relationship was revealed by correlating the results from Rietveld refinement and UV-Vis analysis.

Synthesis

The breakthrough in this work is that the synthesis of compositionally tunable powder materials has been achieved. The $Zn_{1+x}Ge_{1-x}(O_xN_{1-x})_2$ were prepared by nitridation of Zn_2GeO_4 using the ammonolysis reaction. By varying the reaction conditions, we confirm the synthesis window of the phase-pure $Zn_{1+x}Ge_{1-x}(O_xN_{1-x})_2$ with $0 < x < 0.34(1)$ using this method. In addition, we confirm that NH_3 flow rather than N_2 atmosphere

must be used during the cooling process to ensure the successful synthesis of β-$NaFeO_2$-type $Zn_{1+x}Ge_{1-x}(O_xN_{1-x})_2$. Furthermore, we gain further insight into the reaction mechanism by combining chemical analysis and reaction conditions and achieving the targeted synthesis of well-crystallised powders. The reaction includes two steps that nitrogen is first introduced into the material before the extraction of Zn and O. The second step largely governs the chemical composition of $Zn_{1+x}Ge_{1-x}(O_xN_{1-x})_2$.

Phase-pure $Zn_{1+x}Sn_{1-x}(O_xN_{1-x})_2$ powder was synthesised using a solid-state approach under ambient pressure in the present work. By analysing the phase share of the multiphase products in the intermediate steps, this synthetic method was optimised to improve the yield of the target $Zn_{1+x}Sn_{1-x}(O_xN_{1-x})_2$ phase. By varying reaction temperature and time, this work achieves a wide chemical composition range of $0.13(1) < x < 0.33(1)$.

Crystal structure determination

The results confirm that $Zn_{1+x}Ge_{1-x}(O_xN_{1-x})_2$ can crystallise in the wurtzite-type and the β-$NaFeO_2$-type structure. The crystal structure transforms from the β-NaFeO2-type structure to the wurtzite-type structure with increasing oxygen content. The crystal structure analysis was performed by refinement, including the Rietveld and Le Bail methods. The lattice constants *a*, *b* and *c* vary differently with the chemical composition. In particular, the change of the trend of *b* at $x = 0.07$ is obvious. The evident peak splitting in XRD, which indicates the β-$NaFeO_2$-type structure, can be observed for samples with $x < 0.07$. The asymmetric broadening of peaks that should be split in XRD patterns can be observed for samples with $x > 0.07$ until $x \approx 0.33$. The asymmetric broadening of peaks suggests the orthorhombic crystal structure of the samples. The oxygen-richest samples with $x \approx 0.33$ shows no evidence of the β-$NaFeO_2$-type structure. This work defines a distortion factor (α) to quantify the stage of the crystal structure transformation between the wurtzite-type and the β-$NaFeO_2$-type structure. The results quantitively reveal crystal structure transformation with chemical composition by α-x correlation.

In addition, all $Zn_{1+x}Sn_{1-x}(O_xN_{1-x})_2$ prepared in this work crystallise in the wurtzite-type structure. No evidence of the β-$NaFeO_2$-type structure was found. The lattice constant of the $Zn_{1+x}Sn_{1-x}(O_xN_{1-x})_2$ was evaluated by Rietveld refinement assuming the single-

phase model. The lattice constants and unit cell volume vary linearly with the chemical composition (represented by x). The unit cell volume of the $ZnSnN_2$ predicted in this work is largely in line with the values postulated by DFT calculations. Moreover, the overall peak asymmetric broadening was observed for the samples prepared at a temperature over 590 °C, suggesting structural inhomogeneity in the samples.

Cation disorder

Applying neutron diffraction to the $Zn_{1+x}Ge_{1-x}(O_xN_{1-x})_2$ system opens the possibility to perform comprehensive whole-pattern fitting methods to directly calculate the site occupancy factor (SOF) in each crystallographic site in the crystal structure. The intrinsic and extrinsic cation disorders are analysed based on the simultaneous Rietveld refinement of neutron and X-ray diffraction data. The intrinsic cation disorder varies with the crystal structure. A high degree of cation disorder can be found in the wurtzite-type $Zn_{1+x}Ge_{1-x}(O_xN_{1-x})_2$. Interestingly, however, no clear relationship was found between intrinsic cation disorder and oxygen content (represented by x), although the crystal structure also showed a clear correlation with x. In addition, the intrinsic cation disorder has a linear relationship with reaction time, particularly for the samples towards to long reaction time. Furthermore, the extrinsic cation disorder is directly correlated with the chemical composition.

There is no evidence of orthorhombic structure for $Zn_{1+x}Sn_{1-x}(O_xN_{1-x})_2$ prepared in this work; this confirms the wurtzite-type structure for these compounds; hence a statistical distribution of cations.

Tuning of the bandgap energy

This work has established that $Zn_{1+x}IV_{1-x}(O_xN_{1-x})_2$ (IV: Ge, Sn) provide excellent bandgap tunability. Chemical composition, crystal structure, and cation disorder may be among the factors affecting bandgap energy. One can engineer the bandgap energy of these compounds by controlling the synthesis conditions.

For $Zn_{1+x}Ge_{1-x}(O_xN_{1-x})_2$, the results reveal the relationship of bandgap energy with chemical composition, crystal structure, and cation disorder. Overall, increasing the degree of cation order and reducing the oxygen content favours large bandgap energy. The widest bandgap is present for the β-$NaFeO_2$-type $ZnGeN_2$ with $x = 0$.

Conversely, samples with high oxygen content and a high degree of cation disorder show lower bandgap energy. The results predict that pure $ZnGeN_2$ powders possess a direct bandgap of c.a 3.6(1) eV that matches the DFT predicted values of 3.65 eV[65]. The disordered $Zn_{1+x}Ge_{1-x}(O_xN_{1-x})_2$ should have bandgap energy of c.a. 2.7(1) eV higher than the calculated value of 1.21 eV[65] for disordered $ZnGeN_2$. Thus, one should not ignore the influence of chemical composition on bandgap energy onset beyond the cation disorder effect in these compounds. Furthermore, one should not simply interpret this compound as an alloy of ternary nitrides and zinc oxide, although it is chemically similar to an alloy system. However, there is no evidence that the relationship between bandgap energy and chemical composition exhibits the bowing effect common to alloy systems. The complex relationship between bandgap energy and chemical composition still need to be explored.

For $Zn_{1+x}Sn_{1-x}(O_xN_{1-x})_2$, the bandgap energy is mainly controlled by chemical composition and lattice constants. Increasing the oxygen content of the compound leads to an increase in the bandgap values. Further, the results suggest that the wurtzite-type $Zn_{1+x}Sn_{1-x}(O_xN_{1-x})_2$ has an indirect bandgap. The indirect bandgap implies the involvement of phonons in the bandgap transition of electrons in these disordered compounds. Thus, one should take into account the effect of the transition type on the efficiency while applying this such disordered materials as absorption layers for solar cells.

Chapter VI

Outlook

The present work is a fundamental research based on powder materials. Nevertheless, our findings facilitate the applied research on developing and optimising devices based on material systems that allow for similar disorder effects, particularly for the targeted preparation of absorber layers in thin-film devices. For example, in addition to controlling film composition by varying the feedstock supply ratio to influence material properties, modulating parameters related to crystallisation kinetics such as substrate temperature may additionally influence the disorder effect since the independence of intrinsic cation disorder with composition. Our findings provide guidance for more precise access to the materials designed and contribute to developing the new generation of high-performance devices based on these novel ternary nitrides.

Future investigations into the causes and mechanisms of intrinsic and extrinsic cation disorders need to be performed. However, no obvious correlation between them was found. Therefore, the following questions might be interesting for further studies. For example, why no evident correlation between the intrinsic cation disorder and chemical composition, how the wurtzite-type $Zn_{1+x}Ge_{1-x}(O_xN_{1-x})_2$ achieves a transformation by locally changing distribution of cations towards order through the removal of Zn and O. Solving the above questions helps deepen the overall understanding of the nature of cation disorder in the crystal structure of this class of materials. In addition, the method of synthesis of $Zn_{1+x}Sn_{1-x}(O_xN_{1-x})_2$ powder at the present work is worth optimising to reduce the oxygen content further to approach pure $ZnSnN_2$ in anticipation of observing evidence of cation ordering in the oxygen-poor samples since the ordered β-$NaFeO_2$-type structure is energetically favourable based on theoretical calculations.[65, 66, 75]

Bibliography

1. R. Swami, *Int. J. Sci. Res.*, 2012, **2**, 1-5.
2. S. Fonash, in *Solar Cell Device Physics*, Elsevier, 2012, ch. 3, pp. 127-130.
3. J. L. Gray, in *Handbook of photovoltaic science and engineering*, 2003, ch. 3, pp. 82-128.
4. A. Polman, M. Knight, E. Garnett, B. Ehrler and W. Sinke, *Sol. Energy*, 2018, **2017**, 2016.
5. M. A. Green, E. D. Dunlop, J. Hohl‐Ebinger, M. Yoshita, N. Kopidakis and X. Hao, *Prog. Photovolt.: Res. Appl.*, 2021, **29**, 657-667.
6. F. Herman, *Proceedings of the IRE*, 1955, **43**, 1703-1732.
7. M. Cuniot and Y. Marfaing, *Philos. Mag. B*, 1988, **57**, 291-300.
8. X.-C. Zhang, Y. Jin, K. Yang and L. Schowalter, *Phys. Rev. Lett.*, 1992, **69**, 2303-2306.
9. L. Pavesi, F. Piazza, A. Rudra, J. Carlin and M. Ilegems, *Phys. Rev. B*, 1991, **44**, 9052.
10. M. Nakamura, K. Yamaguchi, Y. Kimoto, Y. Yasaki, T. Kato and H. Sugimoto, *IEEE J. Photovolt.*, 2019, **9**, 1863-1867.
11. G. Fonthal, L. Tirado-Mejıa, J. Marın-Hurtado, H. Ariza-Calderon and J. Mendoza-Alvarez, *J. Phys. Chem. Solids*, 2000, **61**, 579-583.
12. N. Kato, S. Moribe, M. Shiozawa, R. Suzuki, K. Higuchi, A. Suzuki, M. Sreenivasu, K. Tsuchimoto, K. Tatematsu and K. Mizumoto, *J. Mater. Chem. A*, 2018, **6**, 22508-22512.
13. C. Yan, J. Huang, K. Sun, S. Johnston, Y. Zhang, H. Sun, A. Pu, M. He, F. Liu and K. Eder, *Nat. Energy*, 2018, **3**, 764-772.
14. K.-J. Yang, D.-H. Son, S.-J. Sung, J.-H. Sim, Y.-I. Kim, S.-N. Park, D.-H. Jeon, J. Kim, D.-K. Hwang and C.-W. Jeon, *J. Mater. Chem. A*, 2016, **4**, 10151-10158.
15. Z. Hu, Z. Lin, J. Su, J. Zhang, J. Chang and Y. Hao, *Sol. RRL*, 2019, **3**, 1900304.
16. J. Peng, D. Walter, Y. Ren, M. Tebyetekerwa, Y. Wu, T. Duong, Q. Lin, J. Li, T. Lu and M. A. Mahmud, *Science*, 2021, **371**, 390-395.
17. M. A. Green, *Nat. Energy*, 2016, **1**, 1-4.
18. S. Philipps, *Photovoltaics Report*, Fraunhofer ISE und Werner Warmuth, PSE Projects GmbH, 2019.
19. W. Shockley and H. J. Queisser, *Int. J. Appl. Phys*, 1961, **32**, 510-519.
20. M. A. Green, E. D. Dunlop, J. Hohl-Ebinger, M. Yoshita, N. Kopidakis and X. Hao, *Progress in Photovoltaics: Research and Applications*, 2020, **28**, 629-638.
21. H. Matsushita, T. Ichikawa and A. Katsui, *J. Mater. Sci.*, 2005, **40**, 2003-2005.
22. T. P. Dhakal, C. Y. Peng, R. R. Tobias, R. Dasharathy and C. R. Westgate, *Sol. Energy*, 2014, **100**, 23-30.
23. A. Lafond, L. Choubrac, C. Guillot‐Deudon, P. Deniard and S. Jobic, *Z. Anorg. Allg. Chem.*, 2012, **638**, 2571-2577.
24. K. V. Chauhan and S. K. Rawal, *Proc. Technol.*, 2014, **14**, 430-437.
25. A. Zakutayev, *J. Mater. Chem. A*, 2016, **4**, 6742-6754.
26. A. Pogrebnjak, K. Smyrnova and O. Bondar, *Coatings*, 2019, **9**, 155-182.
27. W. Sun, C. J. Bartel, E. Arca, S. R. Bauers, B. Matthews, B. Orvañanos, B.-R. Chen, M. F. Toney, L. T. Schelhas and W. Tumas, *Nat. Mater.*, 2019, **18**, 732-739.
28. M. T. Hardy, D. F. Feezell, S. P. DenBaars and S. Nakamura, *Mater. Today*, 2011, **14**, 408-415.
29. F. Roccaforte and M. Leszczynski, *Nitride Semiconductor Technology: Power Electronics and Optoelectronic Devices*, John Wiley & Sons, 2020.

30. C. Honsberg, O. Jani, A. Doolittle, E. Trybus, G. Namkoong, I. Ferguson, D. Nicol and A. Payne, *Proceeding of EU PVSEC*, Paris, 2004, pp. 15-20.
31. J. Wu, W. Walukiewicz, K. Yu, W. Shan, J. Ager Iii, E. Haller, H. Lu, W. J. Schaff, W. Metzger and S. Kurtz, *J. Appl. Phys.*, 2003, **94**, 6477-6482.
32. R.-H. Horng, S.-T. Lin, Y.-L. Tsai, M.-T. Chu, W.-Y. Liao, M.-H. Wu, R.-M. Lin and Y.-C. Lu, *EEE Electron Device Lett.*, 2009, **30**, 724-726.
33. B. U. Haq, R. Ahmed, A. Shaari, F. E. H. Hassan, M. B. Kanoun and S. Goumri-Said, *Sol. Energy*, 2014, **107**, 543-552.
34. Y. Marouf, L. Dehimi, F. Bouzid, F. Pezzimenti and F. Della Corte, *Optik*, 2018, **163**, 22-32.
35. M. Wiemer, V. Sabnis and H. Yuen, *Proceeding of High and Low Concentrator Systems for Solar Electric Applications VI*, 2011, p. 810804.
36. N. C. Coronel, Dissertation (Ph.D.), California Institute of Technology, 2016.
37. C. Goodman, *Nature*, 1957, **179**, 828-829.
38. A. D. Martinez, A. N. Fioretti, E. S. Toberer and A. C. Tamboli, *J. Mater. Chem. A*, 2017, **5**, 11418-11435.
39. M. Maunaye and J. Lang, *Mater. Res. Bull.*, 1970, **5**, 793-796.
40. M. Wintenberger, M. Maunaye and Y. Laurent, *Mater. Res. Bull.*, 1973, **8**, 1049-1053.
41. T. Endo, Y. Sato, H. Takizawa and M. Shimada, *J. Mater. Sci. Lett.*, 1992, **11**, 424-426.
42. F. Kawamura, N. Yamada, M. Imai and T. Taniguchi, *Cryst. Res. Technol.*, 2016, **51**, 220-224.
43. F. Kawamura, N. Yamada, X. Cao, M. Imai and T. Taniguchi, *Jpn. J. Appl. Phys.*, 2019, **58**, SC1034.
44. W. R. Lambrecht, E. Alldredge and K. Kim, *Phys. Rev. B*, 2005, **72**, 155202.
45. R. Viennois, T. Taliercio, V. Potin, A. Errebbahi, B. Gil, S. Charar, A. Haidoux and J.-C. Tédenac, *Mater. Sci. Eng. B*, 2001, **82**, 45-49.
46. M. Shang, J. Wang, J. Fan, H. Lian, Y. Zhang and J. Lin, *J. Mater. Chem. C*, 2015, **3**, 9306-9317.
47. Q.-H. Zhang, J. Wang, C.-W. Yeh, W.-C. Ke, R.-S. Liu, J.-K. Tang, M.-B. Xie, H.-B. Liang and Q. Su, *Acta Mater.*, 2010, **58**, 6728-6735.
48. Y. Lee, H. Terashima, Y. Shimodaira, K. Teramura, M. Hara, H. Kobayashi, K. Domen and M. Yashima, *J. Phys. Chem. C*, 2007, **111**, 1042-1048.
49. P. Narang, S. Chen, N. C. Coronel, S. Gul, J. Yano, L. W. Wang, N. S. Lewis and H. A. Atwater, *Adv. Mater.*, 2014, **26**, 1235-1241.
50. S. Kikkawa and H. Morisaka, *Solid State Commun.*, 1999, **112**, 513-515.
51. T. Misaki, A. Wakahara, H. Okada and A. Yoshida, *J. Cryst. Growth*, 2004, **260**, 125-129.
52. L. Zhu, P. Maruska, P. Norris, P. Yip and L. Bouthillette, *MRS OPL*, 1998, **537**, 149-154.
53. S. Limpijumnong, S. N. Rashkeev and W. R. Lambrecht, *MRS Internet J. Nitride Semicond. Res.*, 1999, **4**, 600-605.
54. T. R. Paudel and W. R. Lambrecht, *Physical Review B*, 2008, **78**, 115204.
55. T. J. Peshek, T. R. Paudel, K. Kash and W. R. Lambrecht, *Phys. Rev. B*, 2008, **77**, 235213.
56. T. R. Paudel and W. R. Lambrecht, *Phys. Rev. B*, 2009, **79**, 245205.
57. A. Punya, W. R. Lambrecht and M. van Schilfgaarde, *Phys. Rev. B*, 2011, **84**, 165204.
58. S. Chen, P. Narang, H. A. Atwater and L. W. Wang, *Adv. Mater.*, 2014, **26**, 311-315.
59. N. Feldberg, B. Keen, J. Aldous, D. Scanlon, P. Stampe, R. Kennedy, R. Reeves, T. Veal and S. Durbin, *Proceeding of IEEE Photovoltaic Specialists Conference*, 2012, pp. 002524-002527.

60. N. Feldberg, J. Aldous, P. Stampe, R. Kennedy, T. Veal and S. Durbin, *J. Electron. Mater.*, 2014, **43**, 884-888.
61. A. Punya and W. R. Lambrecht, *Phys.Rev. B*, 2013, **88**, 075302.
62. T. D. Veal, N. Feldberg, N. F. Quackenbush, W. M. Linhart, D. O. Scanlon, L. F. Piper and S. M. Durbin, *Adv. Energy Mater.*, 2015, **5**, 1501462.
63. N. Feldberg, J. Aldous, W. Linhart, L. Phillips, K. Durose, P. Stampe, R. Kennedy, D. Scanlon, G. Vardar and R. Field III, *Appl. Phys. Lett.*, 2013, **103**, 042109.
64. M. Hagemann, C. Bhandari and W. R. Lambrecht, *Solid State Commun.*, 2016, **233**, 46-49.
65. P. C. Quayle, E. W. Blanton, A. Punya, G. T. Junno, K. He, L. Han, H. Zhao, J. Shan, W. R. Lambrecht and K. Kash, *Phys. Rev. B*, 2015, **91**, 205207.
66. L. Lahourcade, N. C. Coronel, K. T. Delaney, S. K. Shukla, N. A. Spaldin and H. A. Atwater, *Adv. Mater.*, 2013, **25**, 2562-2566.
67. J. Breternitz and S. Schorr, *Acta Crystallogr. A*, 2021, **77**.
68. R. R. Schnepf, J. J. Cordell, M. B. Tellekamp, C. L. Melamed, A. L. Greenaway, A. Mis, G. L. Brennecka, S. Christensen, G. J. Tucker and E. S. Toberer, *ACS Energy Lett.*, 2020, **5**, 2027-2041.
69. E. W. Blanton, K. He, J. Shan and K. Kash, *J. Cryst. Growth*, 2017, **461**, 38-45.
70. D. D. Le, T. S. Ngo, J.-H. Song and S.-K. Hong, *Cryst. Growth Des.*, 2018, **18**, 1385-1393.
71. K. K. Chinnakutti, V. Panneerselvam and S. T. Salammal, *Mater Sci Semicond Process*, 2019, **89**, 234-239.
72. N. Senabulya, N. Feldberg, R. A. Makin, Y. Yang, G. Shi, C. M. Jones, E. Kioupakis, J. Mathis, R. Clarke and S. M. Durbin, *AIP Adv.*, 2016, **6**, 075019.
73. R. A. Makin, N. Senabulya, J. Mathis, N. Feldberg, P. Miska, R. Clarke and S. M. Durbin, *J. Vac. Sci. Technol. B*, 2017, **35**, 02B116.
74. S. Lany, A. N. Fioretti, P. P. Zawadzki, L. T. Schelhas, E. S. Toberer, A. Zakutayev and A. C. Tamboli, *Phys. Rev. Mater.*, 2017, **1**, 035401.
75. D. Skachkov, P. C. Quayle, K. Kash and W. R. Lambrecht, *Phys. Rev. B*, 2016, **94**, 205201.
76. J. Pan, J. J. Cordell, G. J. Tucker, A. Zakutayev, A. C. Tamboli and S. Lany, *Npj Comput. Mater.*, 2020, **6**, 1-6.
77. D. Fang and Y. Li, *Phys. Lett. A*, 2020, 126670.
78. Z. Wang, J. Breternitz, D. Fritsch, A. Franz and S. Schorr, *Chem. Sci.*, 2021, **12**, 8493-8500.
79. Y. Xie, K. Javaid, J. Gao, H. Zhang, L. Liang, F. Zhuge, H. Cao, L. Wang and Y. Lu, *J. Mater. Chem. C*, 2017, **5**, 6480-6487.
80. J. Li, Y.-Z. Fu, C.-X. Huang, J.-H. Zhang, X.-Y. Jiang and Z.-L. Zhang, *Appl. Phys. Lett.*, 2016, **108**, 143505.
81. C. L. Melamed, M. B. Tellekamp, J. S. Mangum, J. D. Perkins, P. Dippo, E. S. Toberer and A. C. Tamboli, *Phys. Rev. Mater.*, 2019, **3**, 051602.
82. F. Ye, Q.-Q. Chen, X.-M. Cai, Y.-Z. Xie, X.-F. Ma, K. Vaithinathan, D.-P. Zhang, P. Fan and V. Roy, *J. Mater. Chem. C*, 2020, **8**, 4314-4320.
83. A. L. Greenaway, C. L. Melamed, M. B. Tellekamp, R. Woods-Robinson, E. S. Toberer, J. R. Neilson and A. C. Tamboli, *Annu. Rev. Mater. Res.*, 2020, 587-618.
84. U. Müller, in *International Tables for Crystallography*, 2011, vol. A1, ch. 1.6, pp. 44-46
85. M. von Laue, *Ann. Phys.*, 1913, **346**, 989-1002.
86. W. Friedrich, P. Knipping and M. Laue, *Ann. Phys.*, 1913, **346**, 971-988.
87. W. L. Bragg, *Nature*, 1912, **90**, 410-410.
88. W. Bragg, *Journal*, 1913, **17**, 43–57.

89. W. L. Bragg, *Proc. R. Soc. A*, 1913, **89**, 248-277.
90. W. Friedrich, P. Knipping and M. Laue, *Bayer. Akad. d. Wiss.*, 1912, 314.
91. P. Brown, A. Fox, E. Maslen, M. O'keefe and B. Willis, *International tables for crystallography*, 2006.
92. V. F. Sears, *Neutron news*, 1992, **3**, 26-37.
93. H. M. Rietveld, *J. Appl. Crystallogr.*, 1969, **2**, 65-71.
94. R. Young, *The rietveld method*, 1993.
95. P. Thompson, D. Cox and J. Hastings, *J. Appl. Crystallogr.*, 1987, **20**, 79-83.
96. J. Rodríquez-Carvajal and T. Roisnel, *Proceeding of Mater. Sci. Forum*, 2004, pp. 123-126.
97. D. M. Többens, 2015, DOI: 10.13140/RG.2.1.4440.4966.
98. A. Le Bail, H. Duroy and J. Fourquet, *Mater. Res. Bull.*, 1988, **23**, 447-452.
99. J. Rodríguez-Carvajal, *FullProf*, CEA/Saclay, France, 2001.
100. V. Petříček, M. Dušek and L. Palatinus, *Z. Kristallogr. – Cryst. Mater.*, 2014, **229**, 345-352.
101. A. Franz and A. Hoser, *JLSRF*, 2017, **3**, 103.
102. A. Hewat, *Proceeding of Materials Science Forum*, 1986, pp. 69-80.
103. M. Haschke, *Laboratory micro-X-ray fluorescence spectroscopy*, Springer, 2014.
104. M. O. Krause and J. Oliver, *J. Phys. Chem. Ref. Data*, 1979, **8**, 329-338.
105. A. Tauc, J. Grigorovici and R. Vancu, *Mater. Res. Bull.*, 1966, **3**, 37–46.
106. E. Davis and N. Mott, *Philos. Mag.*, 1970, **22**, 0903-0922.
107. N. F. Mott and E. A. Davis, *Electronic processes in non-crystalline materials*, Oxford university press, 2012.
108. J. I. Pankove, *Optical processes in semiconductors*, Courier Corporation, 1975.
109. P. Kubelka and F. Munk, *Z. Tech. Phys*, 1931, **12**, 193.
110. R. López and R. Gómez, *J. Sol-Gel Sci. Technol.*, 2012, **61**, 1-7.
111. P. Kubelka, *Josa*, 1948, **38**, 448-457.
112. P. Kubelka and F. Munk, *Z. Tech. Phys*, 1931, **12**, 259-274.
113. R. Viennois, T. Taliercio, V. Potin, A. Errebbahi, B. Gil, S. Charar, A. Haidoux and J.-C. Tédenac, *Mater. Sci. Eng., B*, 2001, **82**, 45-49.
114. A. Oribe, K. Tanaka, H. Morikawa and F. Marumo, *Report of the Research Laboratory on Engineering Materials*, 1987, 7-12.
115. M. Zervos, C. Karipi and A. Othonos, *Nanoscale Res. Lett.*, 2012, **7**, 1-8.
116. Z. Fu-Jian, M. Hong-Lei, L. Wei, D. Wei, Z. Xi-Jian, X. Hong-Di, M. Jin, J. Feng, X. Cheng-Shan and Z. Hui-Zhao, *Chin. Phys. Lett.*, 2005, **22**, 907-910.
117. W. M. Haynes, *CRC handbook of chemistry and physics*, CRC press, 2014.
118. W. Sun, A. Holder, B. Orvañanos, E. Arca, A. Zakutayev, S. Lany and G. Ceder, *Chem. Mater.*, 2017, **29**, 6936-6946.
119. P. Bacher, G. Roult, M. Ghers, O. Merdrignac, J. Guyader and Y. Laurent, *Mater. Chem. Phys.*, 1989, **21**, 223-235.
120. J. Breternitz, Z. Wang, A. Glibo, A. Franz, M. Tovar, S. Berendts, M. Lerch and S. Schorr, *Phys. Status Solidi (a)*, 2019, 1800885.
121. K. J. Laidler, *J. Chem. Educ.*, 1984, **61**, 494-498.
122. K. J. Laidler, *J. Chem. Educ.*, 1972, **49**, 343-344.
123. A. K. Galwey and M. E. Brown, *Thermochim. Acta*, 2002, **386**, 91-98.
124. T. Roisnel and J. Rodríquez-Carvajal, *Proceeding of Materials Science Forum*, 2001, pp. 118-123.
125. R. D. Shannon, *Acta Cryst. A*, 1976, **32**, 751-767.
126. A. N. Fioretti, J. Pan, B. R. Ortiz, C. L. Melamed, P. C. Dippo, L. T. Schelhas, J. D. Perkins, D. Kuciauskas, S. Lany and A. Zakutayev, *Mater. Horiz.*, 2018, **5**, 823-830.

127. R. A. Makin, K. York, S. M. Durbin, N. Senabulya, J. Mathis, R. Clarke, N. Feldberg, P. Miska, C. M. Jones and Z. Deng, *Phys. Rev. Lett.*, 2019, **122**, 256403.
128. D. Skachkov, A. P. Jaroenjittichai, L.-y. Huang and W. R. Lambrecht, *Phys.Rev. B*, 2016, **93**, 155202.
129. R. R. Schnepf, B. L. Levy-Wendt, M. B. Tellekamp, B. R. Ortiz, C. L. Melamed, L. T. Schelhas, K. H. Stone, M. F. Toney, E. S. Toberer and A. C. Tamboli, *J. Mater. Chem. C*, 2020, **8**, 4350-4356.
130. S. Nakatsuka and Y. Nose, *J. Phys. Chem. C*, 2017, **121**, 1040-1046.
131. J. Ma, H.-X. Deng, J.-W. Luo and S.-H. Wei, *Phys. Rev. B*, 2014, **90**, 115201.
132. C. G. Van de Walle, J. Neugebauer, C. Stampfl, M. McCluskey and N. Johnson, *Acta Phys. Pol.A*, 1999, **96**, 613-628.
133. J. Wang, Y. Asakura and S. Yin, *Nanoscale*, 2019, **11**, 20151-20160.
134. Y. Lee, K. Teramura, M. Hara and K. Domen, *Chem.mat.*, 2007, **19**, 2120-2127.
135. P. Makuła, M. Pacia and W. Macyk, *J. Phys. Chem. Lett.*, 2018, **9**, 6814-6817.
136. F. Zong, H. Ma, C. Xue, H. Zhuang, X. Zhang, H. Xiao, J. Ma and F. Ji, *Solid State Commun.*, 2004, **132**, 521-525.
137. F. Qu, Y. Yuan and M. Yang, *Chem. Mater.*, 2017, **29**, 969-974.
138. D. C. Hamilton, E. Arca, J. Pan, S. Siol, M. Young, S. Lany and A. Zakutayev, *J. Appl. Phys.*, 2019, **126**, 035701.
139. J. Pan, J. Cordell, G. J. Tucker, A. C. Tamboli, A. Zakutayev and S. Lany, *Adv. Mater.*, 2019, **31**, 1807406.
140. A. Laidouci, A. Aissat and J. Vilcot, *Sol Energy*, 2020, **211**, 237-243.

Appendix

Supporting materials

Chapter 3.2 Elucidation of the reaction mechanism for the synthesis of $ZnGeN_2$ through Zn_2GeO_4 ammonolysis

1) Synthesis conditions of the studied samples

Table S1: Summary of the reaction conditions for the $Zn_{1+x}Ge_{1-x}(O_xN_{1-x})_2$ samples studied herein

Sample number	Precursor mass [g]	Reaction temp. [°C]	dwelling time [h]	gas flow for cooling [$l \cdot min^{-1}$]		Nominal Composition
1	6	835	10	1.5	N_2	$Zn_{1.91}GeO_{0.75}N_{2.10}$
2	6	880	10	0.05	NH_3	$Zn_{1.28}GeO_{0.18}N_{2.07}$
3	3	880	10	0.15		$Zn_{1.13}GeO_{0.09}N_{2.03}$
4	3	880	10	0.15		$Zn_{1.12}GeO_{0.03}N_{2.05}$
5	3	880	12	0.15		$Zn_{1.09}GeO_{0.03}N_{2.04}$
6	3	880	12	0.15		$Zn_{1.06}GeO_{0.03}N_{2.02}$
7	3	880	15	0.15		$Zn_{1.06}GeO_{0.02}N_{2.03}$

2) O and N contents as determined through hot gas extraction

Table S2: O and N contents as determined through hot-gas extraction and the respective sample masses.

Sample number	Oxygen / wt.-%	Nitrogen / wt.-%	Sample Weight / mg
1	5.966	15.60	9.01
	6.728	15.59	8.15
	6.502	15.66	9.12
2	2.122	21.26	8.80
	2.209	21.18	8.60
	2.118	21.15	8.64
3	1.050	21.26	9.67
	1.099	21.18	10.06
	1.004	21.15	10.07
4	0.4103	23.29	8.31
	0.4374	23.34	9.76
	0.4918	23.08	7.78
5	0.3943	23.27	8.96
	0.4048	23.33	9.19
	0.4589	23.33	8.69
6	0.3948	23.34	8.79
	0.3998	23.37	8.81
	0.3844	23.08	9.42
7	0.2845	23.48	9.29
	0.2996	23.39	9.53
	0.3371	23.47	8.82

Chapter 3.3 Crystal structure of $Zn_{1+x}Ge_{1-x}(O_xN_{1-x})_2$

Chapter 3.4 Understanding cation disorder in $Zn_{1+x}Ge_{1-x}(O_xN_{1-x})_2$

3) Information of the studied samples

Table S3: Summary of the reaction conditions, chemical composition, bandgap, lattice constants and disordered cations for the samples studied herein (1. NH_3 flow of 0.15 l/min for reaction and cooling applied; 2. all samples prepared using 3g precursor).

Sample number	Reaction temp. [°C]	Dwelling time [h]	*x* in $Zn_{1+x}Ge_{1-x}(O_xN_{1-x})_2$	Bandgap [eV]	lattice parameter (calculation error of 0.001 taken)			Ge_{Zn}	Zn_{Ge}
					a [Å]	b [Å]	c [Å]		
8	835	12.00	0.31(1)	2.76(5)	5.551	6.426	5.198	-	-
9	850	12.00	0.25(1)	2.77(5)	5.539	6.426	5.198	-	-
10	850	17.00	0.19(1)	2.80(5)	5.532	6.426	5.195	-	-
11	850	21.33	0.09(1)	2.99(5)	5.500	6.417	5.192	0.15(2)	0.24(2)
12	850	23.33	0.07(1)	3.11(5)	5.491	6.420	5.191	0.14(2)	0.21(2)
13	850	24.00	0.05(1)	3.13(5)	5.487	6.422	5.192	0.23(7)	0.28(7)
14	850	25.33	0.07(1)	3.20(5)	5.480	6.428	5.190	0.07(2)	0.14(2)
15	850	27.10	0.03(1)	3.38(5)	5.473	6.442	5.191	-	-
16	865	5.50	0.29(1)	2.75(5)	5.549	6.427	5.197	0.24(6)	0.53(6)
17	865	6.00	0.27(1)	2.78(5)	5.545	6.424	5.196	-	-
18	865	8.00	0.27(1)	2.79(5)	5.540	6.425	5.196	-	-
19	865	12.00	0.14(1)	2.84(5)	5.513	6.419	5.195	0.28(7)	0.41(7)
20	865	14.20	0.07(1)	2.98(5)	5.500	6.415	5.191	0.15(2)	0.22(2)
21	865	16.20	0.05(1)	3.24(5)	5.479	6.429	5.190	0.09(2)	0.13(2)
22	865	18.20	0.04(1)	3.43(5)	5.464	6.443	5.188	0.01(2)	0.05(2)
23	865	20.00	0.02(1)	3.44(5)	5.460	6.449	5.190	0.14(7)	0.16(7)
24	880	2.00	0.35(1)	2.77(5)	5.561	6.424	5.198	-	-
25	880	3.00	0.33(1)	2.78(5)	5.560	6.423	5.198	-	-
26	880	4.00	0.31(1)	2.78(5)	5.556	6.423	5.198	-	-
27	880	6.00	0.25(1)	2.77(5)	5.541	6.423	5.196	-	-
28	880	8.00	0.13(1)	2.88(5)	5.520	6.414	5.194	-	-
29	880	10.00	0.06(1)	3.07(5)	5.489	6.422	5.193	0.24(7)	0.30(7)
30	880	10.50	0.05(1)	-	5.480	6.425	5.191	-	-
31	880	11.00	0.04(1)	-	5.479	6.436	5.194	-	-
32	880	12.00	0.03(1)	3.43(5)	5.461	6.448	5.190	0.13(7)	0.16(7)
33	880	15.00	0.01(1)	3.50(5)	5.459	6.450	5.190	0.16(7)	0.17(7)
34	895	1.00	0.34(1)	2.70(5)	5.558	6.428	5.197	0.26(5)	0.60(5)
35	895	2.00	0.33(1)	2.73(5)	5.556	6.426	5.197	0.23(5)	0.57(5)
36	895	3.00	0.26(1)	2.83(5)	5.538	6.426	5.196	-	-
37	895	4.00	0.21(1)	2.80(5)	5.529	6.426	5.195	-	-
38	895	6.17	0.10(1)	2.92(5)	5.506	6.416	5.192	0.16(2)	0.27(2)
39	895	6.67	0.11(1)	3.03(5)	5.495	6.419	5.192	0.13(2)	0.24(2)
40	895	7.67	0.04(1)	3.16(5)	5.476	6.434	5.190	0.08(2)	0.12(2)
41	895	8.00	0.02(1)	3.40(5)	5.461	6.447	5.190	0.10(7)	0.12(7)
42	895	12.00	-	3.43(5)	5.459	6.451	5.190	0.06(7)	0.06(7)
43	910	2.00	0.31(1)	2.73(5)	5.545	6.424	5.197	-	-
44	910	3.00	0.19(1)	2.81(5)	5.531	6.426	5.195	-	-
45	910	4.00	0.14(1)	2.77(5)	5.516	6.417	5.192	-	-
46	910	4.33	0.12(1)	3.00(5)	5.495	6.420	5.192	0.11(2)	0.23(2)
47	910	4.67	0.04(1)	3.06(5)	5.487	6.425	5.191	0.12(2)	0.16(2)
48	910	5.33	0.03(1)	3.36(5)	5.469	6.439	5.189	0.03(2)	0.06(2)
49	910	6.00	0.03(1)	3.36(5)	5.461	6.448	5.191	0.11(7)	0.14(7)

Table S4: Lattice constants for the oxygen-rich samples, additionally evaluated by using the wurtzite-type structure model.

Samples	Structural model	a/Å	b/Å	c/Å	Note
1	hexagonal	3.212(1)	3.212(1)	5.198(1)	no evident peak splitting
2	hexagonal	3.197(1)	3.197(1)	5.193(1)	no evident peak splitting; evident peak tail for peaks that should be split
8	hexagonal	3.210(1)	3.210(1)	5.198(1)	no evident peak splitting
9	hexagonal	3.207(1)	3.207(1)	5.197(1)	no evident peak splitting
16	hexagonal	3.209(1)	3.209(1)	5.197(1)	no evident peak splitting
17	hexagonal	3.209(1)	3.209(1)	5.196(1)	no evident peak splitting
24	hexagonal	3.211(1)	3.211(1)	5.198(1)	no evident peak splitting
25	hexagonal	3.211(1)	3.211(1)	5.198(1)	no evident peak splitting
26	hexagonal	3.210(1)	3.210(1)	5.198(1)	no evident peak splitting
27	hexagonal	3.207(1)	3.207(1)	5.197(1)	no evident peak splitting
28	hexagonal	3.198(1)	3.198(1)	5.193(1)	no evident peak splitting
29	hexagonal	3.194(1)	3.194(1)	5.191(1)	no evident peak splitting
34	hexagonal	3.212(1)	3.212(1)	5.198(1)	no evident peak splitting
35	hexagonal	3.211(1)	3.211(1)	5.198(1)	no evident peak splitting
36	hexagonal	3.208(1)	3.208(1)	5.196(1)	no evident peak splitting
37	hexagonal	3.205(1)	3.205(1)	5.195(1)	no evident peak splitting; evident peak tail for peaks that should be split
43	hexagonal	3.210(1)	3.210(1)	5.197(1)	no evident peak splitting
44	hexagonal	3.204(1)	3.204(1)	5.195(1)	no evident peak splitting; evident peak tail for peaks that should be split
45	hexagonal	3.198(1)	3.198(1)	5.193(1)	no evident peak splitting; evident peak tail for peaks that should be split

4) Profile of the whole pattern fitting of diffraction data sets

Sample 1:

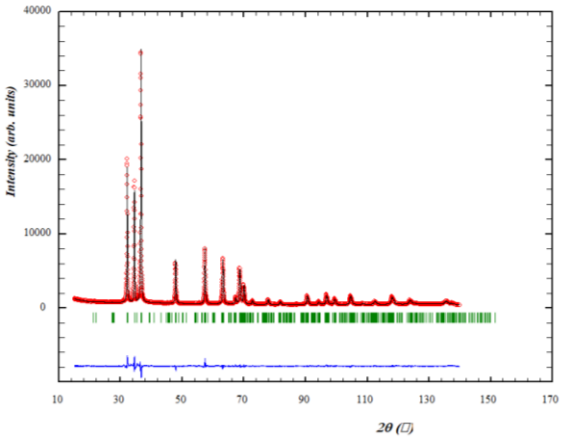

Figure S1: Plot for the Rietveld refinement of the X-ray powder diffraction profile: Measured Intensity (red circles), calculated intensity (black line), difference I_{obs}–I_{calc} (blue line) and calculated reflection positions (green ticks).

Sample 2:

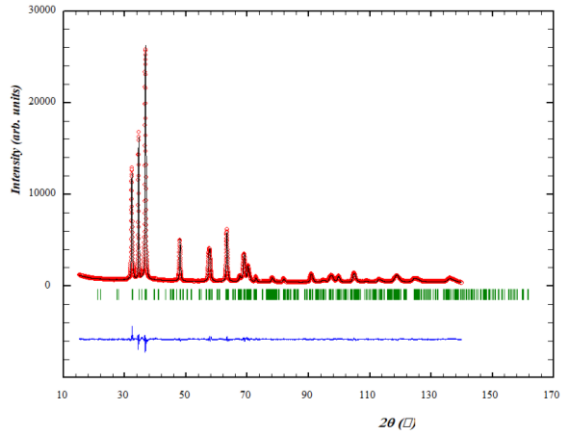

Figure S2: Plot for the Rietveld refinement of the X-ray powder diffraction profile: Measured Intensity (red circles), calculated intensity (black line), difference I_{obs}–I_{calc} (blue line) and calculated reflection positions (green ticks).

Sample 3:

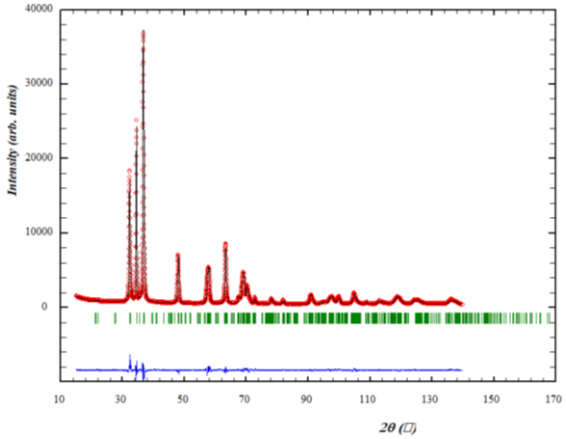

Figure S3: Plot for the Rietveld refinement of the X-ray powder diffraction profile: Measured Intensity (red circles), calculated intensity (black line), difference I_{obs}–I_{calc} (blue line) and calculated reflection positions (green ticks).

Sample 4:

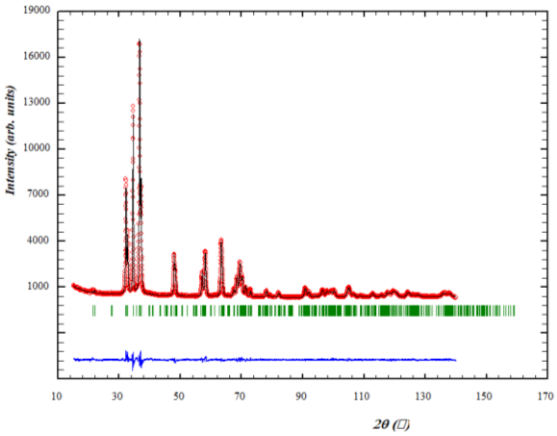

Figure S4: Plot for the Rietveld refinement of the X-ray powder diffraction profile: Measured Intensity (red circles), calculated intensity (black line), difference I_{obs}–I_{calc} (blue line) and calculated reflection positions (green ticks).

Sample 5:

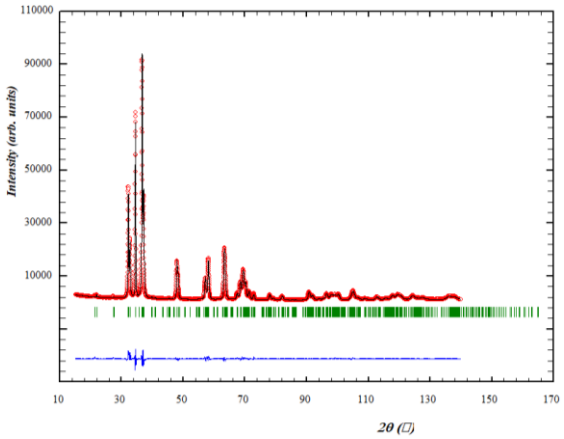

Figure S5: Plot for the Rietveld refinement of the X-ray powder diffraction profile: Measured Intensity (red circles), calculated intensity (black line), difference I_{obs}–I_{calc} (blue line) and calculated reflection positions (green ticks).

Sample 6:

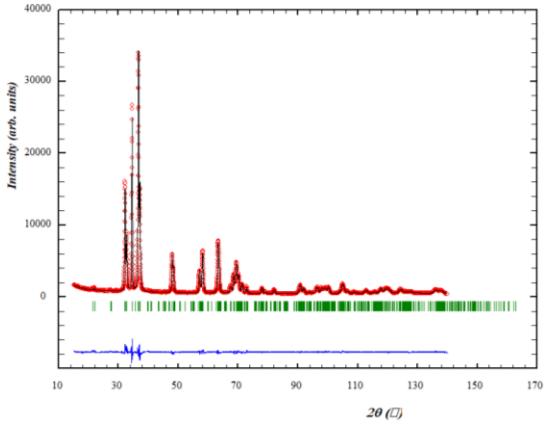

Figure S6: Plot for the Rietveld refinement of the X-ray powder diffraction profile: Measured Intensity (red circles), calculated intensity (black line), difference I_{obs}–I_{calc} (blue line) and calculated reflection positions (green ticks).

Sample 7:

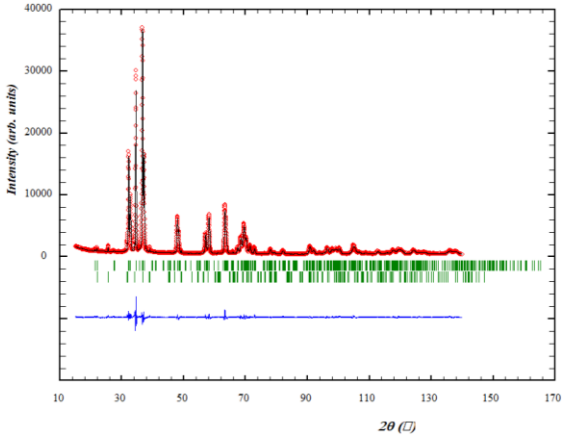

Figure S7: Plot for the Rietveld refinement of the X-ray powder diffraction profile: Measured Intensity (red circles), calculated intensity (black line), difference I_{obs}–I_{calc} (blue line) and calculated reflection positions (green ticks, Ge_3N_4 bottom, Zn-Ge-O-N top).

Sample 8:

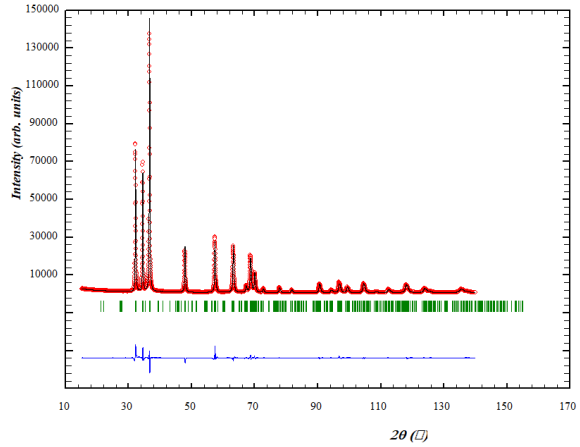

Figure S8: Plot for the Rietveld refinement of the X-ray powder diffraction profile: Measured Intensity (red circles), calculated intensity (black line), difference I_{obs}–I_{calc} (blue line) and calculated reflection positions (green ticks).

Sample 9:

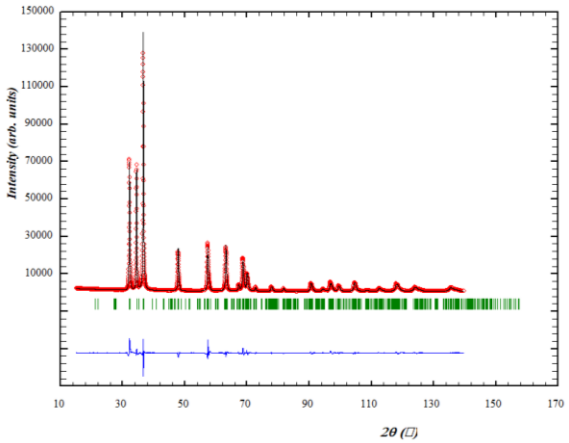

Figure S8: Plot for the Rietveld refinement of the X-ray powder diffraction profile: Measured Intensity (red circles), calculated intensity (black line), difference I_{obs}–I_{calc} (blue line) and calculated reflection positions (green ticks).

Sample 10:

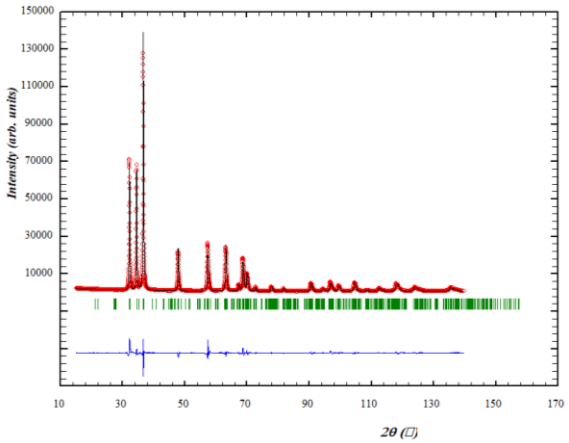

Figure S10: Plot for the Le Bail refinement of the X-ray powder diffraction profile: Measured Intensity (red circles), calculated intensity (black line), difference I_{obs}–I_{calc} (blue line) and calculated reflection positions (green ticks).

Sample 11:

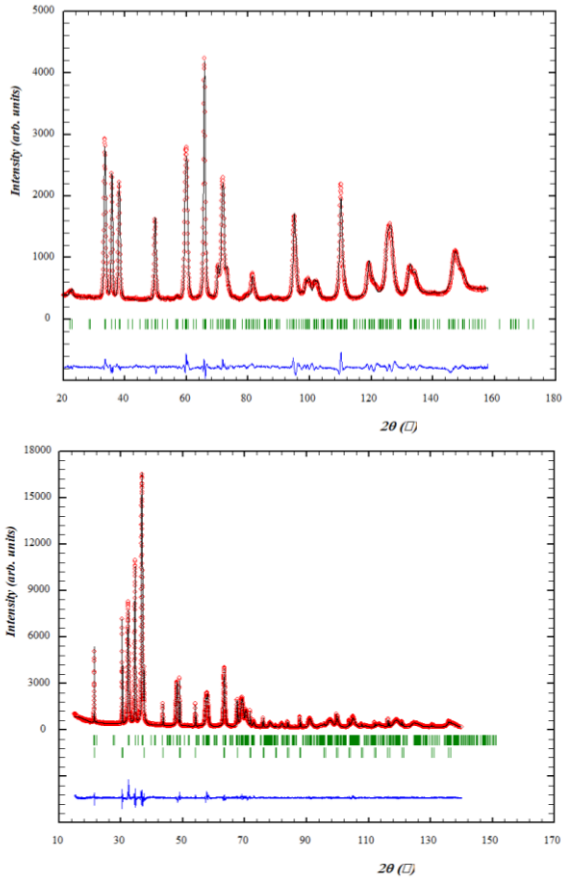

Figure S11: Plot for the simultaneous Rietveld refinement of the neutron (top) and X-ray powder diffraction profile (bottom): Measured Intensity (red circles), calculated intensity (black line), difference I_{obs}–I_{calc} (blue line) and calculated reflection positions (green ticks). XRD pattern includes reflections and calculated reflection position (green ticks at bottom) of LaB_6 standard.

Sample 12:

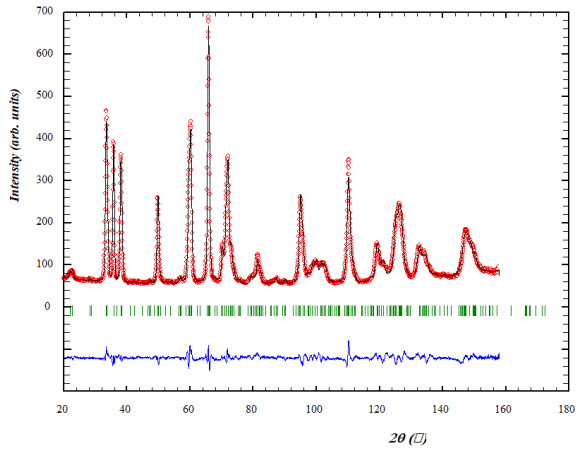

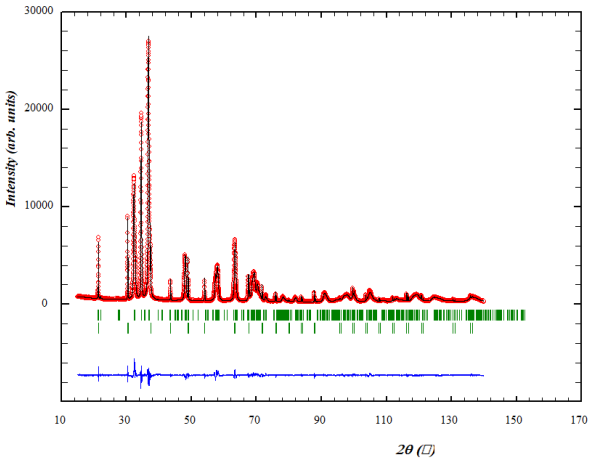

Figure S12: Plot for the simultaneous Rietveld refinement of the neutron (top) and X-ray powder diffraction profile (bottom): Measured Intensity (red circles), calculated intensity (black line), difference I_{obs}–I_{calc} (blue line) and calculated reflection positions (green ticks). XRD figure includes reflections and calculated reflection position (green ticks at bottom) of LaB_6 standard.

Sample 13:

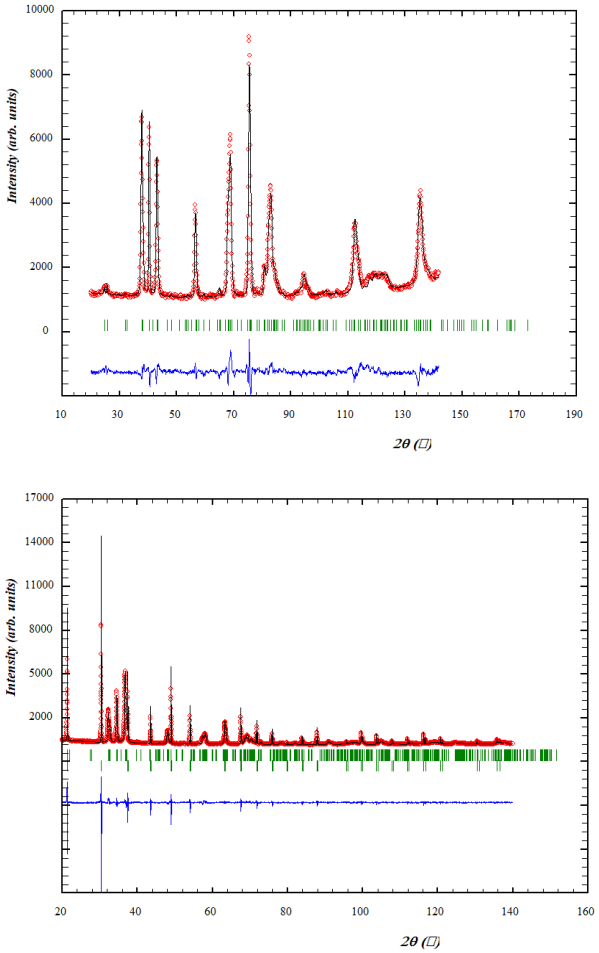

Figure S13: Plot for the simultaneous Rietveld refinement of the neutron (top) and X-ray powder diffraction profile (bottom): Measured Intensity (red circles), calculated intensity (black line), difference I_{obs}–I_{calc} (blue line) and calculated reflection positions (green ticks). XRD figure includes reflections and calculated reflection position (green ticks at bottom) of LaB_6 standard.

Sample 14:

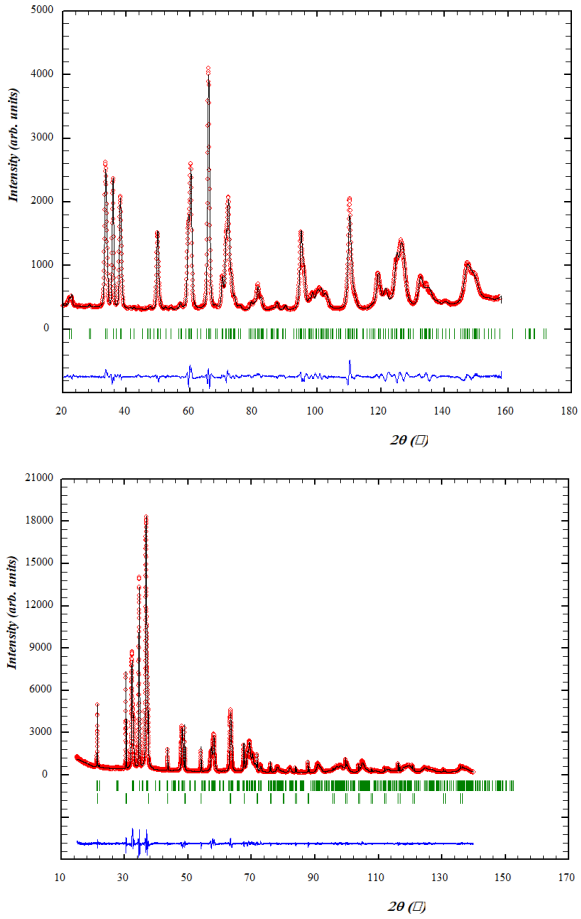

Figure S14: Plot for the simultaneous Rietveld refinement of the neutron (top) and X-ray powder diffraction profile (bottom): Measured Intensity (red circles), calculated intensity (black line), difference I_{obs}–I_{calc} (blue line) and calculated reflection positions (green ticks). XRD figure includes reflections and calculated reflection position (green ticks at bottom) of LaB_6 standard.

Sample 15:

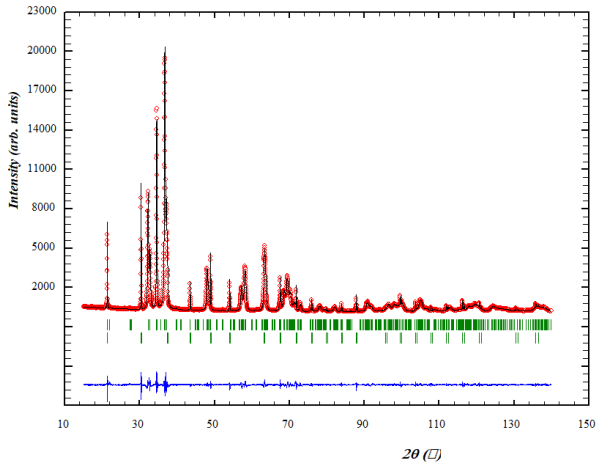

Figure S15: Plot for the Le Bail refinement of the X-ray powder diffraction profile: Measured Intensity (red circles), calculated intensity (black line), difference I_{obs}–I_{calc} (blue line) and calculated reflection positions (green ticks, LaB_6 bottom, Zn-Ge-O-N top).

Sample 16:

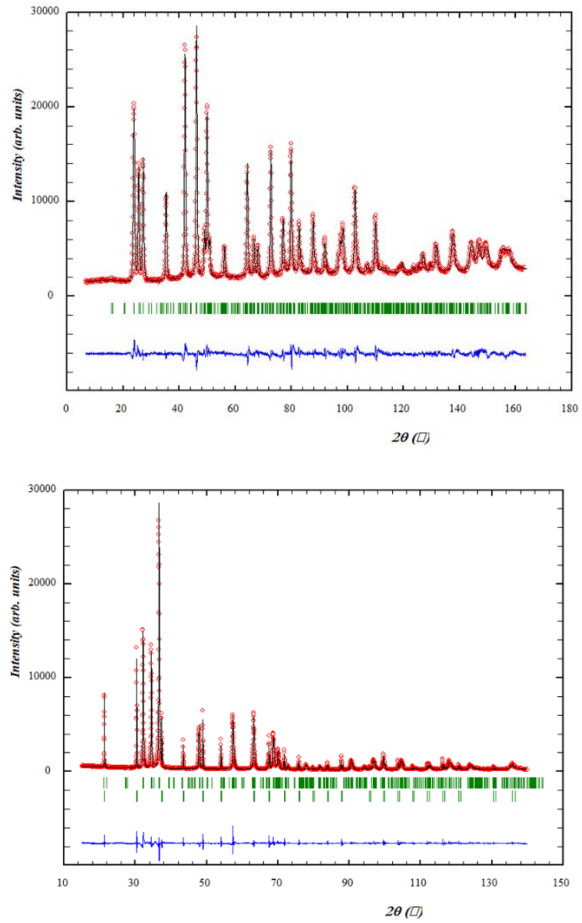

Figure S16: Plot for the simultaneous Rietveld refinement of the neutron (top) and X-ray powder diffraction profile (bottom): Measured Intensity (red circles), calculated intensity (black line), difference I_{obs}–I_{calc} (blue line) and calculated reflection positions (green ticks). XRD figure includes reflections and calculated reflection position (green ticks at bottom) of LaB_6 standard.

Sample 17:

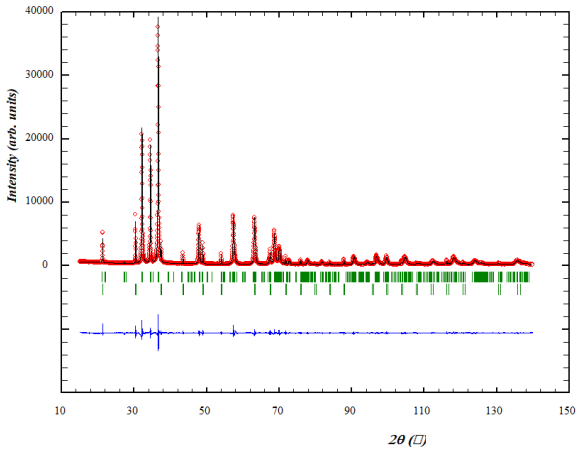

Figure S17: Plot for the Le Bail refinement of the X-ray powder diffraction profile: Measured Intensity (red circles), calculated intensity (black line), difference I_{obs}–I_{calc} (blue line) and calculated reflection positions (green ticks, LaB_6 bottom, Zn-Ge-O-N top).

Sample 18:

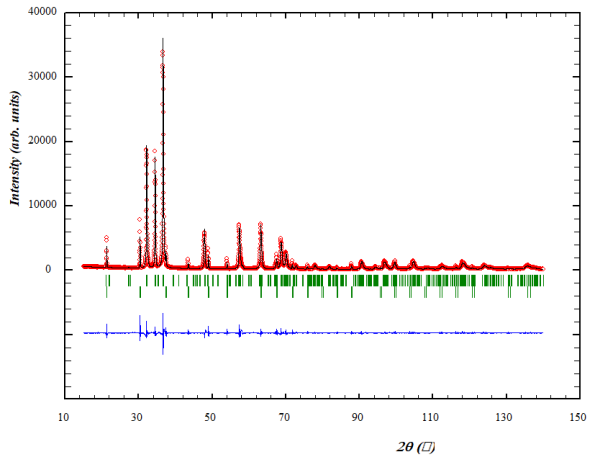

Figure S18: Plot for the Le Bail refinement of the X-ray powder diffraction profile: Measured Intensity (red circles), calculated intensity (black line), difference I_{obs}–I_{calc} (blue line) and calculated reflection positions (green ticks, LaB_6 bottom, Zn-Ge-O-N top).

Sample 19:

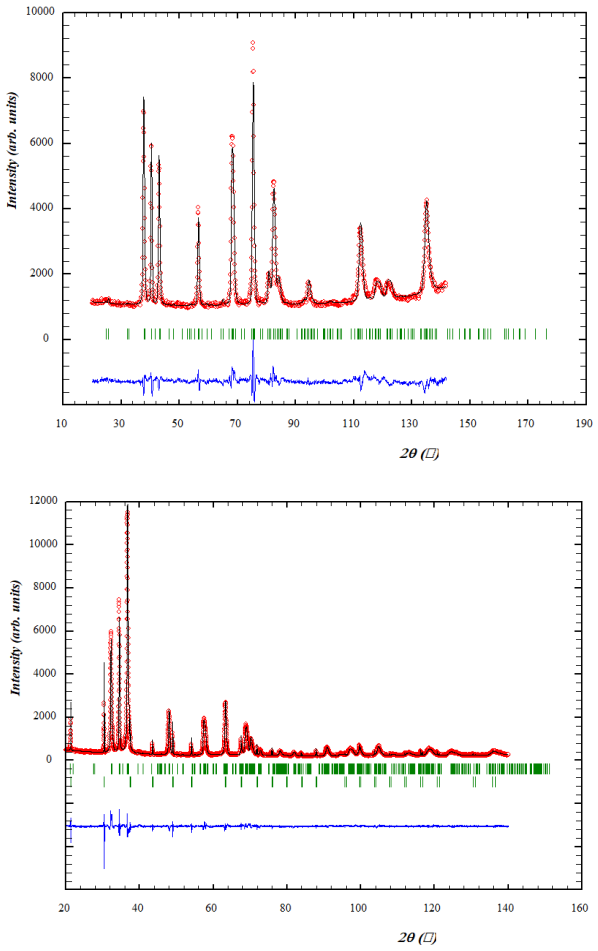

Figure S19: Plot for the simultaneous Rietveld refinement of the neutron (top) and X-ray powder diffraction profile (bottom): Measured Intensity (red circles), calculated intensity (black line), difference I_{obs}–I_{calc} (blue line) and calculated reflection positions (green ticks). XRD figure includes reflections and calculated reflection position (green ticks at bottom) of LaB_6 standard.

Sample 20:

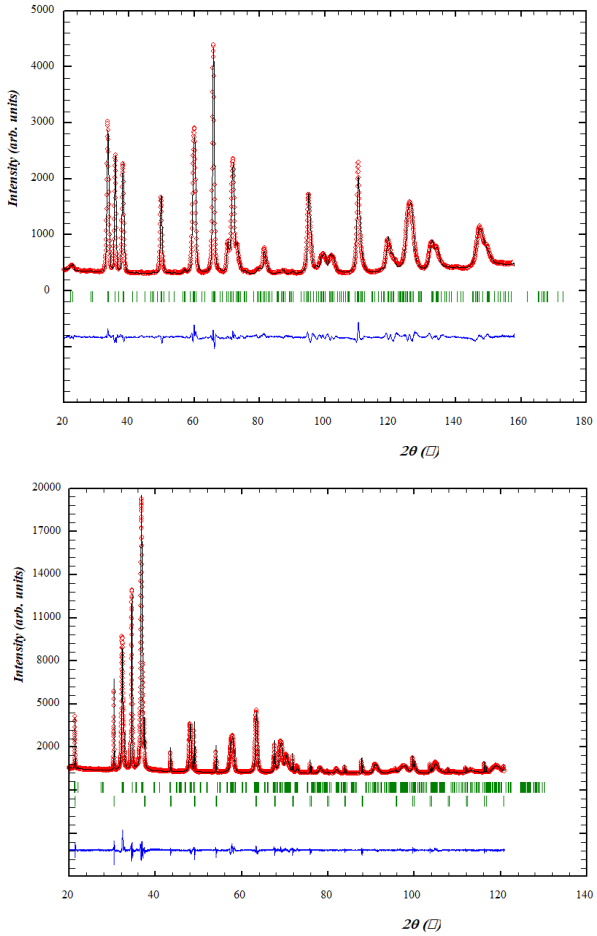

Figure S20: Plot for the simultaneous Rietveld refinement of the neutron (top) and X-ray powder diffraction profile (bottom): Measured Intensity (red circles), calculated intensity (black line), difference I_{obs}–I_{calc} (blue line) and calculated reflection positions (green ticks). XRD figure includes reflections and calculated reflection position (green ticks at bottom) of LaB_6 standard.

Sample 21:

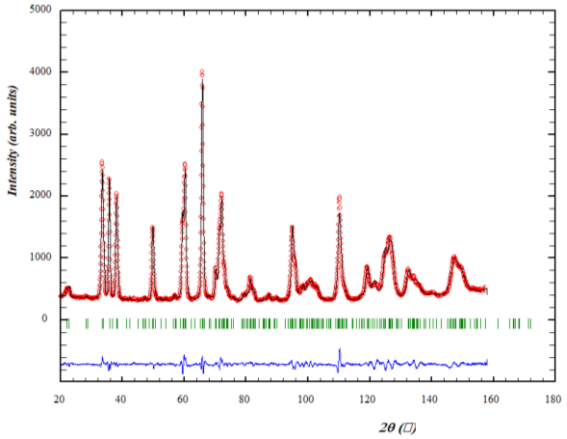

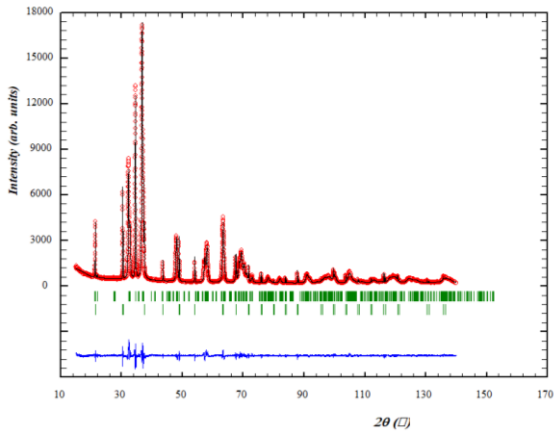

Figure S21: Plot for the simultaneous Rietveld refinement of the neutron (top) and X-ray powder diffraction profile (bottom): Measured Intensity (red circles), calculated intensity (black line), difference I_{obs}–I_{calc} (blue line) and calculated reflection positions (green ticks). XRD figure includes reflections and calculated reflection position (green ticks at bottom) of LaB_6 standard.

Sample 22:

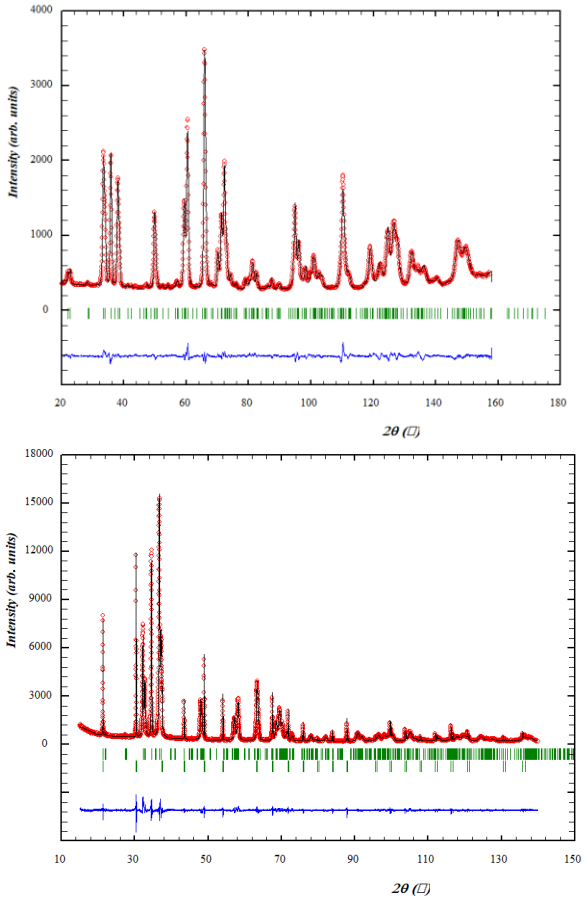

Figure S22: Plot for the simultaneous Rietveld refinement of the neutron (top) and X-ray powder diffraction profile (bottom): Measured Intensity (red circles), calculated intensity (black line), difference I_{obs}–I_{calc} (blue line) and calculated reflection positions (green ticks). XRD figure includes reflections and calculated reflection position (green ticks at bottom) of LaB_6 standard.

Sample 23:

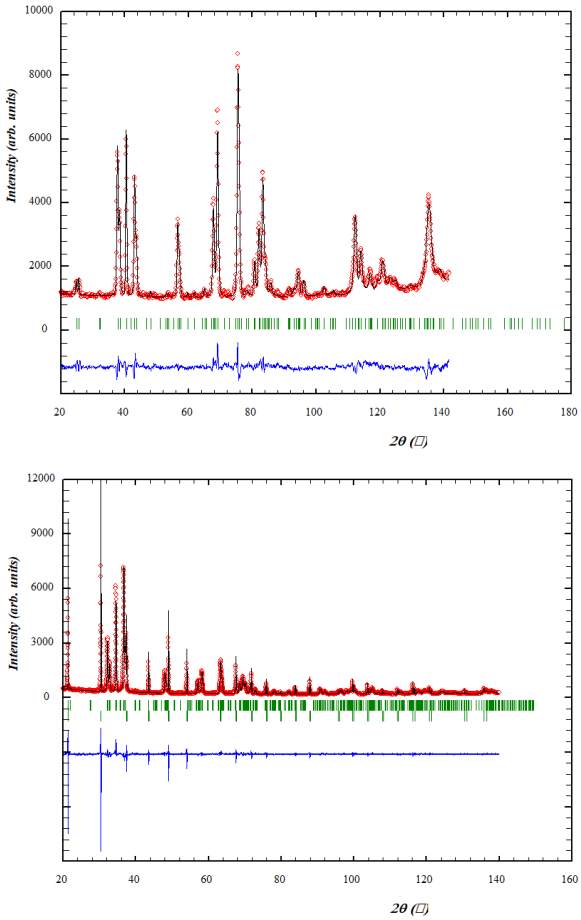

Figure S23: Plot for the simultaneous Rietveld refinement of the neutron (top) and X-ray powder diffraction profile (bottom): Measured Intensity (red circles), calculated intensity (black line), difference I_{obs}–I_{calc} (blue line) and calculated reflection positions (green ticks). XRD figure includes reflections and calculated reflection position (green ticks at bottom) of LaB_6 standard.

Sample 24:

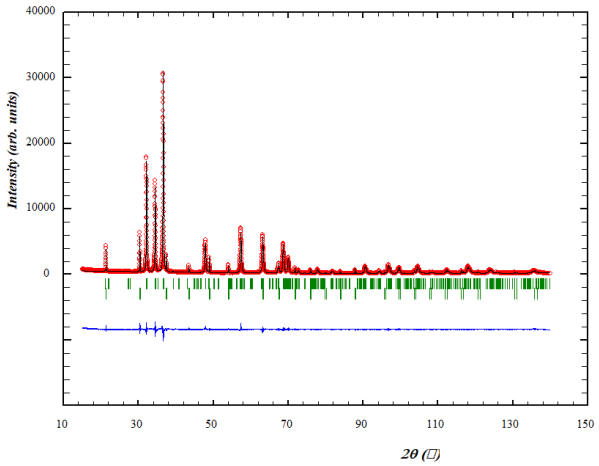

Figure S24: Plot for the Le Bail refinement of the X-ray powder diffraction profile: Measured Intensity (red circles), calculated intensity (black line), difference I_{obs}–I_{calc} (blue line) and calculated reflection positions (green ticks, LaB_6 bottom, Zn-Ge-O-N top).

Sample 25:

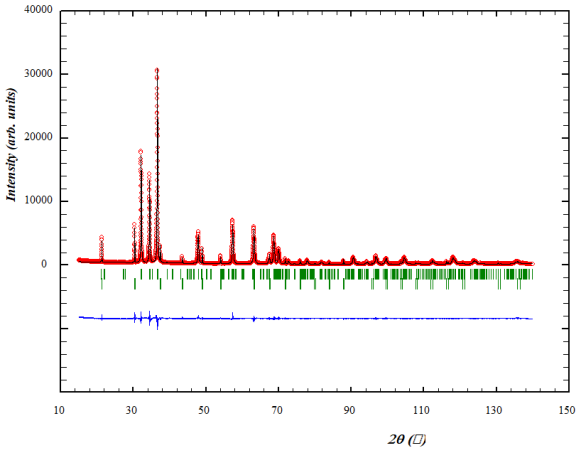

Figure S25: Plot for the Le Bail refinement of the X-ray powder diffraction profile: Measured Intensity (red circles), calculated intensity (black line), difference I_{obs}–I_{calc} (blue line) and calculated reflection positions (green ticks, LaB_6 bottom, Zn-Ge-O-N top).

Sample 26:

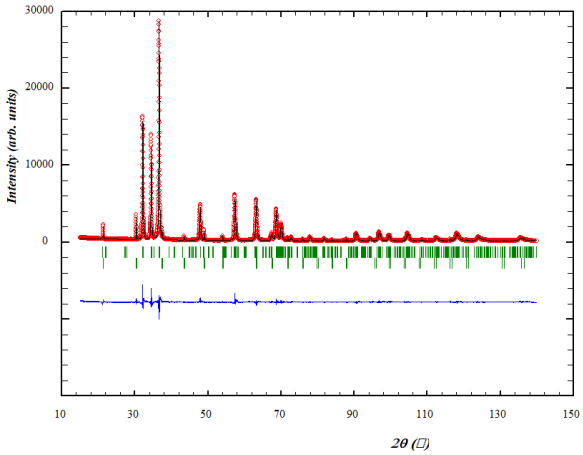

Figure S26: Plot for the Rietveld refinement of the X-ray powder diffraction profile: Measured Intensity (red circles), calculated intensity (black line), difference I_{obs}–I_{calc} (blue line) and calculated reflection positions (green ticks).

Sample 27:

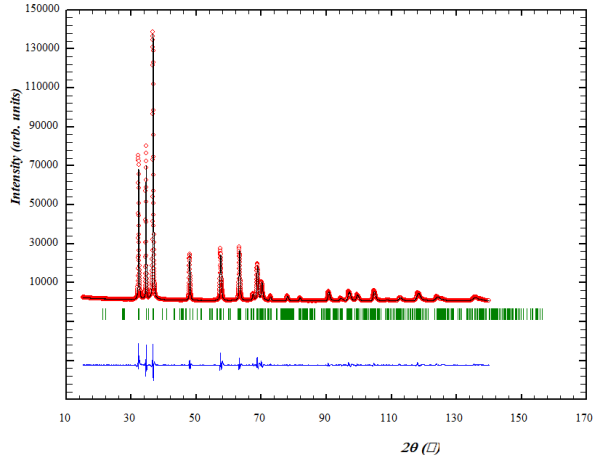

Figure S27: Plot for the Rietveld refinement of the X-ray powder diffraction profile: Measured Intensity (red circles), calculated intensity (black line), difference I_{obs}–I_{calc} (blue line) and calculated reflection positions (green ticks).

Sample 28:

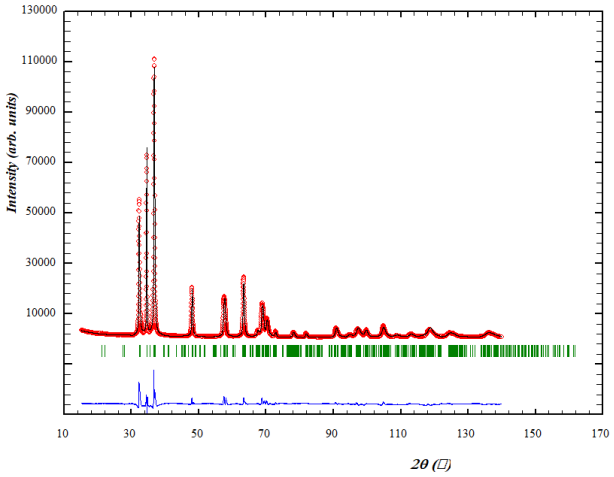

Figure S28: Plot for the Rietveld refinement of the X-ray powder diffraction profile: Measured Intensity (red circles), calculated intensity (black line), difference I_{obs}–I_{calc} (blue line) and calculated reflection positions (green ticks).

Sample 29:

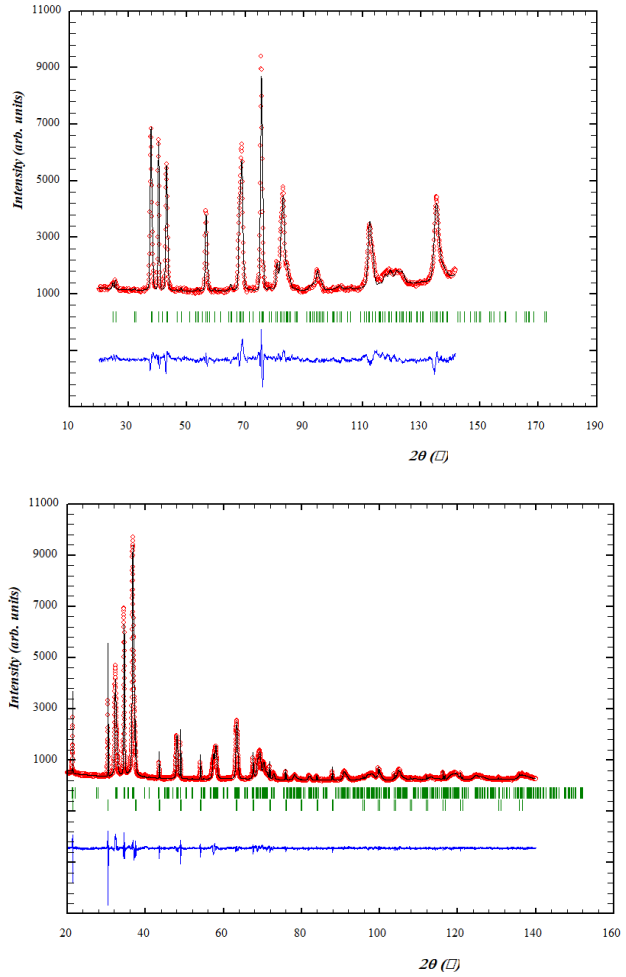

Figure S29: Plot for the simultaneous Rietveld refinement of the neutron (top) and X-ray powder diffraction profile (bottom): Measured Intensity (red circles), calculated intensity (black line), difference I_{obs}–I_{calc} (blue line) and calculated reflection positions (green ticks). XRD figure includes reflections and calculated reflection position (green ticks at bottom) of LaB_6 standard.

Sample 30:

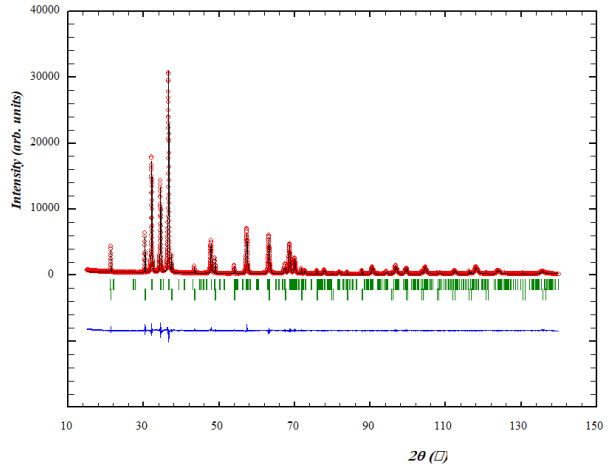

Figure S30: Plot for the Le Bail refinement of the X-ray powder diffraction profile: Measured Intensity (red circles), calculated intensity (black line), difference I_{obs}–I_{calc} (blue line) and calculated reflection positions (green ticks, LaB_6 bottom, Zn-Ge-O-N top).

Sample 31:

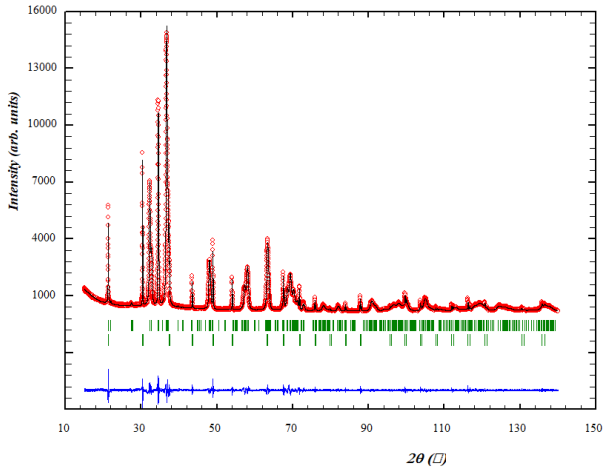

Figure S31: Plot for the Le Bail refinement of the X-ray powder diffraction profile: Measured Intensity (red circles), calculated intensity (black line), difference I_{obs}–I_{calc} (blue line) and calculated reflection positions (green ticks, LaB_6 bottom, Zn-Ge-O-N top).

Sample 32:

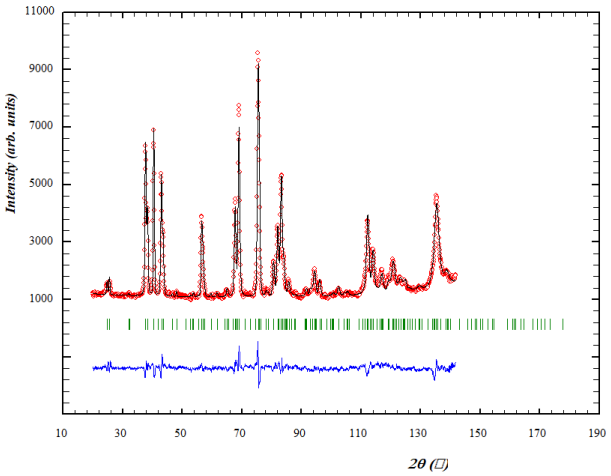

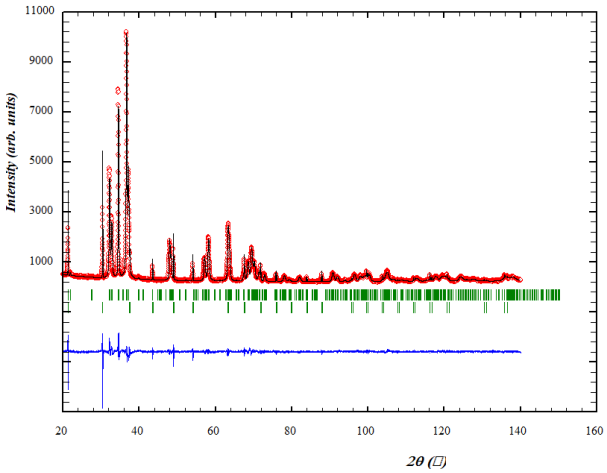

Figure S32: Plot for the simultaneous Rietveld refinement of the neutron (top) and X-ray powder diffraction profile (bottom): Measured Intensity (red circles), calculated intensity (black line), difference I_{obs}–I_{calc} (blue line) and calculated reflection positions (green ticks). XRD figure includes reflections and calculated reflection position (green ticks at bottom) of LaB_6 standard.

Sample 33:

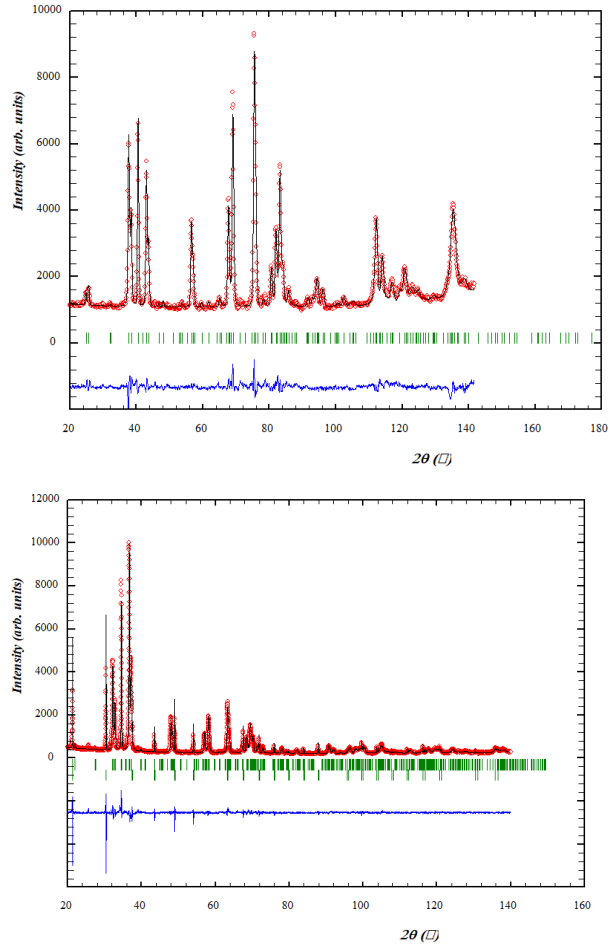

Figure S33: Plot for the simultaneous Rietveld refinement of the neutron (top) and X-ray powder diffraction profile (bottom): Measured Intensity (red circles), calculated intensity (black line), difference I_{obs}–I_{calc} (blue line) and calculated reflection positions (green ticks). XRD figure includes reflections and calculated reflection position (green ticks at bottom) of LaB_6 standard.

Sample 34:

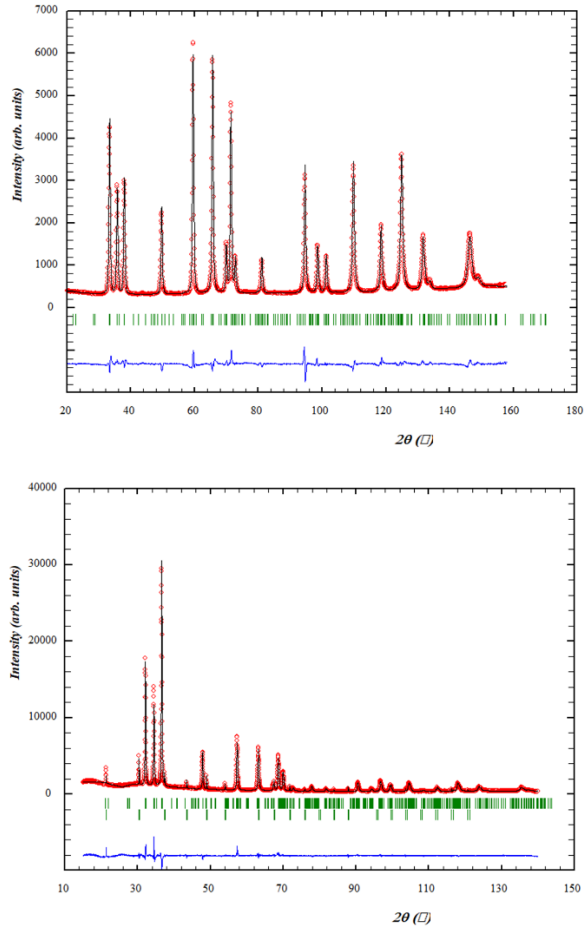

Figure S34: Plot for the simultaneous Rietveld refinement of the neutron (top) and X-ray powder diffraction profile (bottom): Measured Intensity (red circles), calculated intensity (black line), difference I_{obs}–I_{calc} (blue line) and calculated reflection positions (green ticks). XRD figure includes reflections and calculated reflection position (green ticks at bottom) of LaB_6 standard.

Sample 35:

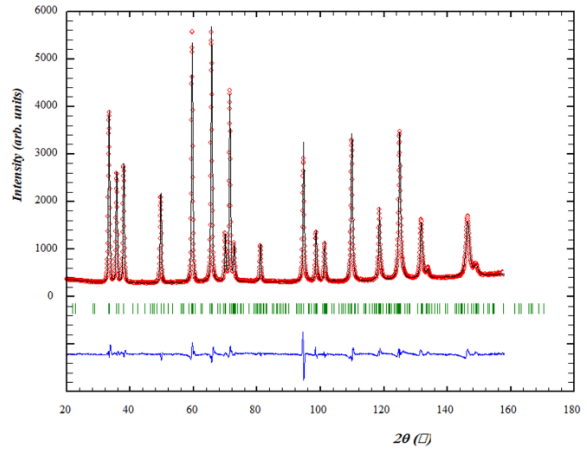

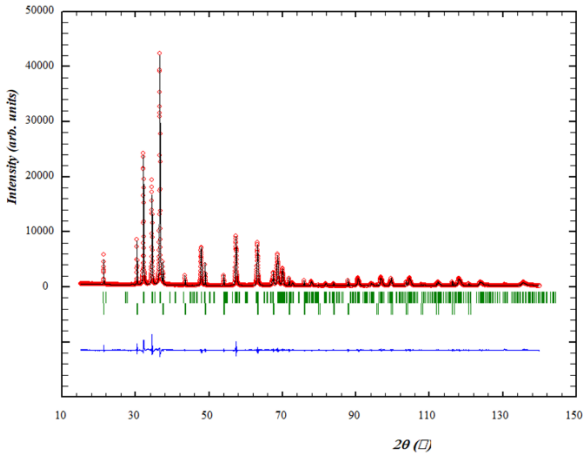

Figure S35: Plot for the simultaneous Rietveld refinement of the neutron (top) and X-ray powder diffraction profile (bottom): Measured Intensity (red circles), calculated intensity (black line), difference I_{obs}–I_{calc} (blue line) and calculated reflection positions (green ticks). XRD figure includes reflections and calculated reflection position (green ticks at bottom) of LaB_6 standard.

Sample 36:

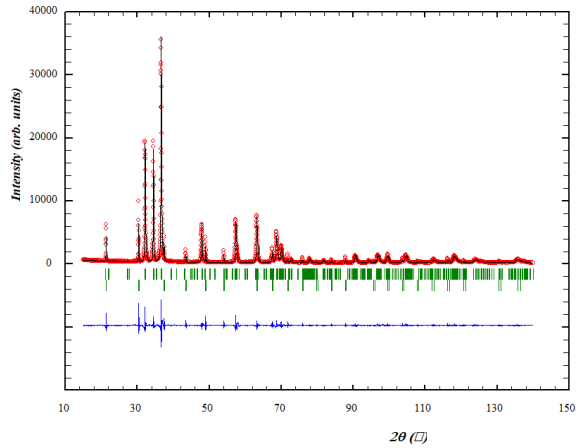

Figure S36: Plot for the Le Bail refinement of the X-ray powder diffraction profile: Measured Intensity (red circles), calculated intensity (black line), difference I_{obs}–I_{calc} (blue line) and calculated reflection positions (green ticks, LaB_6 bottom, Zn-Ge-O-N top).

Sample 37:

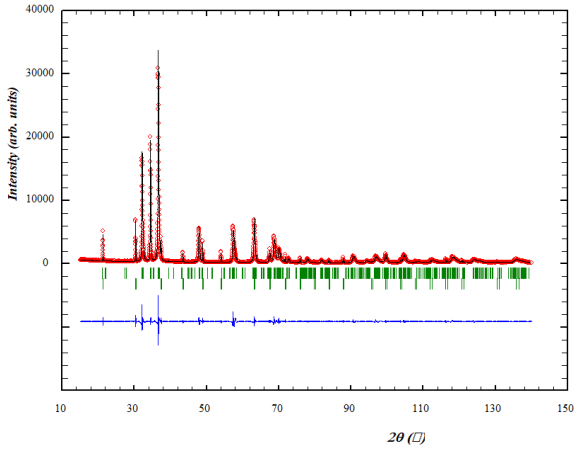

Figure S37: Plot for the Le Bail refinement of the X-ray powder diffraction profile: Measured Intensity (red circles), calculated intensity (black line), difference I_{obs}–I_{calc} (blue line) and calculated reflection positions (green ticks, LaB_6 bottom, Zn-Ge-O-N top).

Sample 38:

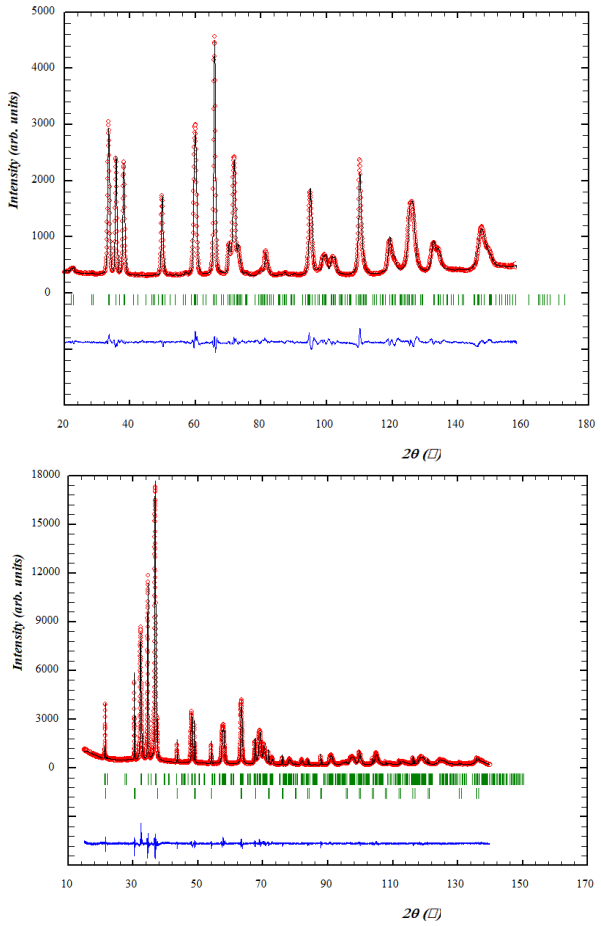

Figure S38: Plot for the simultaneous Rietveld refinement of the neutron (top) and X-ray powder diffraction profile (bottom): Measured Intensity (red circles), calculated intensity (black line), difference I_{obs}–I_{calc} (blue line) and calculated reflection positions (green ticks). XRD figure includes reflections and calculated reflection position (green ticks at bottom) of LaB_6 standard.

Sample 39:

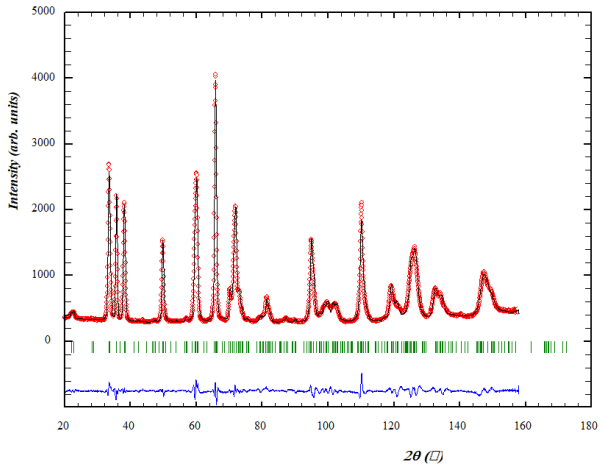

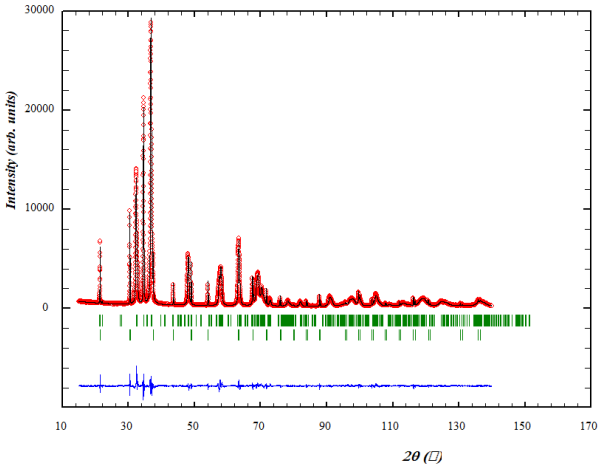

Figure S39: Plot for the simultaneous Rietveld refinement of the neutron (top) and X-ray powder diffraction profile (bottom): Measured Intensity (red circles), calculated intensity (black line), difference I_{obs}–I_{calc} (blue line) and calculated reflection positions (green ticks). XRD figure includes reflections and calculated reflection position (green ticks at bottom) of LaB_6 standard.

Sample 40:

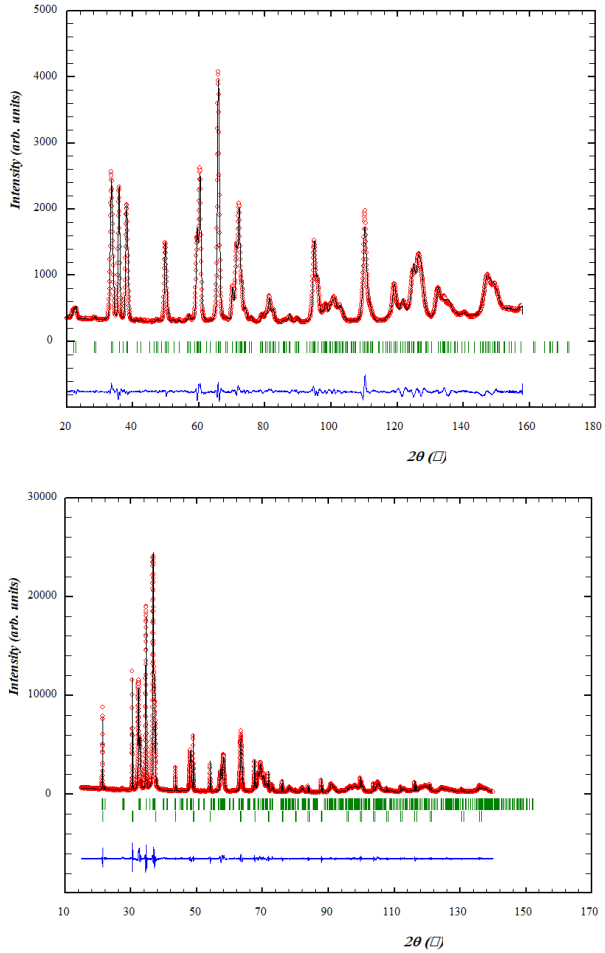

Figure S40: Plot for the simultaneous Rietveld refinement of the neutron (top) and X-ray powder diffraction profile (bottom): Measured Intensity (red circles), calculated intensity (black line), difference I_{obs}–I_{calc} (blue line) and calculated reflection positions (green ticks). XRD figure includes reflections and calculated reflection position (green ticks at bottom) of LaB_6 standard.

Sample 41:

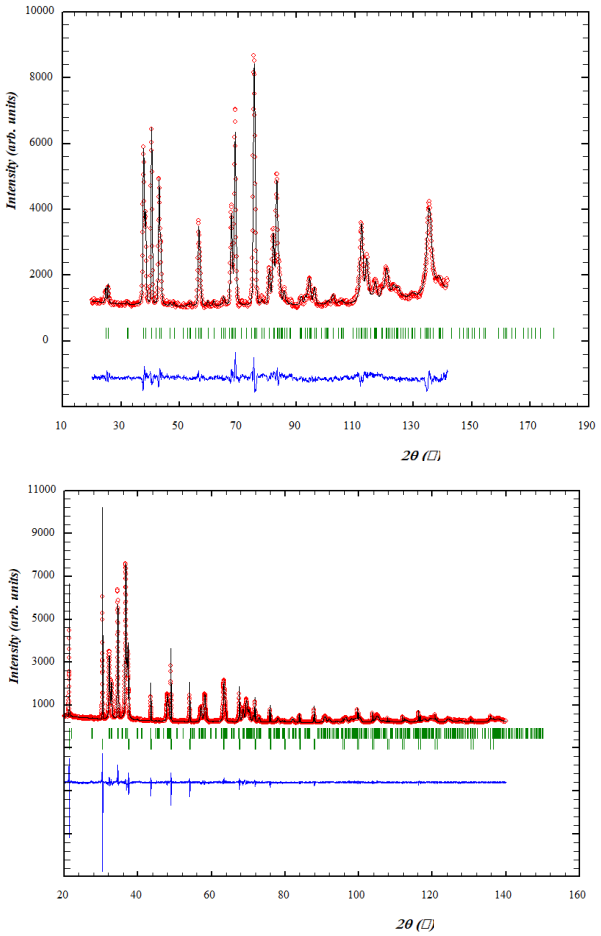

Figure S41: Plot for the simultaneous Rietveld refinement of the neutron (top) and X-ray powder diffraction profile (bottom): Measured Intensity (red circles), calculated intensity (black line), difference I_{obs}–I_{calc} (blue line) and calculated reflection positions (green ticks). XRD figure includes reflections and calculated reflection position (green ticks at bottom) of LaB_6 standard.

Sample 42:

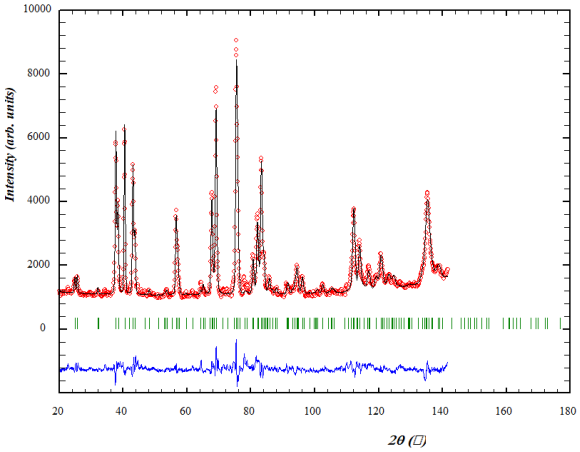

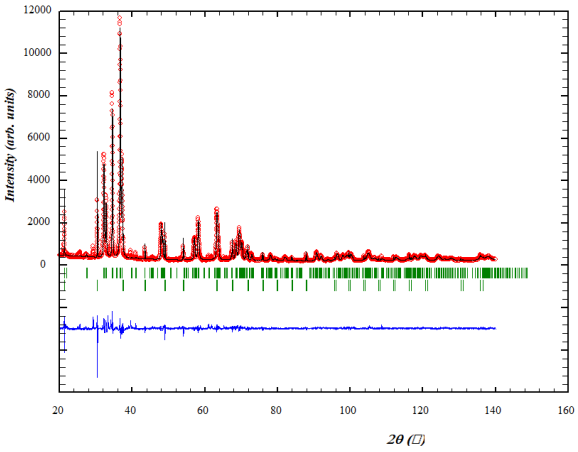

Figure S42: Plot for the simultaneous Rietveld refinement of the neutron (top) and X-ray powder diffraction profile (bottom): Measured Intensity (red circles), calculated intensity (black line), difference I_{obs}–I_{calc} (blue line) and calculated reflection positions (green ticks). XRD figure includes reflections and calculated reflection position (green ticks at bottom) of LaB_6 standard.

Sample 43:

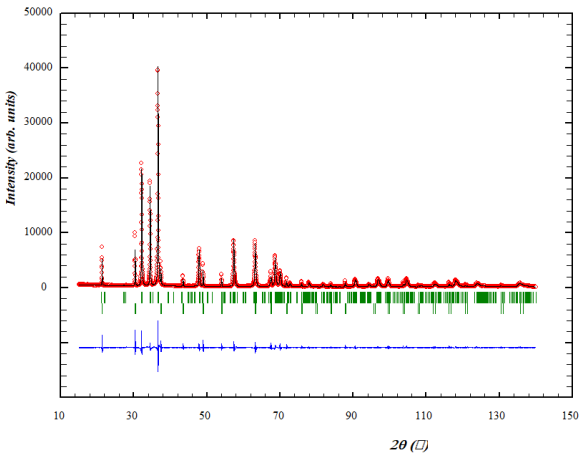

Figure S43: Plot for the Le Bail refinement of the X-ray powder diffraction profile: Measured Intensity (red circles), calculated intensity (black line), difference I_{obs}–I_{calc} (blue line) and calculated reflection positions (green ticks, LaB_6 bottom, Zn-Ge-O-N top).

Sample 44:

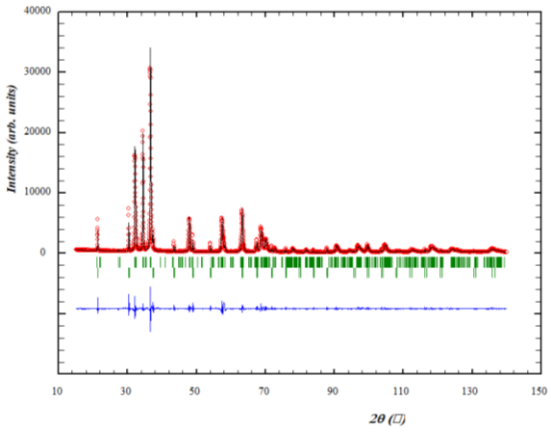

Figure S44: Plot for the Le Bail refinement of the X-ray powder diffraction profile: Measured Intensity (red circles), calculated intensity (black line), difference I_{obs}–I_{calc} (blue line) and calculated reflection positions (green ticks, LaB_6 bottom, Zn-Ge-O-N top).

Sample 45:

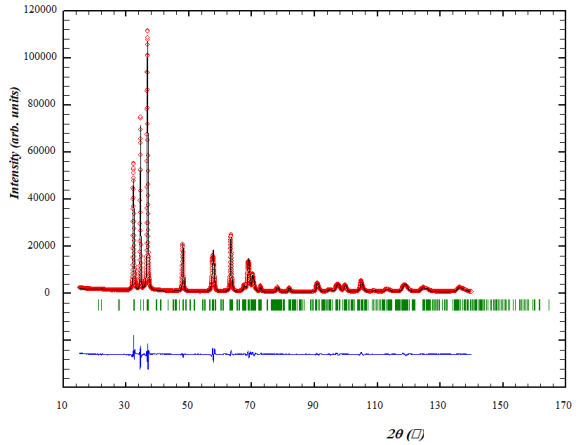

Figure S6: Plot for the Rietveld refinement of the X-ray powder diffraction profile: Measured Intensity (red circles), calculated intensity (black line), difference I_{obs}–I_{calc} (blue line) and calculated reflection positions (green ticks).

Sample 46:

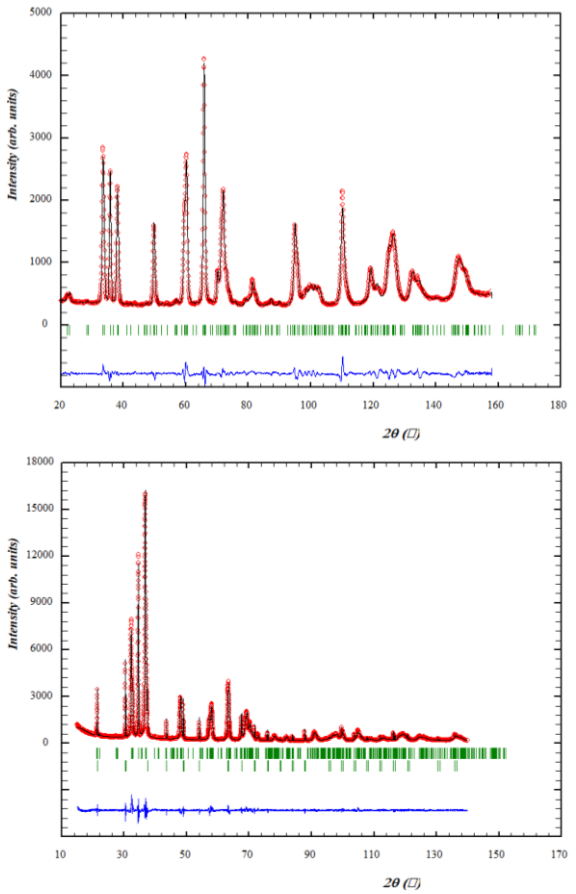

Figure S46: Plot for the simultaneous Rietveld refinement of the neutron (top) and X-ray powder diffraction profile (bottom): Measured Intensity (red circles), calculated intensity (black line), difference I_{obs}–I_{calc} (blue line) and calculated reflection positions (green ticks). XRD figure includes reflections and calculated reflection position (green ticks at bottom) of LaB_6 standard.

Sample 47:

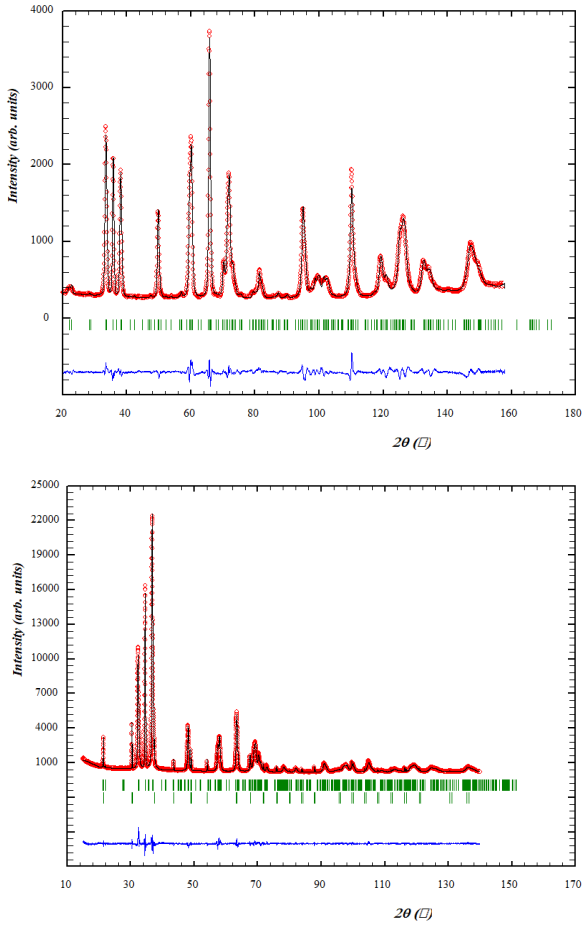

Figure S47: Plot for the simultaneous Rietveld refinement of the neutron (top) and X-ray powder diffraction profile (bottom): Measured Intensity (red circles), calculated intensity (black line), difference I_{obs}–I_{calc} (blue line) and calculated reflection positions (green ticks). XRD figure includes reflections and calculated reflection position (green ticks at bottom) of LaB_6 standard.

Sample 48:

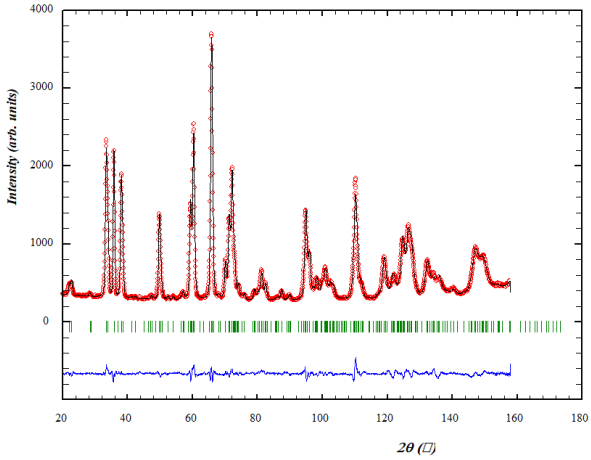

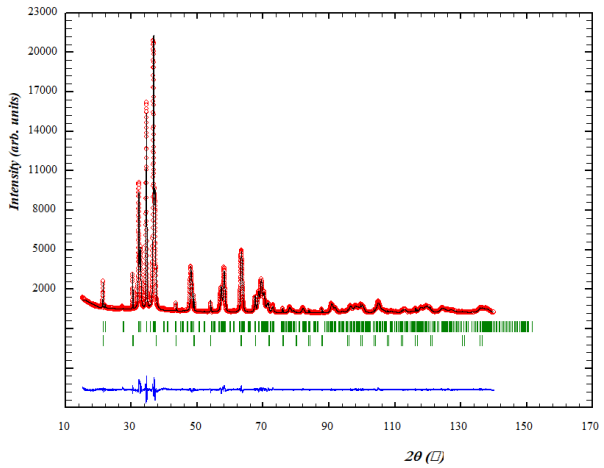

Figure S48: Plot for the simultaneous Rietveld refinement of the neutron (top) and X-ray powder diffraction profile (bottom): Measured Intensity (red circles), calculated intensity (black line), difference I_{obs}–I_{calc} (blue line) and calculated reflection positions (green ticks). XRD figure includes reflections and calculated reflection position (green ticks at bottom) of LaB_6 standard.

Sample 49:

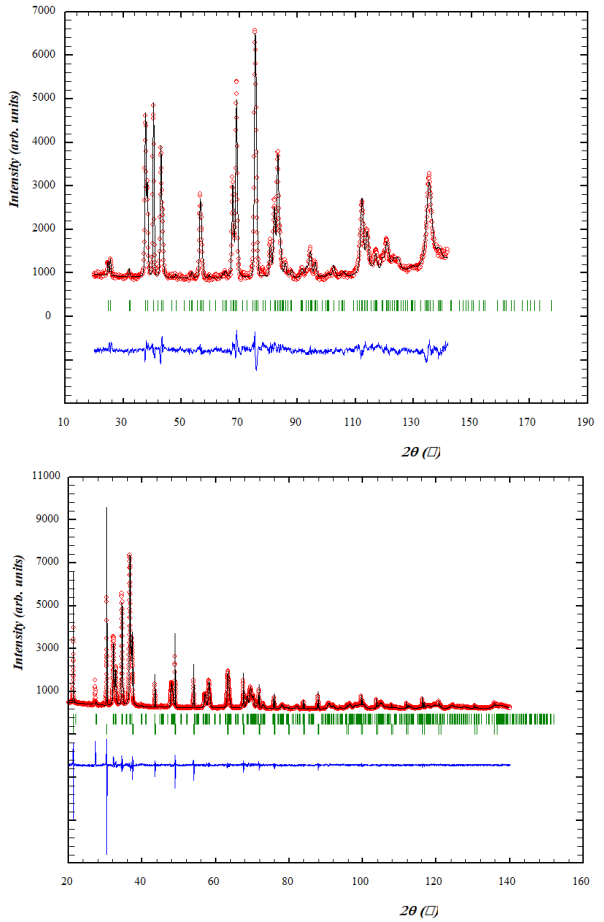

Figure S49: Plot for the simultaneous Rietveld refinement of the neutron (top) and X-ray powder diffraction profile (bottom): Measured Intensity (red circles), calculated intensity (black line), difference I_{obs}–I_{calc} (blue line) and calculated reflection positions (green ticks). XRD figure includes reflections and calculated reflection position (green ticks at bottom) of LaB_6 standard.

5) Information of the studied samples

Table S5: Summary of the reaction conditions and the phase weigth fraction in the as-annealed $Zn_{1+x}Sn_{1-x}(O_xN_{1-x})_2$ samples studied herein

Sample number	Reaction temp. [°C]	dwelling time [h]	*x* in $Zn_{1+x}Ge_{1-x}(O_xN_{1-x})_2$	gas flow for cooling [l·min^{-1}]		Phae weigh fraction [wt. %]			
						$ZnSnN_2$	Zn_3N_2	Sn_3N_4	Sn
50	500	10	0.14(1)	1.5	N_2	9.8	62.1	15.1	13.0
51	530	4	0.16(1)	0.10	NH_3	68.9	26.8	-	4.2
52	560	2	0.19(1)	0.10		79.2	10.6	2.0	8.1
53	560	4	0.13(1)	0.10		71.1	25.4	-	3.5
54	590	4	0.18(1)	0.10		78.6	16.4	-	5.0
55	620	4	0.22(1)	0.10		91.0	2.0	-	6.9
56	650	4	0.33(1)	0.10		84.4	0.3	-	15.3

6) Profile of the whole pattern fitting of diffraction data sets

Sample 50:

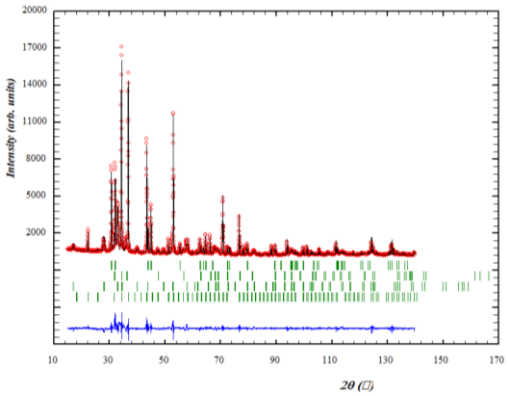

Figure S50: Plot for the Rietveld refinement of XRD profile of as-annealed sample: Measured Intensity (red circles), calculated intensity (black line), difference I_{obs}–I_{calc} (blue line) and calculated reflection positions (green ticks from top to bottom cooresponing to Sn, $ZnSnN_2$, Sn_3N_4 and Zn_3N_2).

Sample 51:

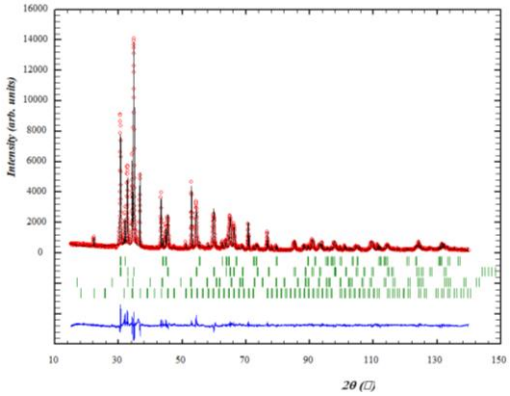

Figure S51: Plot for the Rietveld refinement of XRD profile of as-annealed sample: Measured Intensity (red circles), calculated intensity (black line), difference I_{obs}–I_{calc} (blue line) and calculated reflection positions (green ticks from top to bottom cooresponing to Sn, $ZnSnN_2$, Sn_3N_4 and Zn_3N_2).

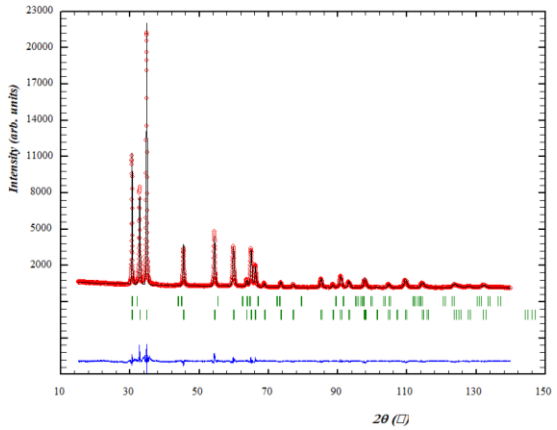

Figure S52: Plot for the Rietveld refinement of XRD profile of as-purified sample: Measured Intensity (red circles), calculated intensity (black line), difference I_{obs}–I_{calc} (blue line) and calculated reflection positions (green ticks, Sn top, $ZnSnN_2$ bottom).

Sample 52:

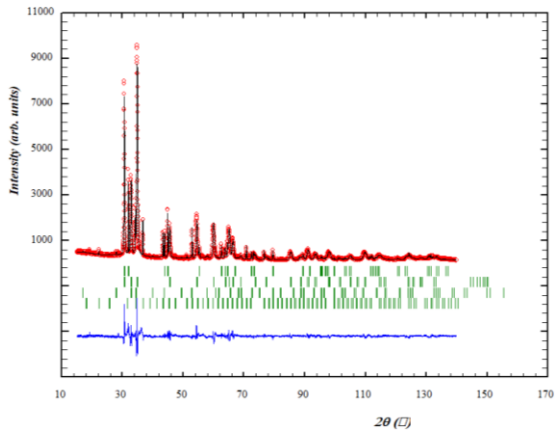

Figure S53: Plot for the Rietveld refinement of XRD profile of as-annealed sample: Measured Intensity (red circles), calculated intensity (black line), difference I_{obs}–I_{calc} (blue line) and calculated reflection positions (green ticks from top to bottom corresponding to Sn, $ZnSnN_2$, Sn_3N_4 and Zn_3N_2).

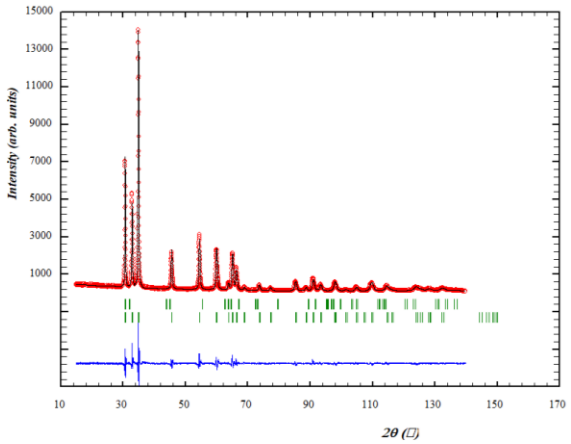

Figure S54: Plot for the Rietveld refinement of XRD profile of as-purified sample: Measured Intensity (red circles), calculated intensity (black line), difference I_{obs}–I_{calc} (blue line) and calculated reflection positions (green ticks, Sn top, $ZnSnN_2$ bottom).

Sample 53:

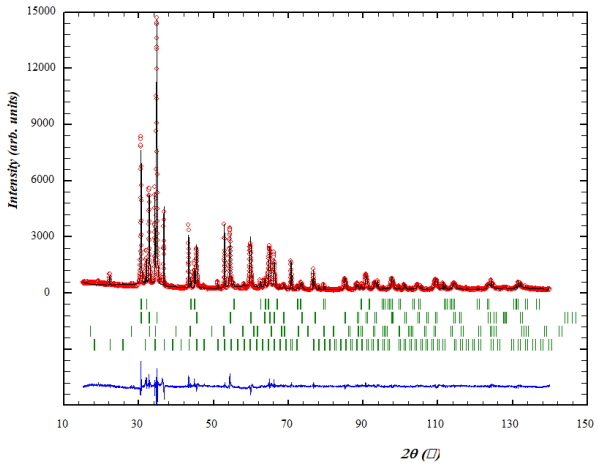

Figure S55: Plot for the Rietveld refinement of XRD profile of as-annealed sample: Measured Intensity (red circles), calculated intensity (black line), difference I_{obs}–I_{calc} (blue line) and calculated reflection positions (green ticks from top to bottom corresponding to Sn, $ZnSnN_2$, Sn_3N_4 and Zn_3N_2).

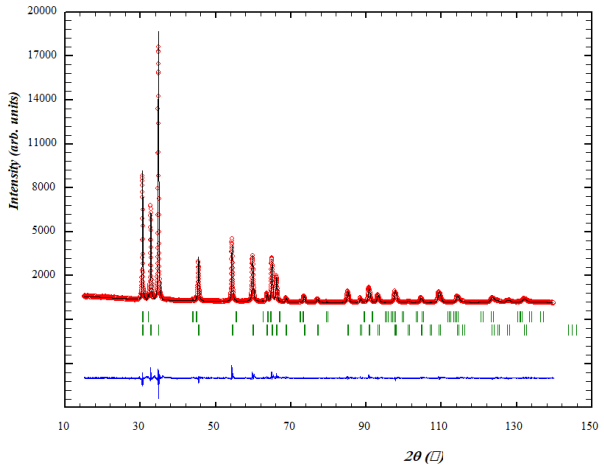

Figure S56: Plot for the Rietveld refinement of XRD profile of as-purified sample: Measured Intensity (red circles), calculated intensity (black line), difference I_{obs}–I_{calc} (blue line) and calculated reflection positions (green ticks, Sn top, $ZnSnN_2$ bottom).

Sample 54:

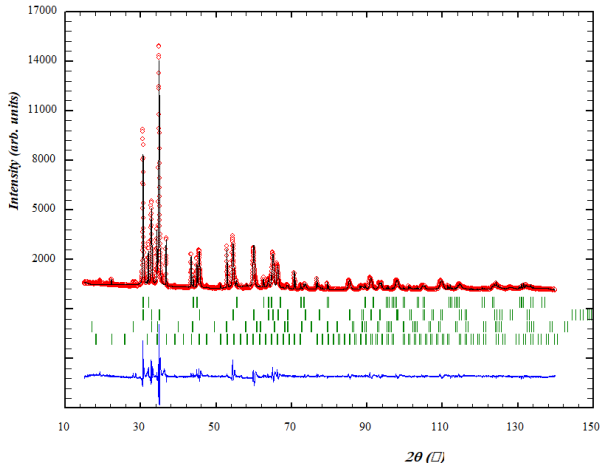

Figure S57: Plot for the Rietveld refinement of XRD profile of as-annealed sample: Measured Intensity (red circles), calculated intensity (black line), difference I_{obs}–I_{calc} (blue line) and calculated reflection positions (green ticks from top to bottom corresponding to Sn, $ZnSnN_2$, Sn_3N_4 and Zn_3N_2).

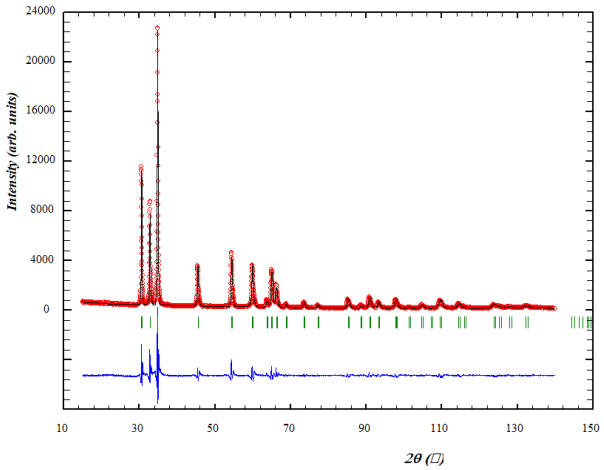

Figure S58: Plot for the Rietveld refinement of XRD profile of as-purified sample: Measured Intensity (red circles), calculated intensity (black line), difference I_{obs}–I_{calc} (blue line) and calculated reflection positions (green ticks).

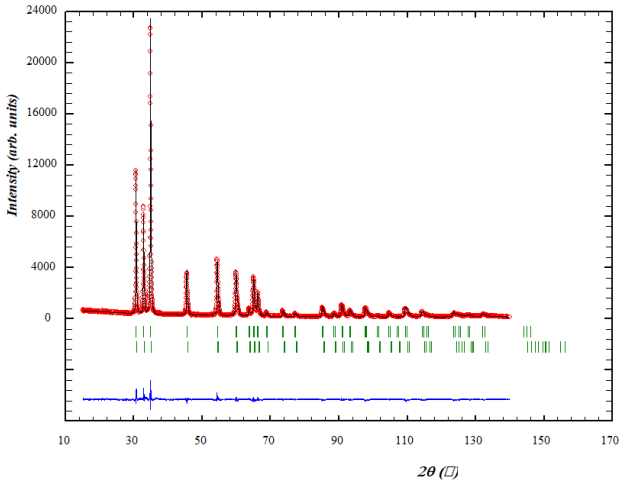

Figure S59: Plot for the Rietveld refinement of XRD profile using the two-phase model: Measured Intensity (red circles), calculated intensity (black line), difference I_{obs}–I_{calc} (blue line) and calculated reflection positions (green ticks).

Sample 55:

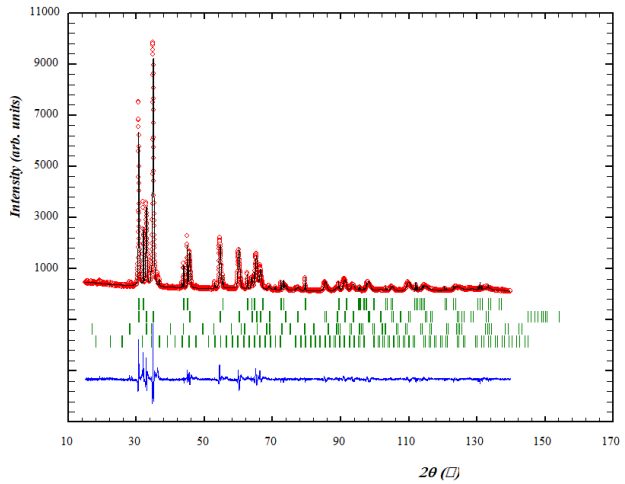

Figure S60: Plot for the Rietveld refinement of XRD profile of as-annealed sample: Measured Intensity (red circles), calculated intensity (black line), difference I_{obs}–I_{calc} (blue line) and calculated reflection positions (green ticks from top to bottom corresponding to Sn, $ZnSnN_2$, Sn_3N_4 and Zn_3N_2).

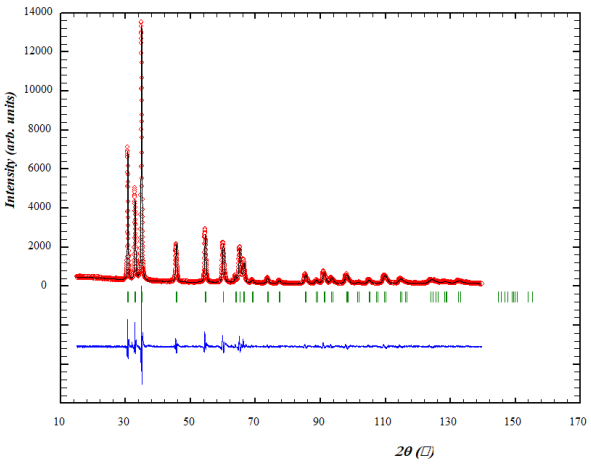

Figure S61: Plot for the Rietveld refinement of XRD profile of as-purified sample: Measured Intensity (red circles), calculated intensity (black line), difference I_{obs}–I_{calc} (blue line) and calculated reflection positions (green ticks).

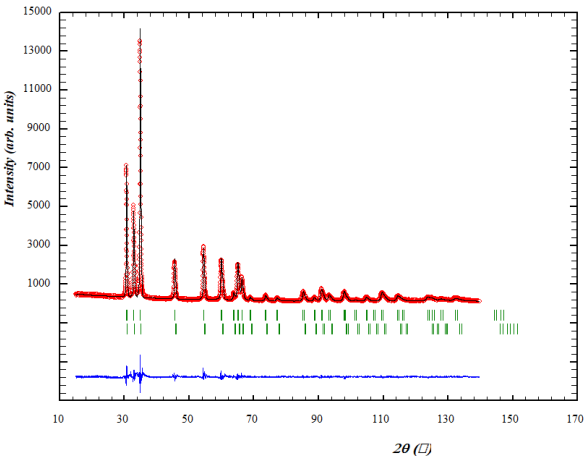

Figure S62: Plot for the Rietveld refinement of XRD profile using the two-phase model: Measured Intensity (red circles), calculated intensity (black line), difference I_{obs}–I_{calc} (blue line) and calculated reflection positions (green ticks).

Sample 56:

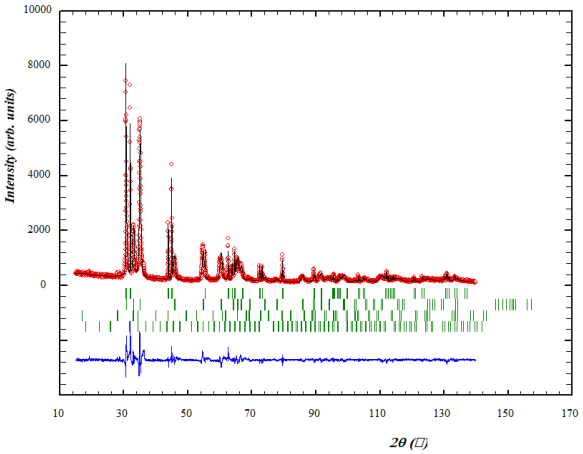

Figure S63: Plot for the Rietveld refinement of XRD profile of as-annealed sample: Measured Intensity (red circles), calculated intensity (black line), difference I_{obs}–I_{calc} (blue line) and calculated reflection positions (green ticks from top to bottom corresponding to Sn, $ZnSnN_2$, Sn_3N_4 and Zn_3N_2).

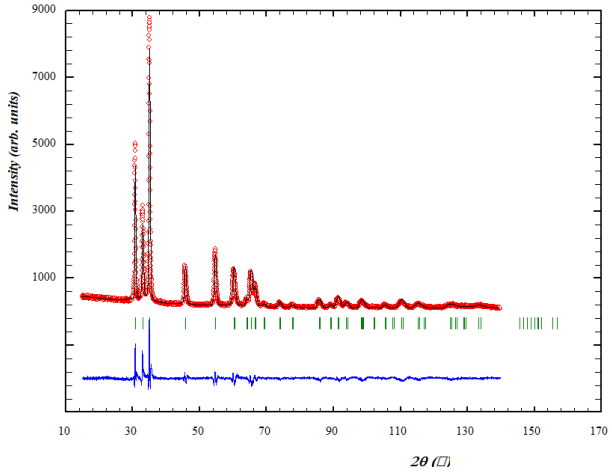

Figure S64: Plot for the Rietveld refinement of XRD profile of as-purified sample: Measured Intensity (red circles), calculated intensity (black line), difference I_{obs}–I_{calc} (blue line) and calculated reflection positions (green ticks).

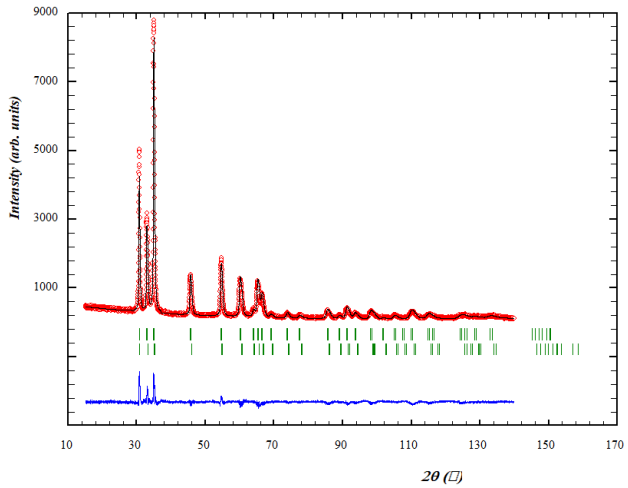

Figure S65: Plot for the Rietveld refinement of XRD profile using the two-phase model: Measured Intensity (red circles), calculated intensity (black line), difference I_{obs}–I_{calc} (blue line) and calculated reflection positions (green ticks).